The Thesis Committee for Francis William McInerny Pinkston
Certifies that this is the approved version of the following thesis:

Pore Pressure and Stress at the Macondo Well, Mississippi Canyon, Gulf of Mexico

APPROVED BY
SUPERVISING COMMITTEE:

Supervisor:

Peter B. Flemings

David C. Mohrig

John W. Snedden

Pore Pressure and Stress at Macondo, Mississippi Canyon, Gulf of Mexico

by

Francis William McInerny Pinkston

Thesis

Presented to the Faculty of the Graduate School of

The University of Texas at Austin

in Partial Fulfillment

of the Requirements

for the Degree of

Masters of Science in Geological Sciences

The University of Texas at Austin

December 2017

Acknowledgements

I would like to thank my advisor, Peter B. Flemings, for helping me develop my geoscience, problem-solving, and communication skillsets. His guidance throughout the research process has been and will continue to be invaluable. In addition, I want to thank him for his generosity in sharing his academic and industry networks. This unique exposure has been an incredible resource for improving my research.

I want to thank the following professors, researchers, industry experts, students, and administrators for their willingness and enthusiasm to share time and expertise: John Germaine, Maria-Katerina Nikolinakou, and the rest of the Geofluids team for providing feedback and research ideas; John Snedden and GBDS Project for the knowledge and resources that made possible well correlation and seismic interpretation; countless Geofluids Consortium industry experts for their advice and interest in my project; David Mohrig for his valuable suggestions; Mark Wiederspahn and Joseph Sung-Ling Yeh for assisting with technical issues and data acquisition; Tessa Green, Colleen Morgan, Jac Erengil, and Philip Guerrero for helping me navigate through my master’s degree.

I would also like to express my sincere gratitude to those that made possible my work through their generous financial support: Peter B. Flemings and John Germaine; the Geofluids Consortium and its sponsors Anadarko, BHP, BP, Chevron, ConocoPhillips, ExxonMobil, Hess, Pemex, Repsol, Shell, Statoil, and Tufts; the Teagle family and Chevron for honoring me with fellowships; the Jackson School of Geosciences and UTIG; TGS for allowing access to the 3D seismic survey.

Finally, I thank my parents, siblings, friends and Amanda for their unending love as I follow my passions.

Abstract

Pore Pressure and Stress at Macondo, Mississippi Canyon, Gulf of Mexico

Francis William McInerny Pinkston, MSGeoSci

The University of Texas at Austin, 2017

Supervisor: Peter B. Flemings

At the Macondo (MC 252-1) well, the overpressure (fluid pressure greater than hydrostatic) in the main reservoir is nearly identical to that within a stratigraphically equivalent sandstone at the Galapagos Field development 21 miles (34 km) to the south; we interpret that these reservoirs share a permeable, laterally extensive, and hydraulically connected aquifer. At Macondo, pore pressure and least principal stress approximately parallel the overburden stress to a depth of 17,640 ft z_{ss} (5,377 m) subsea and thereafter decreases abruptly by 1,200 psi (8.3 MPa) over 370 ft (113 m) as the main sandstone reservoir is approached. In contrast, at Galapagos Field, pore pressure increases with the overburden stress for the entire well depth. We infer that lateral flow through the permeable sandstone controls the reservoir pressure. By modeling fracture pressure with an effective stress ratio, we show that the pore pressure regression at Macondo was responsible for a reduction in fracture pressure across the reservoir interval. This, in combination with the extreme pore pressures above, drastically narrowed the range of

safe operational borehole pressures. These geologic factors led to drilling, casing, and cementing decisions that ultimately contributed to the Deepwater Horizon blowout.

Table of Contents

List of Tables

List of Figures

Chapter 1: Introduction

On April 20, 2010, the *Deepwater Horizon* blowout of the Macondo well began in Mississippi Canyon (MC) block 252, deepwater Gulf of Mexico (Fig. 2.1). Eleven people died as a result of the Deepwater Horizon explosion, and over the next three months, an estimated 4 million barrels of oil leaked into the Gulf of Mexico (Boebert and Blossom, 2016). This human and environmental catastrophe brought to the fore of public consciousness the extraordinary complexity and risk of finding and producing hydrocarbons in the deep ocean. For the first time, the media spotlight focused on the incredible pressures encountered in the search for deepwater hydrocarbon targets. There has been detailed inquiry into the design and engineering failures that resulted in the blowout (Bartlit et al., 2011; Boebert and Blossom, 2016; Engineering and Council, 2012; Hickman et al., 2012; McNutt et al., 2012; Turley, 2014). However, there has been relatively little public examination of the observations, mechanisms, and implications of the state of pressure and stress in the Macondo well.

In the following Chapters, I characterize the pressure and stress profile of the Macondo well. I catalogue measurements, tests, and drilling events, and then use them to model pore pressure and least principal stress in the formations penetrated by the wellbore. I interpret that both the pore pressure and the least principal stress increase in parallel with the overburden stress from near the seafloor to just above the main reservoir, the M56. Within this reservoir interval, pressure and stress abruptly decrease in both the sandstones and mudstones.

To understand the pressure regression at the Macondo well, I analyze the pressure and stress in nearby wells. I correlate the sandstone reservoir that was the source of the blowout over an area of 500 mi^2 using 3D seismic data. The overpressure within this sandstone 21 miles (34 km) to the southwest is within 1.5% of that at Macondo. I interpret that the M56 reservoir is part of a larger hydraulically connected aquifer, and present two models to describe the large pore pressure and stress regression present at Macondo. Finally, I summarize how the Macondo pore pressure profile ultimately led to decisions that contributed to the well failure.

Several fascinating questions emerging from this work warrant future research. The mechanisms behind the above-overburden LOT and FIT results at the 13-5/8”, 11-7/8” and 9-5/8” shoes remain poorly understood (Chapter 3.2.1 & 3). I attribute the results to be a consequence of stress concentration around an unfractured borehole. However, alternative explanations (e.g. salinity) merit investigation given that this phenomenon was encountered at multiple casing shoes and in nearby wells. How formation pressure integrity test results relate to the fracture pressure has significant economic implications for casing design and well control. In addition, the Macondo well showcases another recurring issue facing the oil and gas industry in how the porosity-effective stress relationship changes with depth (Chapter 2.2.4). I simplify the geophysical response to be a function of smectite-to-illite transformation, but these assumptions are not well constrained or understood.

My analysis is based on publically available well data archived by the BOEM and a 3-D seismic volume of Mississippi Canyon. I also incorporate data and expert analysis from documents released during Multidistrict Litigation 2179, the legal proceedings that ensued the blowout of the *Deepwater Horizon* (Bartlit et al., 2011; Bourgoyne, 2011; BP, 2010f, g; Hickman et al., 2012; Huffman, 2011).

This thesis is comprised of three Chapters and two Appendices. The first Chapter outlines the structure, content, and motivation for this research. Chapter 2 is written as a standalone manuscript for future publication. Here, I synthesize the Macondo pore pressure regression, regional model, and implications for *Deepwater Horizon* blowout. Chapter 3 presents the parallel study of the least principal stress at Macondo well. The Appendices supplement the Materials and Methods section of Chapter 2. Together, the Materials and Methods section of Chapter 2, Chapter 3, and the Appendices serve as a comprehensive repository for the available pressure and stress data for the Macondo well. MDL 2179 released an enormous trove of documents spanning all aspects of the *Deepwater Horizon* blowout, and these sections compile materials exclusively related to pressure and stress. I envision these sections as a resource for future researchers analyzing the Macondo well and as a detailed workflow for pore pressure and stress analysis.

Chapter 2: Pore pressure regression in the Macondo well and implications for the *Deepwater Horizon* blowout

ABSTRACT

At the Macondo well (MC 252-1), the overpressure (fluid pressure greater than hydrostatic) in the main reservoir is nearly identical to that within a stratigraphically equivalent sandstone at the Galapagos Field development 21 miles (34 km) to the south; we interpret that the reservoirs share a permeable, laterally extensive, and hydraulically connected aquifer. At Macondo, pore pressure approximately parallels the overburden stress to a depth of 17,640 ft (5,377 m) subsea and thereafter decreases abruptly by 1,200 psi (8.3 MPa) over 370 ft (113 m) as the main sandstone reservoir is approached. In contrast, at Galapagos Field, pore pressure increases with the overburden stress for the entire well depth. We infer that lateral flow through the permeable sandstone controls the reservoir pressure. The pore pressure regression at Macondo was responsible for a reduction in fracture pressure. This, in combination with the extreme pore pressures above, drastically narrowed the range of safe operational borehole pressures. These geologic factors led to drilling, casing, and cementing decisions that contributed to the Deepwater Horizon blowout.

SIGNIFICANCE STATEMENT

The *Deepwater Horizon* blowout of the Macondo well created one of the worst environmental disasters in the history of the United States, highlighting the complexity of deepwater hydrocarbon exploration. A well-studied chain of engineering failures ultimately culminated in the blowout, but here, we focus on the natural pore pressure and stress conditions encountered in the well. By synthesizing a 3-D seismic survey, petrophysical logs, and drilling data, we establish that regional hydraulic connectivity of the main reservoir caused a dramatic and unexpected drop (regression) in the pore pressure and stress profile at the bottom of the well. These geologic phenomena produced challenging conditions for drilling, prevented successful temporary abandonment of the well, and contributed to well failure.

2.1 INTRODUCTION

On April 20, 2010, the Deepwater Horizon blowout of the Macondo well began in Mississippi Canyon block 252, deepwater Gulf of Mexico (Fig. 2.1). Eleven people died as a result of the Deepwater Horizon explosion, and over the next three months, an estimated 4 million barrels of oil leaked into the Gulf of Mexico (Boebert and Blossom, 2016). This human and environmental catastrophe brought to the fore of public consciousness the extraordinary complexity and risk of finding and producing hydrocarbons in the deep ocean. For the first time, the national and global media spotlight focused on the incredible pressures encountered in the search for deepwater hydrocarbon targets. There has been detailed inquiry into the design and engineering failures that resulted in the blowout (Bartlit et al., 2011; Boebert and Blossom, 2016; Engineering and Council, 2012; Hickman et al., 2012; McNutt et al., 2012; Turley, 2014). However, there has been relatively little examination of the observations, mechanisms, and implications of the state of pressure and stress in the Macondo well.

We characterize pore pressure and stress within mudstones and sandstones at the Macondo well. We then correlate the sandstone that was the source of the blowout over an area of 500 mi^2, and we document that the overpressure within this sandstone 21 miles (34 km) to the southwest is within 1.5% of that at Macondo. We interpret that the main reservoir, the M56, is part of a larger hydraulically connected aquifer and present a model to describe the large pore pressure regression present at Macondo. Finally, we summarize how the Macondo pore pressure profile ultimately led to decisions that contributed to the well failure. Our analysis is based on publically available well data archived by the BOEM and a 3-D seismic volume of Mississippi Canyon. We also gained insights through analysis of documents used during legal proceedings related to the Macondo well (Bartlit et al., 2011; Bourgoyne, 2011; BP, 2010f, g; Hickman et al., 2012; Huffman, 2011).

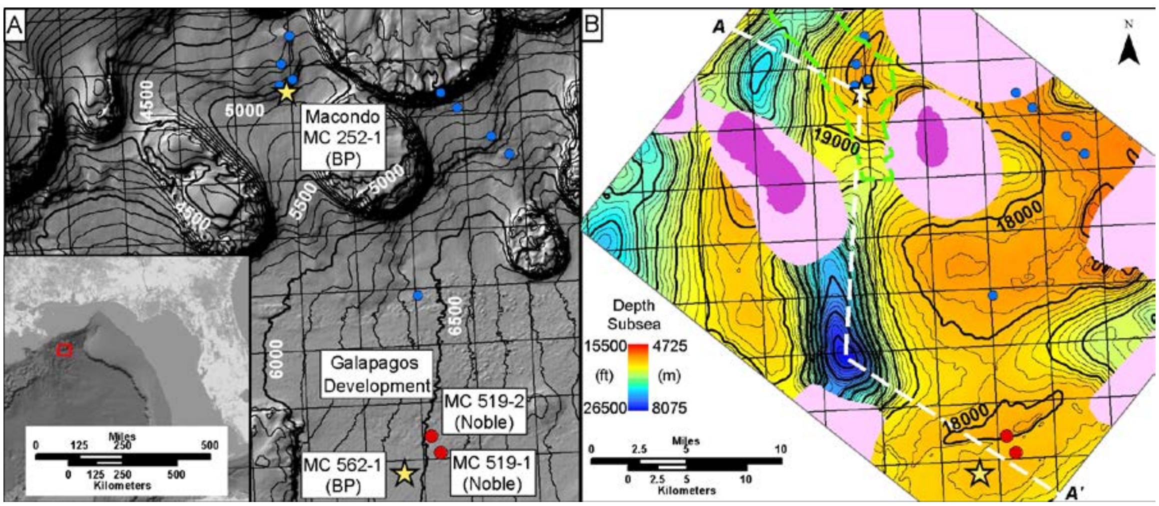

Figure 2.1 The Macondo well, MC 252-1, operated by BP, is located 133 miles (214 km) SE of New Orleans in 4,992 ft (1,522 m) of water. Fig. 2.1A and 1B are collocated and at the same scale. (A) Bathymetry map of the study location. Contour interval = 100 ft (30 m). Symbols record bottom-hole locations of wells that penetrate the M56. The Macondo and MC 562-1 wells are analyzed in this study (Fig. 2.2 and 2.3) The Noble wells (red dots) are used to constrain the aquifer pressure at MC 562-1. Blue dots locate wells that penetrated the M56 post-blowout. (B) The true vertical depth subsea of the M56 interpreted from 3-D seismic data. Contour interval = 250 ft (76 m). Location of the cross-section shown in Fig. 2.4 is annotated A-A' with a white dashed line. The green dashed line denotes the M56 reservoir shape from BP's exploration plan (BP, 2009d), but is artificially truncated N-S. The structural map of the M56 reservoir is interpreted from a 3-D seismic volume that is zero-phase, narrow-azimuth, tilted transversely isotropic, and pre-stack reverse-time-migrated in depth. Dark pink indicates truncation of the M56 by

salt stocks. The narrow-azimuth survey does not image bedding beneath salt (light pink).

2.2 Results and Discussion

2.2.1 Macondo Pore Pressure Profile

Pore pressures, u, in most sedimentary basins are bound below by the hydrostatic pressure, u_h, and above the overburden stress, σ_v. Pore pressure above hydrostatic pressure is the overpressure, u^* ($u^* = u - u_h$). The difference between the overburden stress and the pore pressure is the vertical effective stress ($\sigma_v' = \sigma_v - u$). The Macondo pore pressure profile (Fig. 2.2) has two basic characteristics. First, from near the seafloor to 17,640 ft z_{ss} (5,377 m) pore pressures approximately parallel the overburden stress and the effective stress is approximately constant. The first pore pressure indicator at 7,500 ft z_{ss} (2,300 m) confirms the shallow onset of overpressure; this is common in deepwater Gulf of Mexico (Flemings et al., 2008). From 7,500 to 11,000 ft z_{ss} (2,300 to 3,350 m), σ'_v increases from 700 to 1,200 psi (5 to 8 MPa). Then from 11,650 to 17,640 ft z_{ss} (3,551 to 5,377 m), u increases subparallel with σ_v; thus σ'_v maintains a narrow window between 1,150 and 1,550 psi (7.9 and 10.7 MPa). Second, pore pressure drops as the main reservoir target, the M56 sandstone, is approached. From 17,640 ft z_{ss} (5,377 m) to the base of the well, a pore pressure regression of 1,200 psi (8.3 MPa) is recorded over 370 ft (113 m) between two sandstone packages, the M57 and M56. Most of the pore pressure drop occurs over a vertical distance of just 100 ft (30 m). From the bottom of the M57 at 17,640 ft z_{ss} (5,377 m) to the top of the M56 at 17,740 ft z_{ss} (5,407 m), u decreases from 13,050 to 12,050 psi (89.9 to 83.1 MPa).

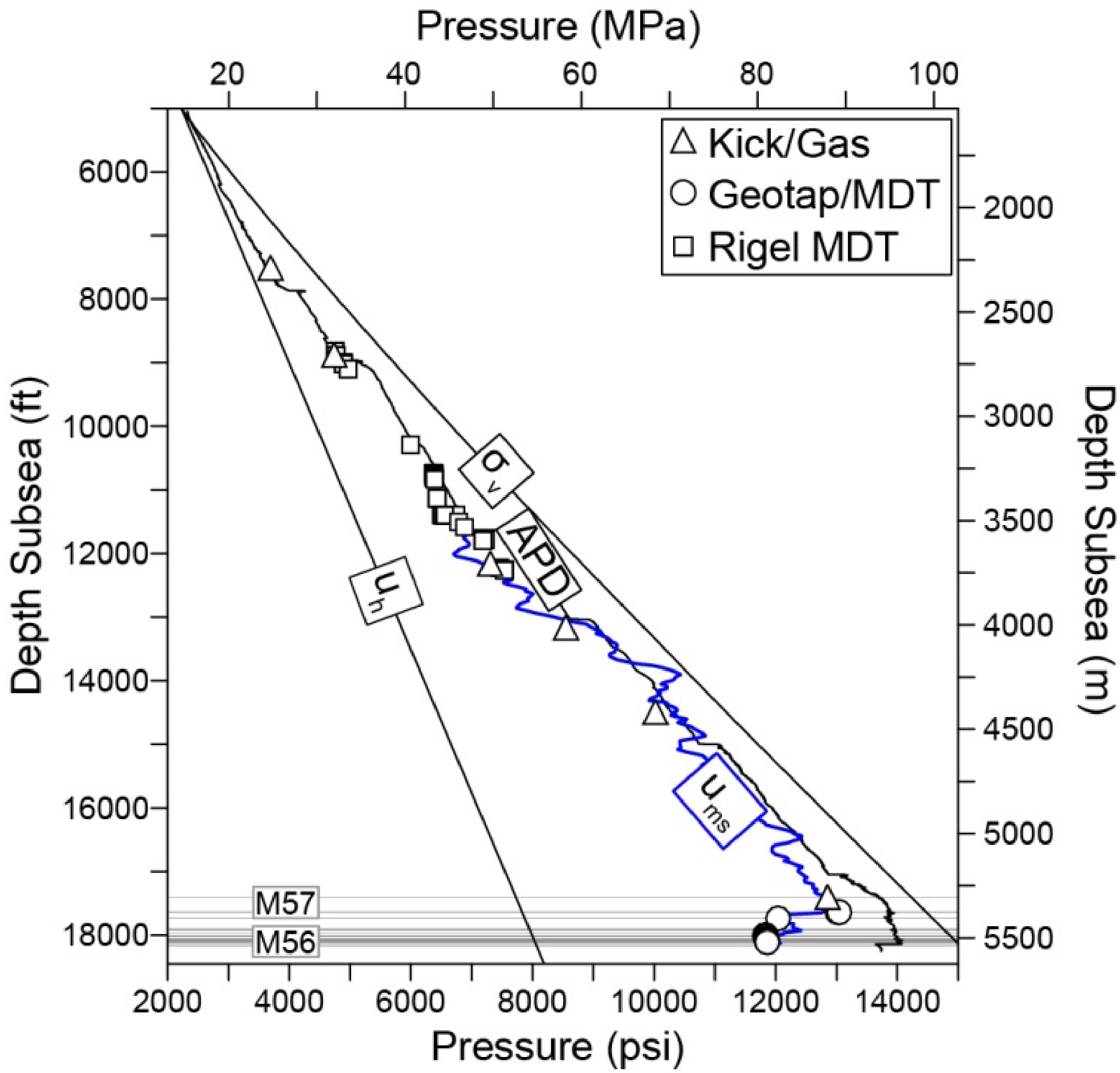

Figure 2.2 Pressure and stress vs. depth beneath sea surface (subsea) from the seafloor to the base of the well. The hydrostatic pressure, u_h, assumes a constant fluid density of 1.024 g/cm^3 (seawater) from the sea surface. The overburden stress, σ_v, is calculated by integrating the density of the sediment below the seafloor (see Supporting Information, SI). Direct measurements of pore pressure are shown with symbols (triangles, squares, circles; see SI for discussion). The mudstone pressure, u_{ms}, interpreted from the (sonic) velocity log is shown with the blue line and the annular pressure-while-drilling (APD) measured near the drill bit is shown with the black line. The depths associated with the M57 and M56 sandstones are highlighted in gray.

The symbols in Fig. 2.2 note pore pressures recorded within permeable sandstones; in addition, we estimate the mudstone pressure, u_{ms} (Fig. 2.2, blue line) based on the velocity log. Our approach to estimating u_{ms} stems from the observation that rock compaction increases with effective stress (Athy, 1930; Rubey and Hubbert, 1959); our methodology is described below. The resulting pore pressure profile is quite similar to the measured sandstone pressures. From 11,650 to 17,640 ft z_{ss} (3,551 to 5,377 m), mudstone effective stress is nearly constant with 90% of the model output between 700 and 1,800 psi (5 and 12 MPa); thus, u_{ms} increases subparallel to the overburden. Below 17,640 ft z_{ss} (5,377 m), the mudstone pore pressure estimate fully captures the magnitude of the pore pressure regression measured in the M56 reservoir interval, supported by observed MDT pressures taken within the sandstone.

2.2.2 Seismic Interpretation and Stratigraphic Correlation

We map the spatial distribution of the top of the Miocene M56 sandstone reservoir across a 20 by 29 mile (32 by 47 km) area using a 3-D seismic volume (Fig. 2.1B). We tie the top of the M56 reservoir from log data to a reflection in the seismic data, and then correlate this event across the seismic volume. The top M56 surface ranges from 15,500 to 26,500 ft z_{ss} (4,700 to 8,100 m) resulting in over 11,000 ft (3,350 m) of relief within our study area (Fig. 2.1B). Structural relief reflects salt tectonics, with some salt diapirs and stocks locally truncating the reservoir. One structural high to the north is penetrated by the Macondo well, and a second to the south targeted by the Galapagos Field development (Figure 2.1B). Our mapped surface closely correlates with BP's independent analysis of the depth of the M56.

The sandstone itself could not be resolved with these seismic data. However, regional sandstone distribution from well control and depositional axis trends both support sandstone continuity between the Macondo and Galapagos Field wells. Significant sandstones correlate with the M56 surface at every well penetration shown in Fig. 2.1B. In this region, the transport of sand by turbidity flows in the Middle Miocene was NW to SE (Combellas-Bigott and Galloway, 2006). The geologic model from BP's exploration plan defines the M56 reservoir as an amalgamated, low-relief channel-levee complex that trends NW-SW and has an average thickness of 25-43 ft (7-13 m) (BP, 2009d). Modern analogs of elongate, continuous, sand-prone channel-levees can exceed 30 miles (50 km) (Posamentier, 2003). This characterization of the M56 sandstone (Fig. 2.1B, dashed green line) is consistent with subsequent reservoir simulation that supports a long but narrow aquifer (Hsieh, 2011).

2.2.3 Aquifer Pressure

We compare aquifer pressure present at Macondo with the aquifer pressure present at the Galapagos Field development. Aquifer pressure refers to the water-phase pressure in the sandstone and it removes the effect of hydrocarbon buoyancy (Flemings et al., 2002). Aquifer pressure is commonly characterized as overpressure because the aquifer overpressure, u_a*, is a single number that is independent of depth within a permeable sandstone (Reilly and Flemings, 2010; Seldon and Flemings, 2005). At Macondo, we calculate u_a* of 3,386 psi (23.35 MPa) by assuming an oil-water contact of 18,375 ft z_{ss} (5,601 m) (see SI). At the Galapagos Field wells, u_a* is 3,433 psi (23.67 MPa). The difference in u_a* between the Macondo and Galapagos Field locations is 47 psi (0.32 MPa) which is less than 1.5%. We interpret that nearly identical u_a* indicates hydraulic connectivity through a shared aquifer.

2.2.4 Pressure and Stress Profile through the M56 at Macondo and Galapagos Field

We compare the (1) pore pressure and (2) velocity profiles across the M56 reservoir at both Macondo and MC 562-1, one of the Galapagos Field wells (Fig. 2.3). (1) The M56 pore pressure and depth are essentially identical at the two locations. At MC 562-1, the pore pressures measured above and below the M56 (Fig. 2.3D, symbols) record a continuous and gradual increase in pore pressure with depth subparallel to the overburden. This contrasts the pore pressure profile at Macondo (Fig. 2.3C) where pore pressure is much lower within the M56 than above it. (2) The mudstone velocities (Fig. 2.3B and E, black lines) in both wells support the observed sandstone pressures. At Macondo, there is a sharp increase in mudstone velocity across the M56 interval. The average mudstone velocity (Fig. 2.3B, thick black line) is 11,000 ft/s (3,350 m/s) across the M57 interval (17,250-17,640 ft z_{ss} or 5,258-5,377 m), but average mudstone velocity drops to 9,500 ft/s (2,900 m/s) across the M56 interval (17,640-18,250 ft z_{ss} or 5,377-5563 m). Although not shown, resistivity and density also increase in this interval, reflecting the increased compaction. In contrast, at MC 562-1, the velocities show a continuous and gradual increase with depth (Fig. 2.3E, thick black line). Likewise, our mudstone pressure estimation (Fig. 2.3D, blue line) is nearly continuous across the M56 at MC 562-1 in contrast to the pore pressure regression at Macondo.

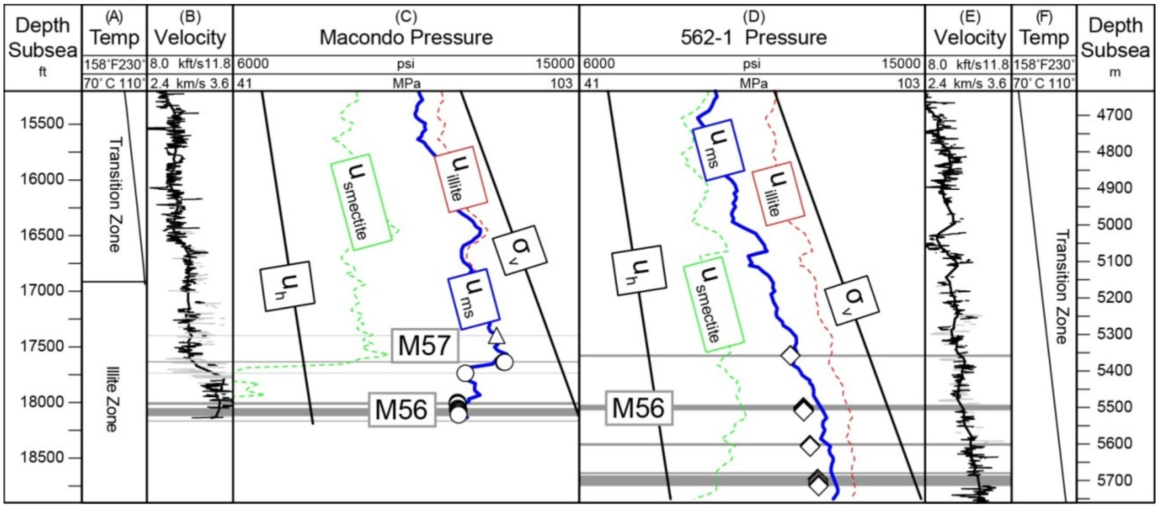

Figure 2.3 Temperature, mudstone velocity, and pressure vs. depth at the Macondo and MC 562-1 wells through the M56 reservoir. The modeled mudstone pressure, u_{ms}, (blue line) decreases abruptly at Macondo (C) whereas the mudstone pressure increases continually at MC 562-1 (D). The green and red lines represent the modeled pore pressure for smectitic (green) and illitic (red) mudstone model endmembers as described in the Methods section. Open symbols record the sandstone pressures. The temperature at the level of the M56 reservoir is 20° C greater at Macondo than at MC 562-1 (A vs. F) (See SI). The velocity log increases at the M56 level at Macondo whereas it rises continuously at MC 562-1 (B vs. E).

2.2.5 Basin Hydrodynamics

We integrate the observations at the Galapagos Field and Macondo wells with the map of the M56 surface to interpret overpressure across the region (Fig. 2.4A). We have shown constant aquifer overpressure in the M56 at both locations so we assume u_a* remains constant between them (Fig. 2.4, green). From the seafloor down, the mudstone overpressure increases linearly, subparallel with the lithostatic stress as is observed at both Macondo and Galapagos Field (Fig. 2.2 and 2.3). At Galapagos Field, the mudstone overpressure is approximately continuous with the sandstone overpressure (Fig. 2.3D). In contrast, to capture the pore pressure regression at Macondo, there is a reversal in the mudstone overpressure trend as the M56 is approached (Fig. 2.3C); this results in a return to cooler colors. Beneath the M56, mudstone overpressure again increases. Contours are connected between wells by assuming a linear change in the mudstone overpressure gradient. Contouring adjacent to the M56 assumes the pore pressure regression, if present, is approximately the same distance from the M56 as is observed at Macondo (Fig. 2.4A, dashed black line).

This overpressure field is also expressed in a plot of overpressure vs. depth below seafloor (Fig. 2.4B). In this view, the constant overpressure of the reservoir is illustrated with a vertical black line. The overpressure in the bounding mudstone away from the reservoir is shown with white lines that represent both Macondo and Galapagos Field. In this view, it is clear that at depths below seafloor greater than present at Galapagos Field, the M56 pressure is lower than the pressure in the bounding mudstones.

The overpressure cross-section is analogous to a fluid potential map: water flows orthogonally to the overpressure contours within material of isotropic permeability. Flow within the mudstone is illustrated by black arrows. In areas where there is a pore pressure regression (Fig. 2.4A, area between the dashed line and the M56), flow is focused toward the M56. Elsewhere flow is upward: pore pressure gradually dissipates as fluids flow to the seafloor. We have suggested that the Galapagos Field and Macondo reservoirs are hydraulically connected, and this is inferred by their nearly identical aquifer overpressures. In fact, the aquifer pressure at Galapagos Field is interpreted to be 47 psi (0.32 MPa) greater than at Macondo. In a 2-D view, this implies flow from Galapagos Field towards Macondo. Although the pressure difference is small, it can drive a lateral flow rate of 200 mm/year given the 300 mD permeability that is estimated for these sandstones.

It is well recognized that in many basins, regionally connected high-permeability aquifers at a nearly constant overpressure are encased in low-permeability overpressured mudstone such as is illustrated here in the M56 (Flemings and Lupa, 2004; Merrell et al., 2014; Walker et al., 2012; Yardley and Swarbrick, 2000). A key question in these systems is how the aquifer pressure relates to the bounding mudstone pressure. One common interpretation is that the aquifer pressure at some location exceeds the least principal stress. At this location, the pore pressure bleeds off through fractures such that the aquifer is fixed to the least principal stress (Reilly and Flemings, 2010; Seldon and Flemings, 2005). If the M56 reservoir extends up to 7,500 ft z_{sf} (2,300 m), then at that depth, the pore pressure would equal the overburden stress and hydraulic fracturing would have begun (Fig. 2.4B ‘e’). In fact, we cannot find a location within the mapped area where the M56 sandstone reaches these shallow depths. However, this could occur outside of the mapped area or underneath salt, where we are unable to map (Fig. 2.1B, pink areas). An alternative interpretation is that the aquifer pressure is controlled by the pore pressure of the bounding mudstone. In this model, where the mudstone is at a higher pore pressure than the aquifer, fluid flows into the aquifer and where the mudstone is at a lower pore pressure, fluid flows out of the aquifer. The aquifer pressure is a complex average of the mudstone’s pore pressure and permeability and the reservoir geometry (Flemings et al., 2002; Gao and Flemings, 2017). Unfortunately, we cannot resolve the sandstone geometry or extent outside of the mapped area, so we cannot determine whether this mechanism is occurring.

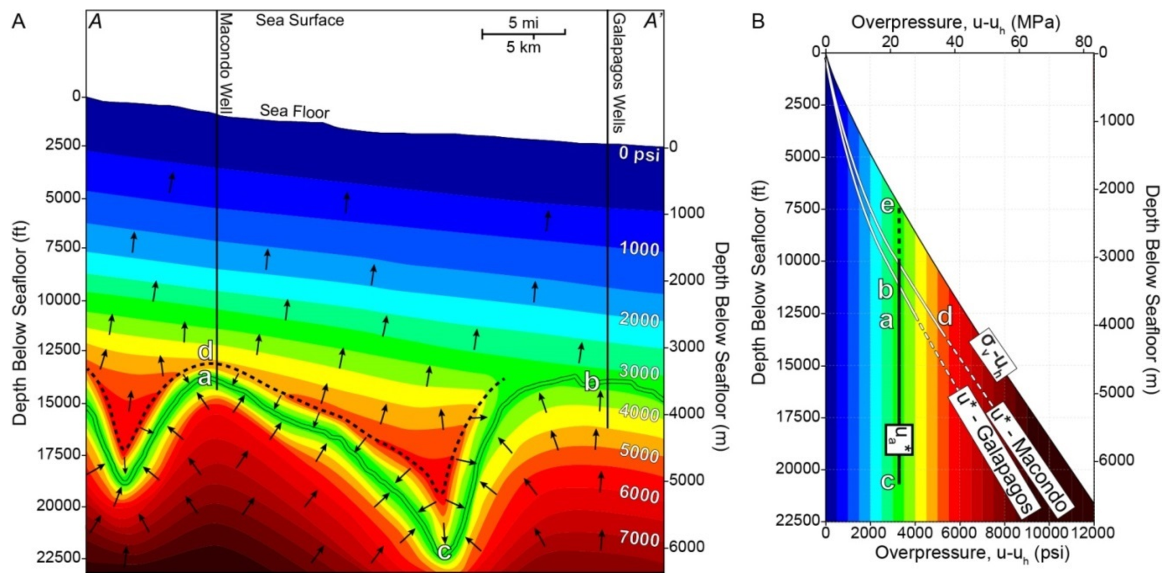

Figure 2.4 A) 2-D overpressure cross-section spanning A-A' (located in Fig. 2.1). Cooler colors indicate lower overpressure and warmer colors indicate higher overpressure. Arrows indicate the flow direction of pore fluid expelled during compaction. The vertical overpressure gradient within the mudstone (contour spacing) decreases from A to A' based on observations at the Macondo and Galapagos Field wells. The black dashed line approximates the flow divide. B) Overpressure vs. depth below seafloor. The black line records constant overpressure in the M56, and becomes dashed above the mapped depth range. White lines approximate mudstone pore pressures at each well location and become dashed below well control. Overpressure calculations use a hydrostatic gradient of 0.465 psi/ft, which is based on an aquifer pore-water density of 1.073 g/cm^3. Key locations are labeled on both figures: a) M56: Macondo b) M56: Galapagos Field c) M56: deepest mapped depth below seafloor d) Top of Macondo pore pressure regression (contour reversal) e) Fracture initiation begins where aquifer overpressure converges with overburden stress (σ_v-u_h) (location not mapped, shown on B only)

2.3 Implications of the Pore Pressure Regression

The pore pressure regression hindered the drilling and temporary abandonment programs at Macondo. Within the exposed borehole, a single mud weight is used to maintain pressure (1) below the fracture pressure to avoid drilling fluid (mud) loss into the formation and (2) above the pore pressure to prevent flow into the borehole. The difference between the maximum equivalent mud weight (EMW, the average fluid density projected to the drill floor, see SI) that causes fracturing and the minimum EMW that controls the pore pressure is the drilling window. During operations in the deepest hole section at Macondo, the formation was exposed below the base of the 9 7/8” liner (Fig. 2.5C). Along this hole section, the drilling window narrowed to essentially zero (Fig. 2.5A and B, yellow rectangle): its left bound defined by pore pressure in the M57 of 14.20 ppg (1.702 g/cm^3) EMW and its right bound defined by the M56 fracture pressure of 14.3-14.4 ppg (1.714-1.726 g/cm^3) EMW.

This narrow window created challenging drilling conditions. Gas flowed into the well from the M57 (Fig. 2.5A, open triangle), indicating that borehole pressures had dropped below the pore pressure. On three occasions, mud was lost into the formation (Fig. 2.5A, brown triangles), indicating that borehole pressures had exceeded the fracture pressure. In fact, these events constrain the drilling window. The two mud loss events into the M56 document a lower fracture pressure within this interval than in the upper half of the hole section (Fig. 2.5A, brown square and uppermost triangle). This drop in fracture pressure (least principal stress) is most likely a result of the reduced pore pressure, but could also be due to the mechanical properties in sands relative to mudstones (Daines, 1982). The lack of sufficient drilling window meant that BP was forced to terminate drilling without fulfilling all of its objectives, which included drilling to 19,560 ft z_{ss} (5,962 m).

The narrow drilling window also complicated installation of the 7” production casing. Wireline logs were stopped at 18,210 ft z_{ss} (5,550 m), short of reaching the bottom of the borehole at (18,274 ft z_{ss} or 5,570 m), and this could suggest significant debris accumulation since drilling was completed. The borehole was then cleaned prior to casing installation, but the casing also encountered debris before reaching its target depth of 18,218 ft z_{ss} (5,553 m). The accumulation of debris after two borehole cleanings, in conjunction with the borehole widening recorded by the caliper log (Fig. 2.5C, red), could indicate borehole instability. When borehole pressure is reduced relative to the least principal stress, circumferential stress on the borehole wall increases, which can lead to compressional wellbore failure and debris (Zoback, 2007). At trial, it was ruled that compressional failure of the casing due to contact with bottom-hole debris during installation was a primary cause of the blowout (Barbier, 2015).

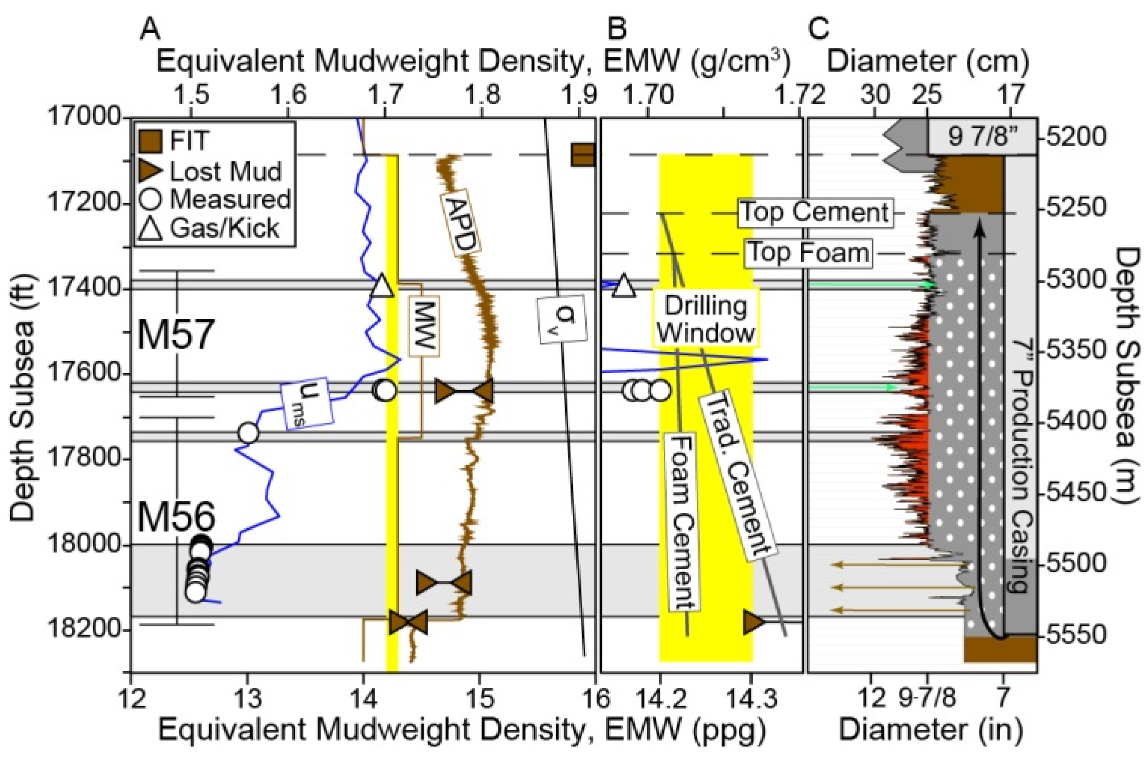

Figure 2.5 A) Pressure and stress gradient vs. depth expressed as an equivalent mud weight (EMW, the average fluid density from the drill floor necessary to reproduce the downhole pressure, see SI). Lost mud events record the lower and upper bounds of the fracture pressure (brown triangles, see SI); the formation integrity test (FIT, brown square) records a lower bound of the fracture pressure. The APD is the

annular pressure while drilling as recorded on the drill string. The MW records the static pressure from drilling mud weight measured at surface conditions. To prevent influx of M57 pore fluids (C, green arrows), the static borehole pressure had to be kept above 14.20 ppg (1.702 g/cm^3) EMW. However, to avoid fracturing the M56 (C, brown arrows), the dynamic pressure had to be kept below 14.3-14.4 ppg (1.714-1.726 g/cm^3) EMW. The zone in yellow shows the range of pressures that had to be maintained (the drilling window). B) Pressure and stress gradient vs. depth during temporary abandonment. The two gray lines represent the static pressure that would be induced by foamed cement (left, 14.5 ppg or 1.738 g/cm^3) vs. a traditional cement (right, 16.74 ppg or 2.006 g/ cm^3). C) Wellbore cross-section during temporary abandonment. Cement is pumped through the bottom of the casing and up the annulus. White circles differentiate the foamed cement from the traditional cement cap above. Red shows caliper measurements greater than the width of the under-reamer.

Finally, the narrow drilling window impacted the approach used to cement the production casing in place. To maintain pressures along the cement column within the drilling window (Fig. 2.5B, gray lines within yellow rectangle), BP and Halliburton used 16.74 ppg (2.006 g/cm^3) cement foamed with nitrogen to reduce its downhole density to 14.5 ppg (1.738 g/cm^3) to keep dynamic borehole pressures below 14.583 ppg EMW (1.747 g/cm^3) (Beck, 2011; Hafle and Mueller, 2010). The particular foam cement mixture was shown to be unstable during testing prior to and after the blowout (Barbier, 2015; BP, 2010e). At trial, it was accepted by both parties that this cement failed, and it was BP's position that failure of the cement was the primary cause of the failure to seal the well (Barbier, 2015; BP, 2010d; Turley, 2014).

2.4 Materials and Methods

2.4.1 Mudstone Pore Pressure

Based on the lithology and grain size of cuttings recovered during drilling, we estimate that mudstone composes 80% of the drilled section at Macondo. In fact, rapid deposition of this low permeability material is the primary source of overpressure in the

Gulf of Mexico (Dugan and Sheahan, 2012). It is not possible to measure the pressure within these low permeability mudstones directly. Instead, pore pressure is commonly estimated from the compaction state (porosity) of the rock. In this approach, porosity is a function of effective stress and proxies for porosity such as resistivity, density, or velocity are often used (Hart et al., 1995; Zhang, 2011). These petrophysical measurements are correlated to effective stress. Once the correlation is established, then σ'_v can be determined given an estimate of the compaction; this is used to calculate pore pressure because overburden is known ($u = \sigma_v - \sigma'_v$).

In deepwater Gulf of Mexico Neogene sediments, the porosity-effective stress relationship is influenced by clay diagenesis of which the smectite-to-illite transformation (S/I) is considered the most significant (Dutta, 1986; Lahann et al., 2001; Wilhelm et al., 1998). It is inferred that more illitic material has a lower porosity at a given effective stress than a more smectitic material (Lahann, 2002; Mondol et al., 2007). We follow ref. (Lahann, 2002) and assume:

$$\phi - \phi_m = \phi_0 e^{-B\sigma'_v} \qquad \text{Eq. 2.1}$$

The left side of Eq. 2.1 is the total porosity, ϕ, less the pore volume that is filled by clay-bound water, ϕ_m. The molecular structure of smectite has an easily hydratable interlayer, whereas illite does not (Colten-Bradley, 1987); thus $\phi_{m,i} < \phi_{m,s}$. The right side of Eq. 2.1 describes the compaction behavior of the non-clay-bound water and is commonly used to describe porosity loss with effective stress (e.g. (Hart et al., 1995; Rubey and Hubbert, 1959)). It is not well known whether ϕ_0 or B vary with the degree of the S/I transformation, so we assume that they are constant per Lahann (2002).

We calibrate the model first by determining the effective stress within the mudstones adjacent to where pressure has been measured directly in sandstones. We assume that $u*$ in the mudstone equals $u*$ measured in the nearby sandstone (e.g. (Merrell et al., 2014)), and use the mudstone pressure to calculate σ'_v. Next, we determine the porosity at each location from the velocity log after (Issler, 1992):

$$\phi = 1 - \left(\frac{v}{v_{\mathrm{ma}}}\right)^{1/x} \qquad \text{Eq. 2.2}$$

where v_{ma} is matrix velocity, v is the velocity log measurement, and x is an empirically derived acoustic formation factor exponent. We assume x = 2.19 and v_{ma} = 14,909 ft/s (4,545 m/s) following precedent for Gulf of Mexico Neogene sediments (Hart et al., 1995; Issler, 1992; Merrell et al., 2014). As illustrated in Fig. 2.6, the shallow locations with cooler in-situ temperatures have a high porosity for a given effective stress, whereas the deeper locations with warmer in-situ temperatures have a lower porosity for the same effective stress. The contrast is most apparent σ'_v = 1500 psi (10 MPa) and ϕ varies by as much as 9 porosity units between the shallow and deep measurements. The difference is interpreted to reflect a loss in the clay-bound water ϕ_m as the smectite in the mudstone is converted to illite with burial.

The S/I transition is incorporated into the model as follows. We assume that the clay-bound water porosity loss due to S/I transformation is linearly proportional to temperature, and that transformation begins at 70° C and plateaus at 110° C. This approximates the main phase of S/I transformation (Bjørlykke, 1999; Hoffman and Hower, 1979; Pollastro, 1993) without additional constraints on depositional history and chemical composition (Huang et al., 1993). We follow Lahann (2002) and assume ϕ_m =

0.12 for smectitic mudstone and ϕ_m = 0.03 for illitic mudstone. Based on these assumptions, the clay-bound water porosity is:

$$\phi_m = \left(1 - \frac{T - T_s}{T_i - T_s}\right)(\phi_{m,s}) + \frac{T - T_s}{T_i - T_s}(\phi_{m,i}) \qquad \text{Eq. 2.3}$$

where T is temperature, and *s* and *i* designate smectite or illite. We combine Eq. 2.2 and 2.3, and solve for ϕ - ϕ_m for all the ϕ vs. σ'_v points in Fig. 2.6. We then use least-squares regression and find ϕ_0 = 0.22 and B = 2.9E^{-4} psi^{-1} (Fig. 2.6, black line).

Given B and ϕ_0, Eq. 2.1 is then used to estimate mudstone pressure along the borehole (Fig. 2.2, blue line) given a value of ϕ_m based on temperature. We picked mudstones along the borehole at 30-40 ft (9-12 m) intervals and applied a 5-point moving average. For each mudstone point, we calculate ϕ from velocity (Eq. 2.2) and ϕ_m from temperature (Eq. 2.3). ϕ and ϕ_m are entered into Eq. 2.1, solving for σ'_v and then *u*.

We apply this method (calibrated at Macondo) to estimate the mudstone pressure at MC 562-1 (Fig. 2.3). The close match between the estimated mudstone pressures and the measured sandstone pressures, independent of local calibration, supports the accuracy of our method within this region. Effective stresses at MC 562-1 are roughly 500-1,300 psi (3-9 MPa) higher than at Macondo (outside of the pressure regression). Mudstone sonic porosities are similar in both wells, but the temperature gradients are different. The Macondo well has an average temperature gradient of 28.4° C/km versus 26.1° C/km at MC 562-1 (see SI). The lower temperature gradient and deeper water at MC 562-1 results in M56 temperatures that are nearly 20° C lower than M56 temperatures at Macondo. The lower temperature indicates that the mudstone at MC 562-1 is more smectitic than the mudstone at Macondo for a given depth, so the sonic porosities transform to higher σ'_v (Fig. 2.6).

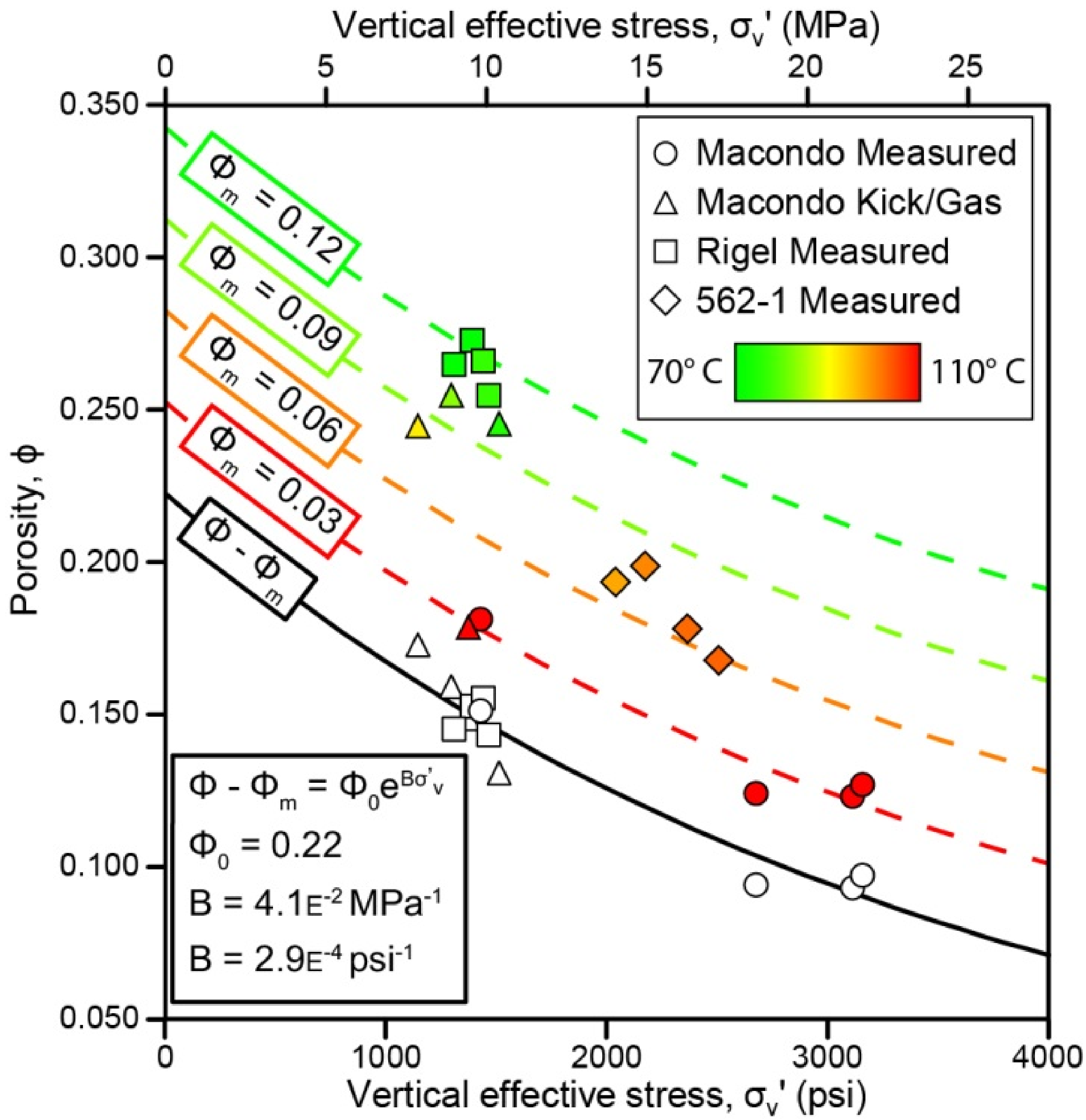

Figure 2.6 Mudstone porosity vs. effective stress. Color-coded symbols denote in-situ temperature for each mudstone porosity-effective stress calibration point. The points are corrected for clay-bound water porosity (open symbols) and then are used to calibrate Eq. 2.1 (black line). Dashed lines show the porosity-effective stress relationships for different temperatures (color coded) and clay-bound water porosities, ϕ_m. Measurements from the M56 (σ'_v >2500 psi or 17 MPa) are corrected for hydrocarbon buoyancy. Porosity is estimated from velocity (Eq. 2.2).

2.4.2 Macondo Pore Pressure Profile

The overburden stress is calculated by integrating the weight of the water column and the weight of the overlying sediment. Bulk density is frequently measured during well logging operations. We combine density log data from nearby wells in portions of the Macondo well where no density data were acquired. Logs are corrected to account for borehole washout and for presence of hydrocarbons. In regions where no density data are available, a velocity-to-density transform is used (Gardner et al., 1974). Finally, if neither density nor velocity data are present, an exponential interpolation between density above and below the interval is used (Athy, 1930).

Industry routinely measures pore pressure and takes fluid samples from relatively permeable formations with wireline tools (e.g. Modular Formation Dynamics Tester™, MDT) and directly from the drill string (e.g. Geotap™). At the Macondo well, BP recorded 21 measurements in four sandstones at the base of the well between 17,600 and 18,150 ft z_{ss} (5,364 and 5,532 m) (Fig. 2.2, circles). 70 MDT pressures were recorded in nine sandstones between 8,900 and 12,500 ft z_{ss} (2,700 and 3,800 m) (Fig. 2.2, squares) at the older MC 252-1 (Texaco) well, located 1.27 miles (2.04 km) SW of the Macondo well. These MDT measurements are corrected to the Macondo well location assuming continuous stratigraphy parallel to the seafloor. Each MC 252-1 (Texaco) measurement is projected up 217 ft (66 m) based on the seafloor depth difference between wells. The corresponding pressure correction is 96 psi (0.66 MPa) assuming a hydrostatic gradient.

We also constrain pore pressure from fluid influxes into the borehole (kicks) and elevated gas levels detected in the incoming drilling mud. Kicks and high gas occur when pore pressure exceeds hydraulic pressure from the drilling fluid in the exposed borehole.

Six such events occurred during drilling operations (Fig. 2.2, 2.3, and 2.5, open triangles). Using drilling information prior-to, during, and after an event, we estimate the location and pore pressure.

Drilling information includes the location of sandstones, length of exposed borehole, gas content of the incoming mud, surface mud weight, equivalent static density, equivalent circulating density, and shut-in drill pipe pressure. The equivalent mud weight is another way of expressing pressure using the average density of the drilling fluid from the drill floor to a location in the borehole:

$$\mathrm{EMW\ (ppg)} = \frac{\mathrm{pressure\ (psi)}}{z_{df}\ \mathrm{(ft)}} * 19.25 \frac{\mathrm{ppg}}{\mathrm{psi/ft}} \qquad \text{Eq. 2.4}$$

where z_{df} is true vertical depth measured from the drill floor of the rig. The equivalent static density (ESD) is the downhole pressure experience by the formation with the mud pumps off and includes density changes due to suspended cuttings, gas content, and mud compressibility. The equivalent circulating density (ECD) expresses the dynamic pressure experienced by the formation as drilling fluids are circulating, which includes the additional pressure due to friction.

Drilling information is also used to constrain the fracture pressure. The equivalent static density and equivalent circulating density provide the upper and lower bounds for determining fracture pressure during mud loss events (Fig. 2.5, brown triangles). Fracture pressure is also constrained using formation integrity tests, FIT (Fig. 2.5, brown square).

2.4.3 Aquifer Pressure

We determine the M56 aquifer overpressure at the Macondo well to be 3,386 psi (23.35 MPa), but it could be as high as 3,436 psi (23.69 MPa). At the Galapagos Field development, the M56 aquifer overpressure is tightly constrained to be 3,433 psi (23.67 MPa). Below, we describe how we determine these values. The aquifer overpressures are constrained with direct pressure measurements in the M56 sandstones at the Macondo well and three wells at the Galapagos Field development. These wells are chosen because the pressure measurements were made before production at either location; thus, the measurements are interpreted to record the in-situ pressures unaffected by production or release (Fig. 2.1, red circles and yellow stars). Many of the measurements were made within hydrocarbon-bearing sections. To determine the aquifer overpressure in such cases, the buoyant effect of the hydrocarbon column must be removed (e.g. (Flemings et al., 2002)). Specifically, the hydrocarbon pressure is projected down to the hydrocarbon-water contact (HWC) using the MDT-derived hydrocarbon density (Fig. 2.7). For each well at Macondo and Galapagos Field, we constrain the HWC, hydrocarbon-phase density, and water-phase density with log, MDT and seismic data. We then calculate aquifer overpressure at Macondo and Galapagos Field, taking into account pore-water density ($u_a{*} = u - \rho_{pw} g z_{ss}$).

Given direct pressure measurements in hydrocarbon-bearing sandstone, the challenge is to infer the hydrocarbon-water contact. At Macondo, we interpret that the 4-way closure of the M56 structure (Fig. 2.1B) was filled to its spill point. We interpret a structural crest at 17,720 ft z_{ss} (5401 m), a saddle at 18,375 (5601 m), and thus a column height of 655 ft (200 m) by depth correcting BP's predrill interpretation (BP, 2009d). BP interpreted that the seismic amplitudes supported this filled-to-spill interpretation for the HWC (BP, 2009d). We calculate $u_a{*}$ to be 3,386 (23.35 MPa) using a hydrocarbon gradient of 0.24 psi/ft (5.43 MPa/km) and a pore-water gradient of 0.465 psi/ft (10.52 MPa/km). It is possible that hydrocarbon charge limitation could result in a shallower HWC, though this is rare in this petroleum-rich area. MC 253-1 (Fig. 2.1, northernmost blue dot) provides the deepest hydrocarbon-bearing penetration of the M56 in the Macondo structure at 18,150 ft z_{ss} (5,532 m), which yields u_a* of 3,436 psi (23.69 MPa)

MC 519-1, MC 519-2, and MC 562-1, the three Galapagos Field development wells, penetrated HWCs, a water leg, and a hydrocarbon leg respectively in the M56 (Fig. 2.7). Direct measurement of water-phase pressures and gradients provides accurate aquifer overpressure calculations. At MC 519-1, two vertically stacked sandstone lobes comprise the M56. Each lobe shows a distinct HWC, but both share a u_a* of 3,436 psi (23.69 MPa). MC 519-2 encountered only water in the M56, which yields u_a* of 3,430 psi (23.65 MPa). We use these MDT measurements to estimate the M56 pore water density of 0.465 psi/ft (10.52 MPa/km). MC 562-1 encountered hydrocarbon in the M56 and did not penetrate a HWC. An aquifer pressure calculation that assumes the HWC is just below the sandstone yields a u_a* of 3,433 psi (23.67 MPa), which is nearly identical to those observed in the Noble wells. We use the average, 3,433 psi (23.67 MPa), to describe a single u_a* for the Galapagos Field development.

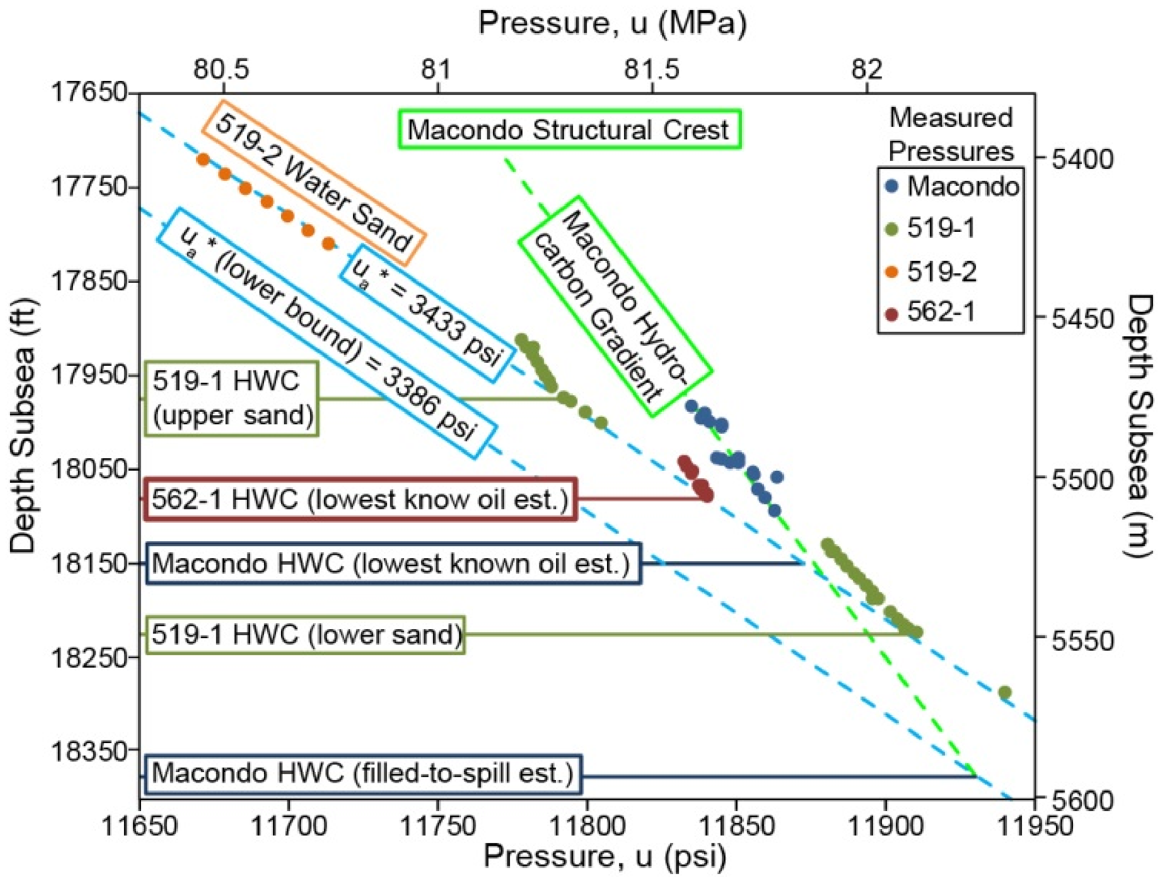

Figure 2.7 Pressure vs. depth of M56 MDT measurements from four wells. Water-phase pressures for the Macondo and Galapagos Field structures are shown as blue dashed lines. A green dashed line denotes the M56 hydrocarbon gradient at Macondo. Solid horizontal lines locate observed and estimated hydrocarbon-water contacts.

2.4.4 Temperature Profiles

We determined the temperature profiles at Macondo and MC 562-1 using temperatures recorded during MDT pore fluid sampling (Fig. 2.8, open symbols). Temperatures between 113.3 and 113.7° C were recorded at three MDT sample points in the Macondo well between 13,008 and 13,064 ft z_{sf} (3,965 and 3,982 m) (Fig. 2.8, rectangles). At MC 562-1, four MDT sample points record temperatures between 93.5 and 98.4° C for depths between 11,633 and 12,316 ft z_{sf} (3,545 and 3,754 m) (Fig. 2.8, diamonds). BP's temperature model for Macondo (Fig. 2.8, upper black line) (BP, 2010g) is 3.8° C higher than the average of the recorded temperatures in the M56 (Fig. 2.8, rectangle error bars). We assume this difference reflects a correction for borehole cooling. At Macondo, MDT measurements were acquired three days after drilling was completed, which is comparable to the four day gap at MC 562-1. Therefore, we apply the same 3.8° C correction to the measurements at MC 562-1 (Fig. 2.8, diamond error bars). Our temperature model for MC 562-1 assumes a linear decrease from the corrected reservoir measurements to the seafloor (Fig. 2.8, lower black line). Seafloor water temperatures in deepwater Gulf of Mexico approach 4° C (Forrest et al., 2005) for the water depths observed at Macondo and MC 562-1.

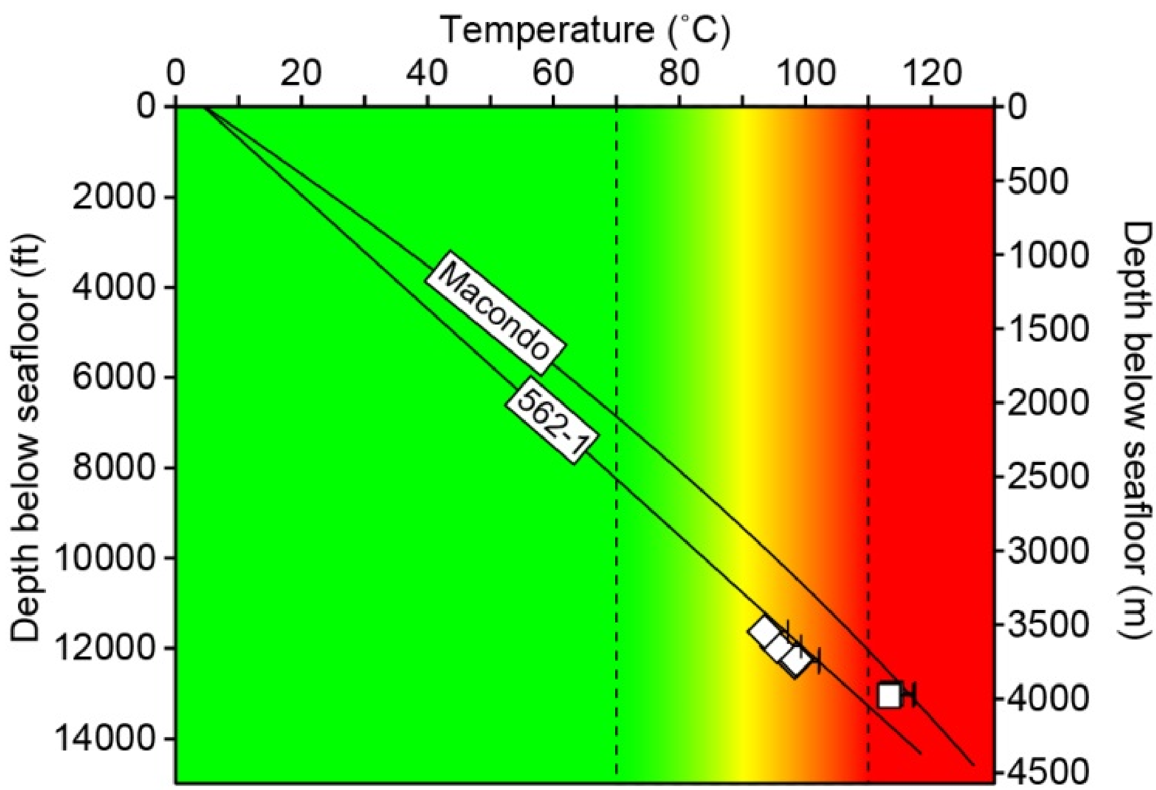

Figure 2.8 Temperature vs. depth below seafloor at Macondo and MC 562-1. Open

symbols show MDT pore fluid temperature measurements. Error bars projected from the right represent a correction for borehole cooling. BP's temperature model is used at Macondo; MC 562-1 temperatures are modeled using a linear projection to the seafloor. Color scheme and dotted lines show the temperature-derived S/I transition zones.

Chapter 3: Stress Analysis

ABSTRACT

A least principal stress profile of the Macondo well is estimated using an empirically calibrated effective stress ratio, *K*. Five formation pressure integrity tests (FPITs) are analyzed to determine the least principal stress at discrete locations along the wellbore. For the five FPITs, *K* varies between 0.51 and 1.13 with a mean of 0.78. The pore pressure prediction (Chapter 2.4.1), overburden stress model (Appendix A), and *K* = 0.78 are used to calculate the least principal stress along the borehole. The operator incurred losses while drilling the Macondo well, and fracture gradients are interpreted at eight of these mud loss event locations. The fracture gradient decreases by ~1 ppg EMW as the reservoir interval is approached. Initial losses in the reservoir interval may have reduced the fracture gradient, perhaps contributing to subsequent losses. The least principal stress model captures the trend in the fracture gradients interpreted from lost circulation pressures. Therefore, the reduction in pore pressure across the reservoir interval appears drive the reduction in least principal stress and fracture gradient.

3.1 INTRODUCTION

The fracture pressure of a formation describes the borehole pressure at which perceptible fluid loss occurs into fractures (Zhang and Yin, 2017). A detailed understanding of the fracture pressure (fracture gradient when displayed in EMW space) is critical for well design and control. The fracture pressure in impermeable rocks is controlled by the far-field stresses, local stress concentration, and tensile strength (Detournay and Carbonell, 1997; Hubbert and Willis, 1972). Stress concentration and tensile strength can vary in time and space due to a variety of factors (e.g. repeated fracture (Addis et al., 1998), borehole shape, existing fractures, temperature (Zoback, 2007); wellbore strengthening techniques (Mehrabian et al., 2017)). Therefore, I focus on interpreting the least principal stress at the Macondo well using Formation Pressure Integrity Tests (FPITS). I then model the least principal stress with a calibrated effective stress ratio and compare the results to the fracture pressures recorded by lost circulation events.

This chapter serves as a comprehensive investigation of fracture pressures and least principal stress at the Macondo well. Existing analyses are fragmented (BP, 2009c), lack supporting data (BP, 2010e), document lessons learned (Lebleu, 2010a), or argue regulatory compliance (Huffman, 2011). Here, I document the theory, data, analysis, assumptions, and model used in the determination of least principal stress in the Macondo well.

3.2 METHODS

3.2.1 Formation Pressure Integrity Tests

Formation-pressure integrity tests (FPITs) are used primarily to gauge the integrity of a casing shoe, but they also are used to interpret the fracture properties and least principal stress of the formation (Postler, 1997). FPITs fall into three categories: formation integrity tests (FIT), leak-off tests (LOT), and extended leak-off tests (XLOT). In all three cases, a 10 to 50 ft section of new formation is drilled below a casing point (Section 250.427, BOEM regulations). The annulus is then closed, and mud is pumped into the well, which increases the borehole pressure. If the borehole pressure reaches a predetermined value without a break in slope in volume pumped vs. pressure, then test is considered a FIT. The test failed to initiate a fracture because borehole pressure did not 1) exceed the least principal stress or 2) exceed the near-wellbore stresses and tensile strength (whichever is lower).

A description of an idealized XLOT from Alberty and McLean (2014) is paraphrased below. During an XLOT, the leak-off pressure (LOP) is interpreted from a break in slope in volume pumped vs. pressure (Fig. 3.1). The LOP is interpreted to record the pressure at which fracture growth begins. If pumping continues after the LOP is observed, pressure may continue to increase, reach a local maximum, then decrease as additional fluid is pumped into the well (Fig. 3.1). This peak is known as the breakdown pressure (FBP) and it is interpreted to record uncontrolled fracture growth away from the wellbore. As more fluid is added to the system, the pressure stabilizes below the FBP at the fracture propagation pressure (FPP). The FPP is interpreted to record stable far-field fracture growth away from the wellbore. When pumping is stopped, pressure in the shut-in well decreases rapidly. The instantaneous shut-in pressure (ISIP) is defined as the first inflection point (slope decrease) (Postler, 1997) or the point at which rapid decay transitions to gradual decay (Zoback, 2007) in the surface pressure vs. time shut-in data. During an XLOT, the test is often repeated to ensure a consistent response (Fig. 3.1, blue) and better capture the far-field stresses.

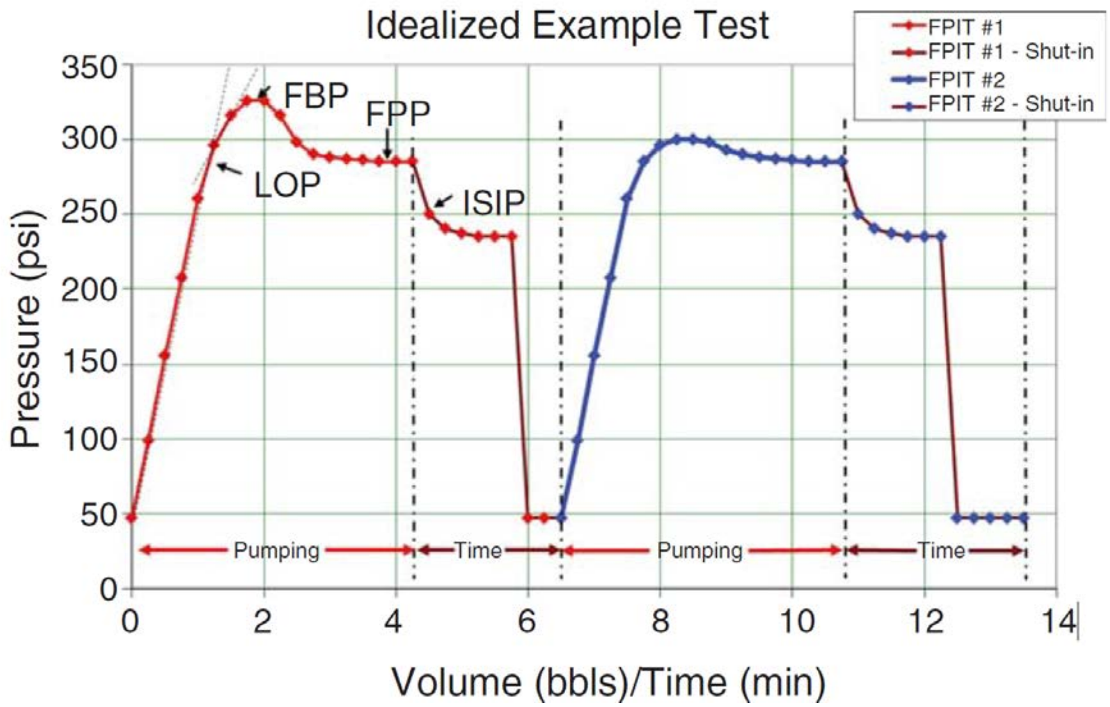

Figure 3.1 Idealized XLOT from Alberty and McLean (2014). The test records the pressure vs. the volume pumped at a constant rate during the pump-up phase and pressure vs. time during the shut-in phase. The leak-off pressure (LOP), breakdown pressure (FBP), fracture propagation pressure (FPP) and instantaneous shut-in pressure (ISIP) are noted. This plot illustrates the repeated test in blue.

At the Macondo well, 17 FPITs were released during MDL 2179 proceedings (Alberty, 2010), and I display and analyze the final test from the 22”, 18”, 16”, 13-5/8”, 11-7/8” and 9-5/8” casing shoes. Using the above as a guide, I interpret these FPITs as follows. I calculate dP/dV and dP/dt using a forward difference approximation, then

d^2P/dV^2 and d^2P/dt^2 with a backward difference approximation. To determine the LOP, I graphically locate the bend in slope (e.g. Postler (1997)) and chose the corresponding decrease in d^2P/dV^2. To determine the ISIP, I look for the deviation in slope from rapid to gradual (e.g. Zoback (2007) pg. 212) and use the first positive value of d^2P/dt^2 during the shut in phase. Table 3.1 shows an example calculation for the 13-5/8" FPIT. Many of the tests do not adhere to the idealized results described above. For simplicity and because many of the tests display curved pump up behavior, I eschew fitting curves to the data. Instead, PFIT interpretations are made at the discrete recorded points.

Table 3.1: 13-5/8" FPIT complete pump up and shut in data. The first derivative calculations use a forward difference approximation and the second derivative calculations use a backward difference approximation. During the pump up phase, d^2P/dV^2 hovers around 0 before dropping to -60 at the LOP. During shut in, d^2P/dt^2 is -11 psi/min^2 from 0 to 1 min then jumps to 88 at 2 m as the slope of the pressure decline flattens.

Pump up			
Vol	Pressure	dP/dV (forward difference)	d^2P/dV^2 (backward difference)
bbl	psi	psi/bbl	psi/bbl^2
0	0	280	
0.5	140	130	-150
1	205	130	0
1.5	270	160	30
2	350	176	16
2.5	438	164	-12
3	520	160	-4
3.5	600	160	0
4	680	160	0
4.5	760	160	0
5	840	180	20
5.5	930	160	-20
6	1010	160	0
6.5	1090	160	0
7	1170	160	0
7.5	1250	160	0
8	1330	180	20
8.5	1420	120	-60
9	1480	0	-120
9.5	1480		

Shut in			
Time after Shut in	Pressure	dP/dt (forward difference)	d^2P/dt^2 (backward difference)
min	psi	psi/min	psi/min^2
0	1416	-94	
1	1322	-105	-11
2	1217	-17	88
3	1200	-10	7
4	1190	-3	7
5	1187	-4	-1
6	1183	-3	1
7	1180	-2	1
8	1178	-1	1
9	1177	-2	-1
10	1175		

The various FPIT measurements (LOP, FBP, etc.) are translated to downhole pressure by calculating the sum of pressure applied by the static column of drilling fluid, P_{static}, and the drill pipe pressure measured at the surface, $P_{surface}$.

$$P_{FPIT}(psi) = P_{static}(psi) + P_{surface}(psi) \qquad \text{Eq. 3.1}$$

The pressure from the static column of drilling fluid is measured with the pressure-while-drilling tool immediately prior to the test. This pressure may be expressed as the equivalent static density (ESD), which is the average borehole fluid density measured in pounds per gallon. ESD is converted to P_{static} using Eq. 2.4. The downhole pressure gauge is not used during the test because the tool communicates with the surface via mud telemetry and cannot transmit when the pumps are off.

Interpretation of the least principal stress from leak-off test measurements has been the subject of debate because of the effect of near-wellbore effects (Addis et al., 1998; Detournay and Carbonell, 1997). Some interpret the LOP as the least principal stress (e.g. Daines (1982), Zoback (2007)). Alberty and McLean (2014) suggest that the most accurate least principal stress indicator is the shut-in pressure following stable fracture growth during an XLOT. Unfortunately, during the Macondo well FPITs, the pump-up phase was cut short prior to reaching FPP. As a result, the least principal stress interpretations rely on the available LOT data and likely record some near-wellbore effects. I plot both the ISIP and LOP to inform the stress state, and cautiously use the ISIP as an approximation of the least principal stress (e.g. Zoback (2007) and Postler (1997)) even if the test is stopped prior to sustained fracture propagation.

Table 3.2: FPIT summary. The least principal stress is calculated using Eq. 3.1 and the instantaneous shut-in pressure. EMW is calculated using the true vertical depth measured from the Deepwater Horizon rig floor ($z_{df\ DWH}$).

Casing Diameter	Test #	Type	Casing Shoe True Vertical Depth (DWH rig floor)	Downhole Static Pressure (Equivalent Static Density)		Leak-off Pressure (surface)	Breakdown Pressure (surface)	Maximum Pressure (surface)	Instantaneous Shut-In Pressure (surface)	Least Principal Stress (downhole)	
			ft	ppg	psi	psi	psi	psi	psi	psi	ppg
22"	8 of 8	LOT	7952	9.99	4127	145	160	160	118	4245	10.28
18"	5 of 5	LOT	8969	10.7	4985	525		550	470	5455	11.71
16"	1 of 1	LOT	11585	11.71	7047	545		631	586	7633	12.68
13-5/8"	1 of 1	LOT	13135	12.72	8679	1420	1480	1480	1217	9896	14.50
11-7/8"	1 of 1	LOT	15093	13.78	10804	954		994	892	11696	14.92
9-7/8"	1 of 1	FIT	17158	14.52	12942			1520			

3.2.1.1 22" Casing

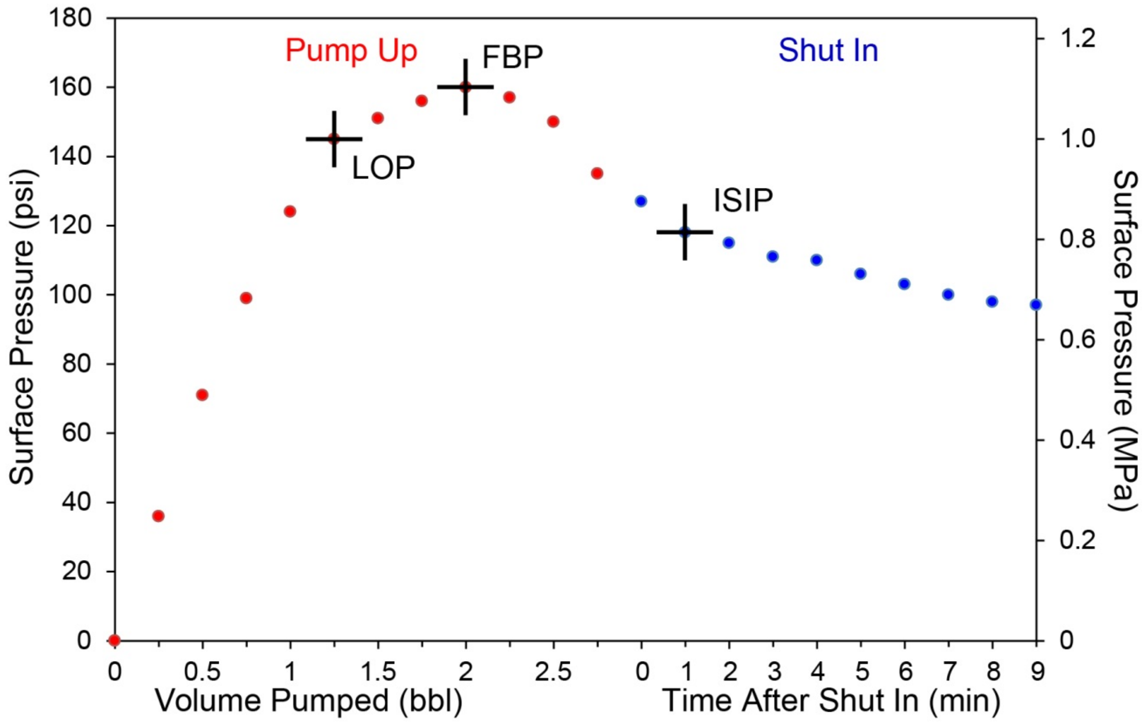

Figure 3.2 22" Shoe LOT. Test # 8 out of 8; Casing shoe = 7952 ft $z_{df\ DWH}$; ESD of 9.99 ppg or 4127 psi at shoe; LOP = 145 psi; FBP = 160 psi; ISIP = 118. Least principal stress calculated from the ISIP = 4245 psi or 10.28 ppg. This test records a clear break in the slope during the pump-up phase at 1.25 bbl. The pressure maxima followed by decreasing pressure suggests that the FPB was reached, but the pump-up stopped before a stable FPP is displayed. The slope change used to determine the ISIP during the shut-in phase is subtle, from -9 psi/min to -3 psi/min at 1 min.

3.2.1.2 18” Liner

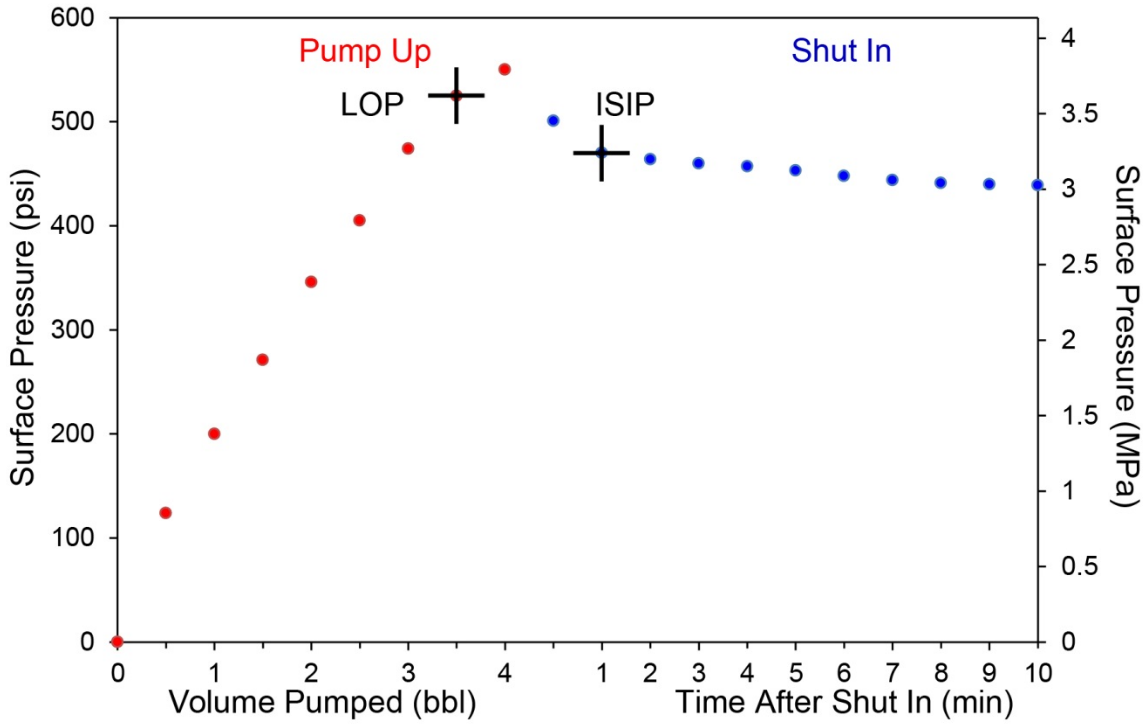

Figure 3.3 18” Shoe LOT. Test # 5 out of 5; Casing shoe = 8969 ft $z_{df\ DWH}$; ESD of 10.7 ppg or 4985 psi at shoe; LOP = 525 psi; ISIP = 470 psi. Least principal stress calculated from the ISIP = 5455 psi or 11.71 ppg. The pump-up phase was stopped immediately after the change in slope was observed between 3.5 to 4 bbl, so no FBP is recorded. I interpret the ISIP from the clear slope change at 1 min after shut-in.

3.2.1.3 16” Liner

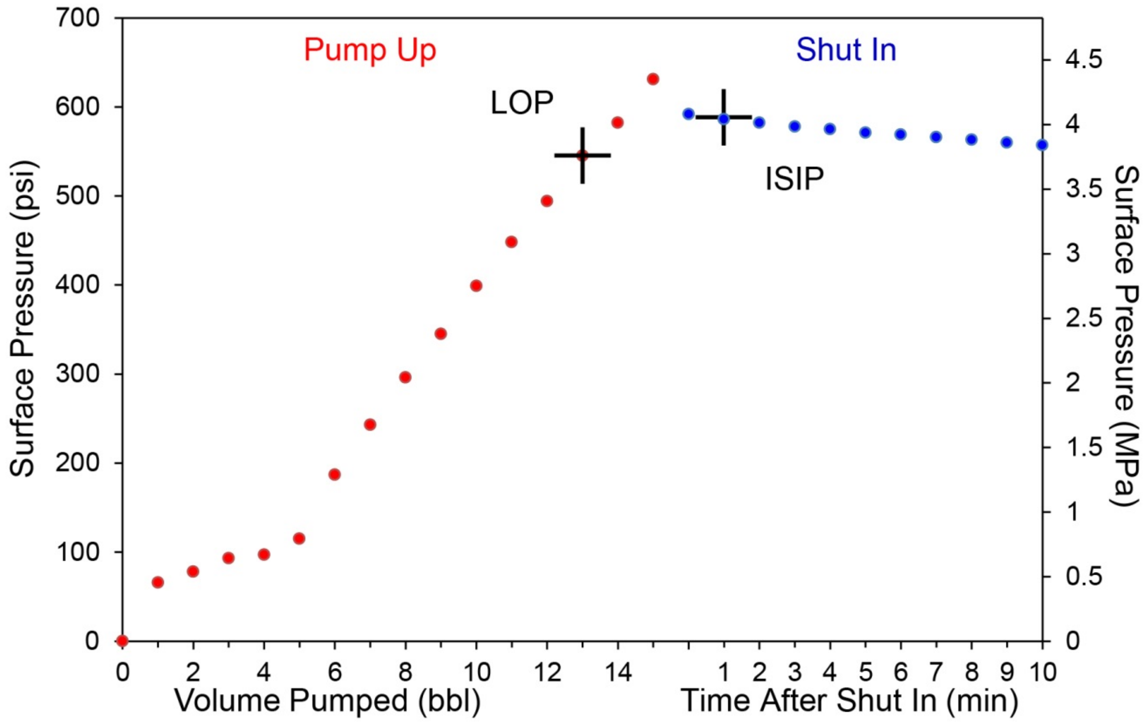

Figure 3.4 16” Shoe LOT. Test # 1 out of 1. Casing shoe = 11585 ft $z_{df\ DWH}$. ESD of 11.71 ppg or 7047 psi at shoe. LOP = 545 psi; ISIP = 586 psi. Least principal stress calculated from the ISIP = 7633 psi or 12.68 ppg. The slope decreases from 13 to 14 bbl, but then increases again from 14 to 15 bbl; this creates ambiguity in the LOP interpretation. The behavior may indicate leak-off in a near-wellbore plastic zone (e.g. Postler (1997)) and that elastic leak-off occurs at a higher pressure with continued pump-up. The ISIP is interpreted at 1 min after shut-in from the subtle slope change from -6 psi/min to -3 psi/min. ISIP is greater than the LOP, perhaps indicating that leak-off occurred at the max pressure. Alternatively, this test could be interpreted as a FIT.

3.2.1.4 13-5/8" Liner

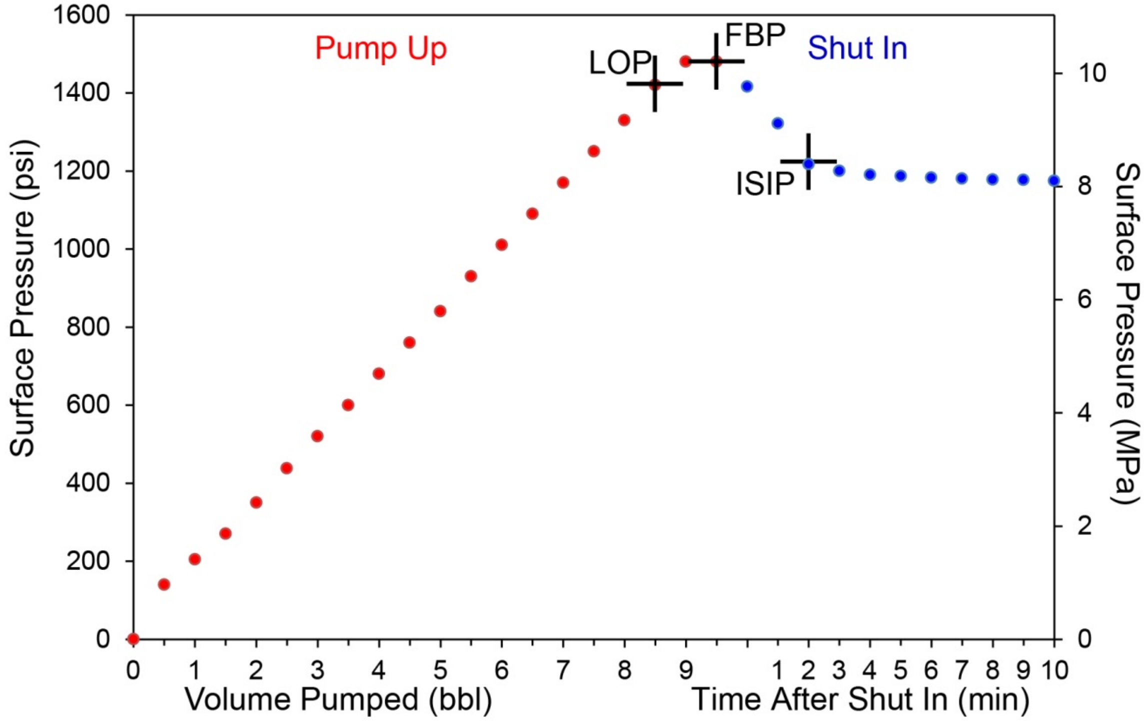

Figure 3.5 13-5/8" Shoe LOT. Test # 1 out of 1; Casing shoe = 13135 ft $z_{df\ DWH}$; ESD of 12.72 ppg or 8679 psi at shoe; LOP = 1420; FBP = 1480; ISIP = 1217 psi. Least principal stress calculated from the ISIP = 9896 psi or 14.50 ppg. The early pump-up phase displays a consistent linear trend. A clear slope decrease from 8.5 to 9 bbl records the LOP and the FBP follows immediately after. During the shut-in phase, a sustained, steep pressure decrease is recorded prior to leveling at 2 mins. These four characteristics may indicate a high degree of wellbore stress concentration in an unfractured wellbore.

3.2.1.5 11-7/8” Liner

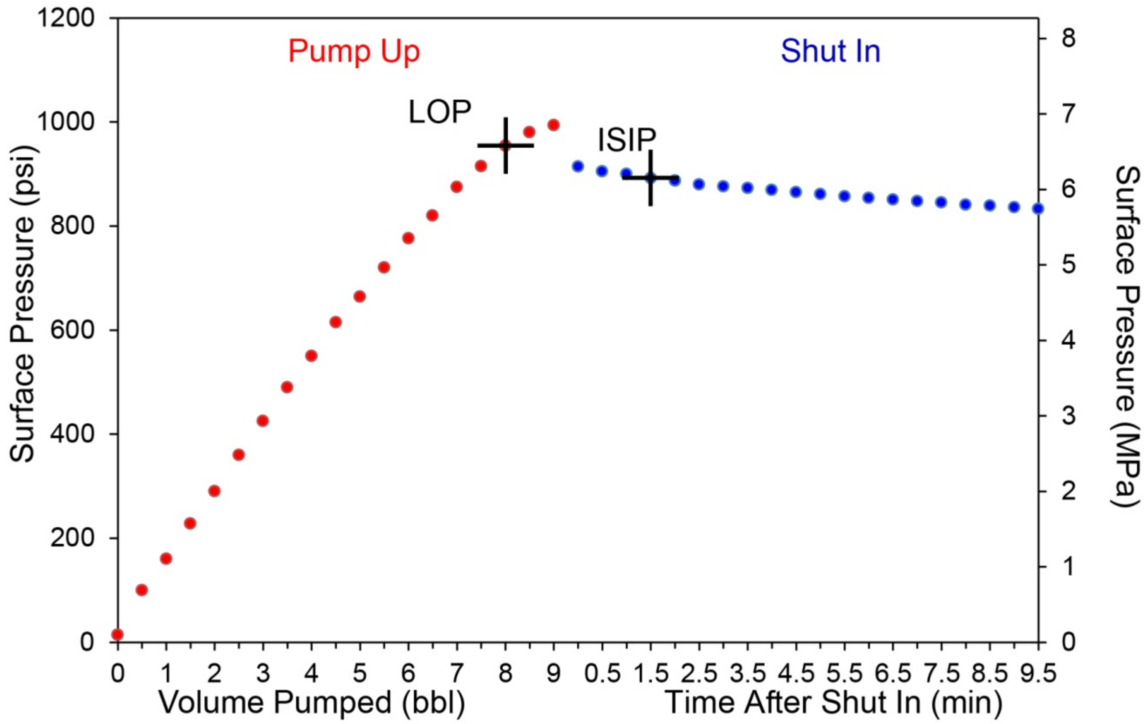

Figure 3.6 11-7/8” Shoe LOT. Test # 1 out of 1; Casing shoe = 15093 ft $z_{df\ DWH}$; ESD of 13.78 ppg or 10804 psi at shoe; LOP = 954 psi; ISIP = 892 psi. Least principal stress calculated from the ISIP = 11696 psi or 14.92 ppg. The pump-up phase is non-linear, so perhaps there is slight permeability in the tested formation or elevated mud system compressibility. I interpret the LOP from the decrease in slope from 8 to 8.5 bbl: dP/dV decreases earlier in the test, but 8 bbl marks the beginning of two consecutive slope decreases. ISIP interpretation is also challenging for this FPIT. Although d^2P/dt^2 is first positive at 0.5 min, I interpret 1.5 min as the ISIP. During shut-in, the slope of the pressure decline decreases from -18 to -10 psi/min to -8 to -6 psi/min at 1.5 min after shut-in. The difference in interpretation is on the order of tens of psi, which is well within the error for these tests.

3.2.1.6 9-7/8" Liner

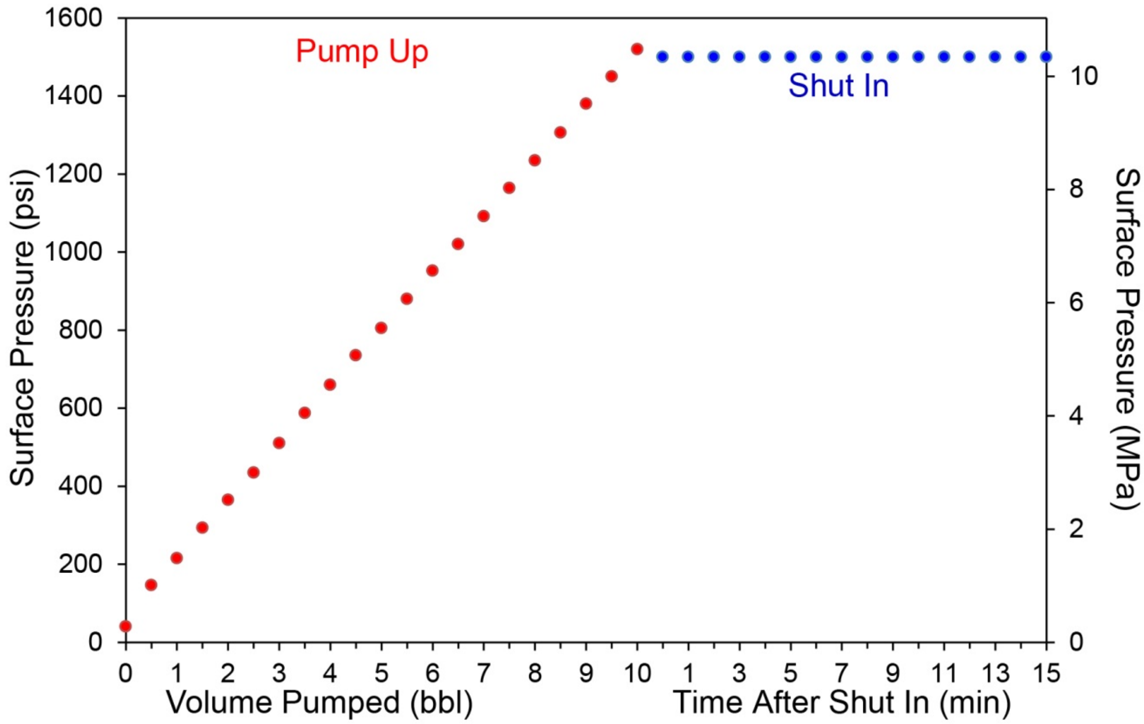

Figure 3.7 9-7/8" Shoe FIT. Test # 1 out of 1; Casing shoe = 17158 ft $z_{df\ DWH}$; ESD of 14.52 ppg or 12942 psi at shoe. Maximum surface pressure without slope break = 1500 psi. Maximum downhole pressure without a slope break = 14462 psi or 16.23 ppg. The maximum pressure from this FIT offers a lower bound for the near-wellbore LOP. This test displays similar response to the 13-5/8" casing LOT: it displays a highly linear pump-up phase and limited late-time shut-in pressure loss. I interpret that near wellbore effects are prohibiting near-wellbore fracture initiation, and that the least principal stress is several hundred psi lower than the maximum as was recorded in the 13-5/8" test.

3.2.2 Mud Loss Events

Lost circulation events incurred while drilling the Macondo well were scrutinized by BP during drilling (e.g. (Lebleu, 2010a, b, c)) and were widely cited during the trial (e.g. (Bartlit et al., 2011; Unknown, 2011a, b)), but they were not compiled into the stress profile of the well. In the following subsections, I paraphrase the circumstances surrounding each lost mud event using end-of-well reports, daily drilling logs, daily geological, daily PPFG reports, and other BP documents released during the trial. Specifically, I note the downhole static and dynamic drilling pressures leading up to, during, and after each lost mud event. Unfortunately, the pressure data available do not have the resolution to distinguish between fracture initiation, breakdown, propagation, or closure pressure, so I bracket the fracture pressure interpretations with upper and lower bounds. I define the upper bound with the ECD when the losses began. Therefore, the upper bound likely exceeds the fracture initiation, breakdown, and propagation pressures, given the magnitude of the losses of each lost circulation event. I estimate the lower bound from the highest static or dynamic pressure at which the well is stable before or after the event. Therefore, the lower bound is less than the fracture initiation pressure.

Constraint of the mud loss location is critical for remediation and stress characterization. In this analysis, the location of the loss zone is inferred from the drilling activity when the loss occurred. Bottom-hole losses can be diagnosed if they occur during drilling or cause MWD torque changes (Growcock 2009). However, it is difficult to pinpoint the location of losses from other operations that increase the static or dynamic borehole pressure. Losses occur in the weakest zone of the exposed formation. The casing shoe is prone to fluid losses, given that it has the least overburden stress (Huffman 2011), and may be weakened by formation pressure integrity test activities. In addition, there is some evidence that sandstones, siltstones, and marls are more loss prone than shales in the Macondo well. It is generally accepted that the in-situ stress of mudstone is higher than that of sandstone and siltstone (Alberty and McLean, 2001; Daines, 1982), although the sandstone fracture pressure can be raised by increasing the near-wellbore stress state (Alberty and McLean, 2001). BP considered the sandstones to be more fracture prone than shales at Macondo (BP, 2010g). Lastly, for events where the loss zones are constrained (Fig. 3.9, 3.10), GR and cuttings suggest that the lithology is sandy/silty/marly. As a result, I assume that losses occur in sandstones, siltstones, and marls when depth constraint is poor.

Table 3.3: Mud loss summary. Equivalent mudweight calculations use $z_{df\ DWH}$ (the true vertical depth measured from the Deepwater Horizon drill floor (75 ft). 18-1/8" x 22" section calculations use the true vertical depth measured from the Marianas drill floor (89 ft). The overburden stress is calculated at the depth of the loss with the model from Appendix A. The pore pressure is interpreted from a nearby kick event (Appendix B), MDT or Geotap measurement, or the pore pressure model (2.4).

Hole Section	Activity	Depth Estimate, zss	Pore Pressure Estimate	Overburden Stress	Fracture Pressure Low Estimate	Fracture Pressure High Estimate	Total Mud Lost
in	-	ft	ppg	ppg	ppg	ppg	bbl
18-1/8" x 22"	Squeeze 22" Shoe						67.5
	Drilling	7975	9.5	11.39	10.15	10.34	22.5
	Running 18"						199
	Cementing 18"						141
16-1/2" x 20"	Drilling	8975	10.79	12.11	11.53	11.72	6804
	Running 16"						2759
	Cementing and Squeezing 16"	8975	10.79	12.11	11.1	11.25	1937
14-3/4" x 16-1/2"	Cementing 13-5/8"						76
12-1/4" x 14-1/2"	Circulating and Cementing 11-7/8"	13914	12.4	14.35	13.7	14.1	307
10-5/8" x 12-1/4"	Running, Circulating, and Cementing 9-7/8"	15160	13.4	15.01	14.33	14.9	342
8-1/2" x 9-7/8"	Drilling	17639	14.15	15.73	14.71	15.04	214
		18089	12.56	15.85	14.53	14.83	3006
8-1/2"	Drilling	18174	12.56	15.87	14.26	14.44	51

3.2.2.1 18-1/8" x 22" Hole Section Lost Mud

I interpret that the fracture gradient is between 10.15 and 10.34 ppg EMW at 7975 ft z_{ss} (Fig. 3.8, Table 3.3). Here, lost circulation occurred as a result of kill operations following a kick taken in the 22" hole section (Appendix B.2.3.2). The borehole was exposed from 22" casing shoe (7862 ft z_{ss}) to the drill bit during the kick (8881 ft z_{ss}). Losses began during kill operations, and continued as the hole was drilled to section TD (9001 ft z_{ss}). The exact loss location is not well constrained because the length of the exposed borehole. I infer losses near the 22" shoe, because it has the least overburden stress, and the FPIT results (3.2.2.1) are similar to the borehole pressures during the loss event.

For the upper bound of the fracture gradient, I use the lowest downhole pressure at which losses occurred. ESD during kill operations were below 10.3 ppg EMW (9.9 ppg SMW) (BP, 2009b) and reached as high as 10.34 ppg (10.1 ppg SMW) while drilling ahead to section TD (Lebleu, 2010c). For the lower bound of the fracture gradient, I use the highest pressure at which the well was stable. ECD of 10.15 ppg EMW was recorded prior to taking the kick (BP, 2009c).

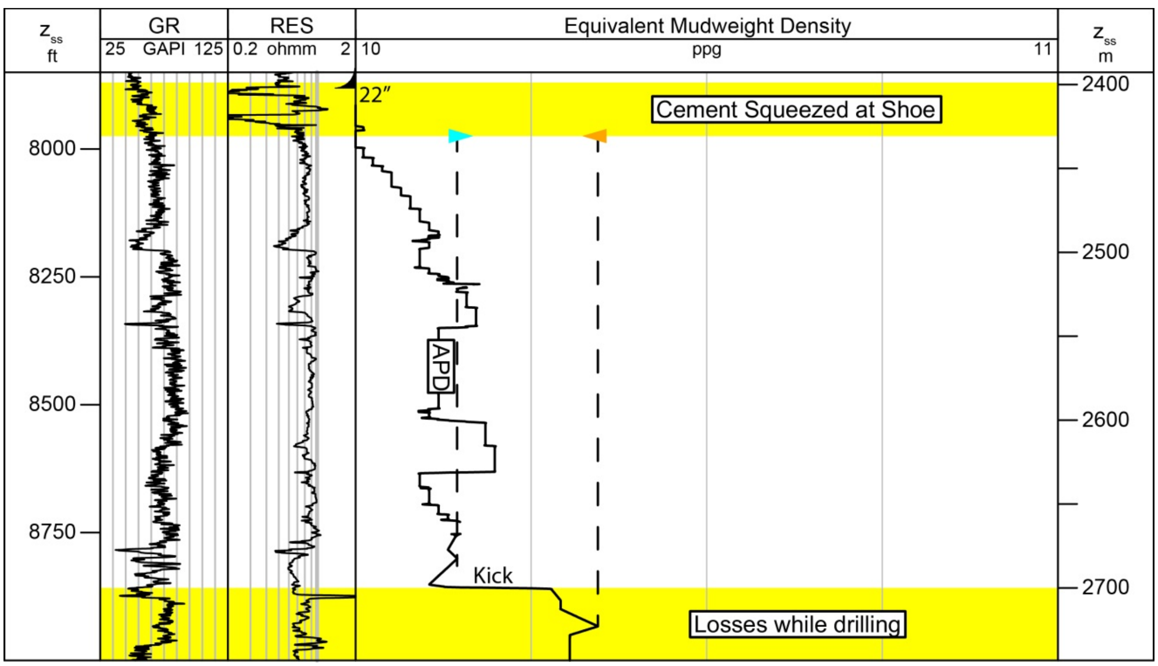

Figure 3.8: Equivalent mudweight vs. depth profile of the mud loss event at 7975 ft z_{ss}. Triangles denote the loss location and fracture gradient range: the lower bound in blue and the upper bound in orange. Dashed black lines project the borehole pressure gradient from the drill bit during the loss to the interpreted loss location. The upper yellow box highlights the 22” shoe depths reinforced by cement squeeze operations; I interpret that the losses likely occurred just below the squeezed formation. The lower yellow box illustrates the interval that was drilled while losses were occurring.

3.2.2.2 16-1/2" x 20" Hole Section Lost Mud

I interpret that the fracture gradient is between 11.53 and 11.72 ppg EMW at 8975 ft z_{ss} (Fig. 3.9, Table 3.3). Losses occurred when the drill bit was picked up off of the bottom hole (12269 ft z_{ss}) to circulate, clean the hole, and lower the ECD. The formation was exposed up to the 18” casing shoe (8894 ft z_{ss}), and the loss location is well constrained by resistivity log runs before and after the loss event (Fig. 3.9). The upper fracture gradient bound is ECD when the losses began (11.63-11.72-ppg) (Halliburton, 2010b). The lower bound of the fracture gradient is interpreted from the ESD of 11.53 ppg during a static flow check at 12116 ft z_{ss} prior to the loss event (Halliburton, 2010b).

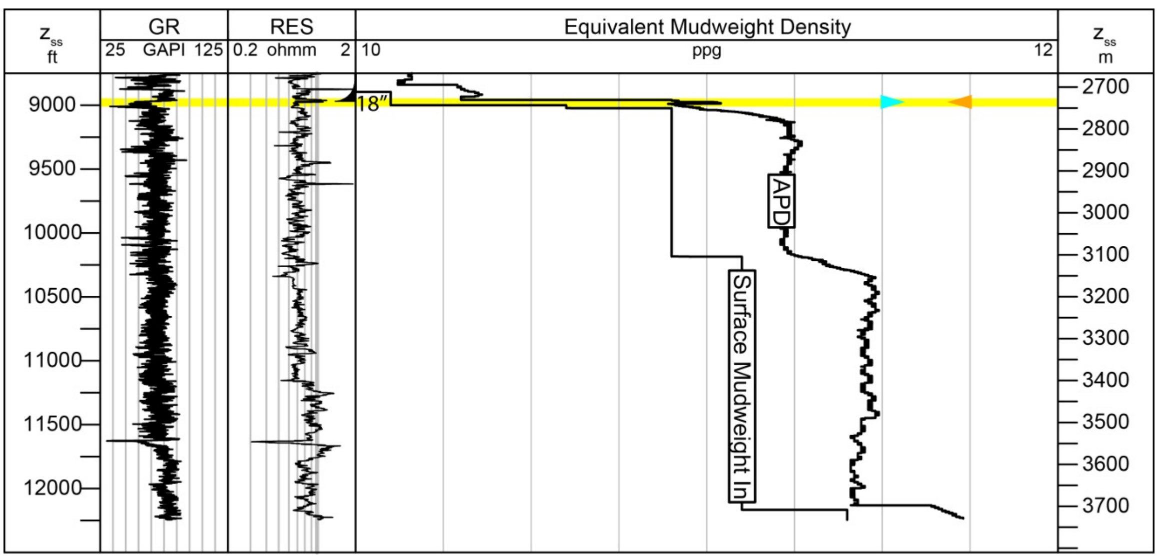

Figure 3.9: Equivalent mudweight vs. depth profile of the mud loss event at 8975 ft z_{ss}. Triangles denote the loss location and fracture gradient range: the lower bound in blue and the upper bound in orange. The yellow box highlights the location of the loss interval (Fig. 3.10)

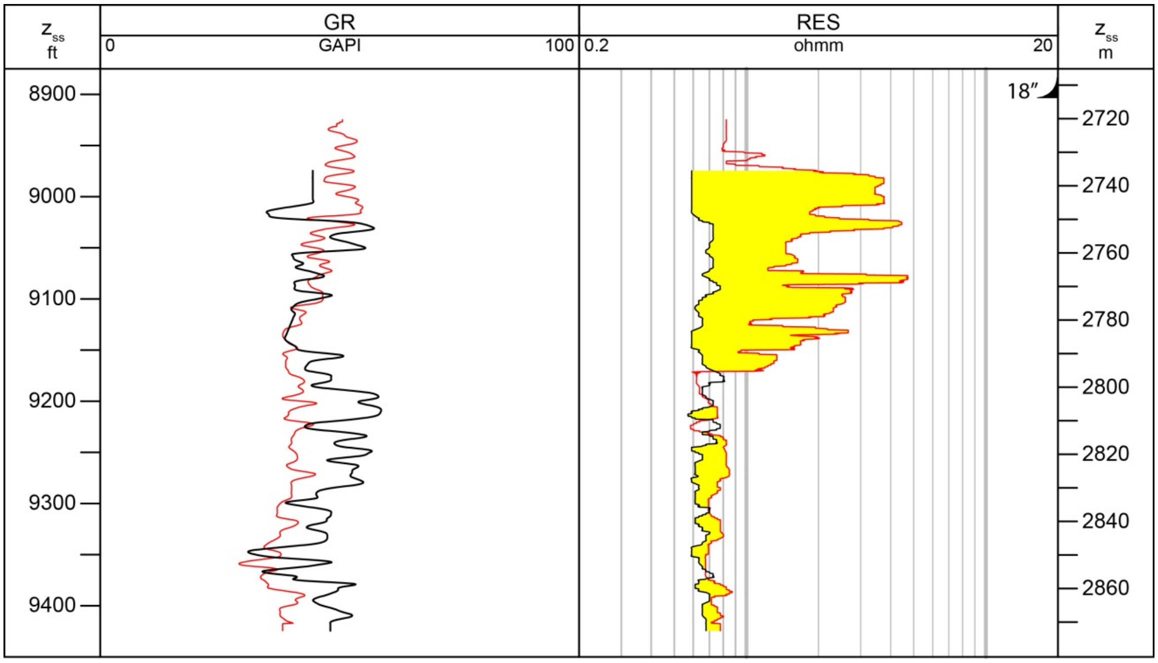

Figure 3.10: Wipe vs. drill log runs of the 8975 ft z_{ss} mud loss event. Black lines denote the LWD log measurements during drilling. Red lines show the measurements made after the loss events. The dramatic increase in resistivity reflects the presence of non-conductive oil-based mud inside of fractures in the formation.

Subsequent lost returns into this zone may indicate weakening of the formation. I interpret that the fracture gradient decreased to between 11.1 and 11.25 ppg EMW at 8975 ft z_{ss} (Fig. 3.11, Table 3.3). After regaining control of the well, BP cemented the 16” casing in place to 11510 ft z_{ss}. Upon drilling through cement at the 16” shoe, mud losses resumed with 11.5 ppg SMW. The cement job appears to have failed to isolate the shallower formation and thus there was connectivity to the from the 16” shoe to the existing fractures in the 18” shoe. Following well control operations, the well was later static with 11.1 ppg SMW, but losses continued with 11.25 ppg SMW. These serve as my interpretations of the fracture gradient bounds.

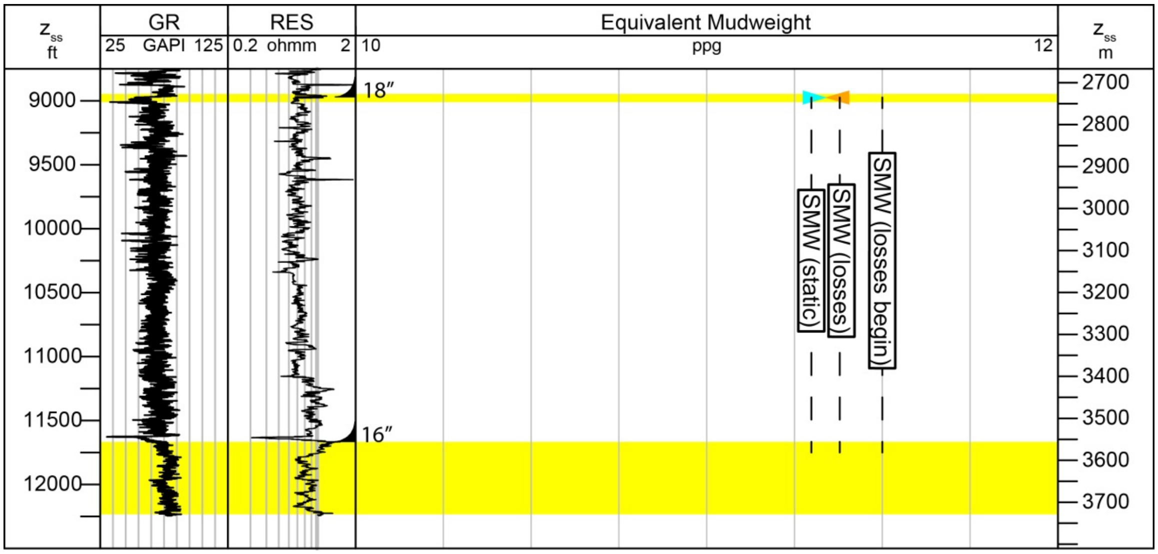

Figure 3.11: Equivalent mud weight vs. depth profile of the mud loss event at 8975 ft z_{ss}. Triangles denote the loss location and fracture gradient range: the lower bound in blue and the upper bound in orange. The upper yellow rectangle highlights the location of the loss interval (Fig. 3.10). The lower yellow rectangle shows the cemented borehole below the 16" casing. Cementation of the 16" liner in place failed to isolate the formation up to the 18" shoe, the location of the losses. Dashed black lines project the borehole pressure gradient from the 16" shoe to the 18" shoe loss location.

3.2.2.3 12-1/4" x 14-1/2" Hole Section Lost Mud

I interpret that the fracture gradient is between 13.7 and 14.1 ppg EMW at 13914 ft z_{ss} (Fig. 3.12, Table 3.3). Losses occurred after the 11-7/8" casing was lowered into place while circulating and cementing. Prior to lowering the casing, the hole was circulated and conditioned with 13.7 ppg ECD (13.3 ppg SMW), and the mudweight was raised to 13.4 ppg (13.64 ppg ESD) without losses (Halliburton, 2010b). I interpret 13.7 ppg as the lower bound of the fracture gradient. The fracture gradient upper bound is poorly constrained because the casing summary report was not released, and therefore the dynamic pressure data is unavailable. The loss location is also poorly constrained. Leak off tests at the 13-5/8” and 11-7/8” inch shoes (Fig. 3.12, brown squares) suggest a fracture gradient of at least 14.8 ppg at the top and bottom of the hole section. I assume that the loss occurred into the shallowest exposed sand at 13275 ft z_{ss}.

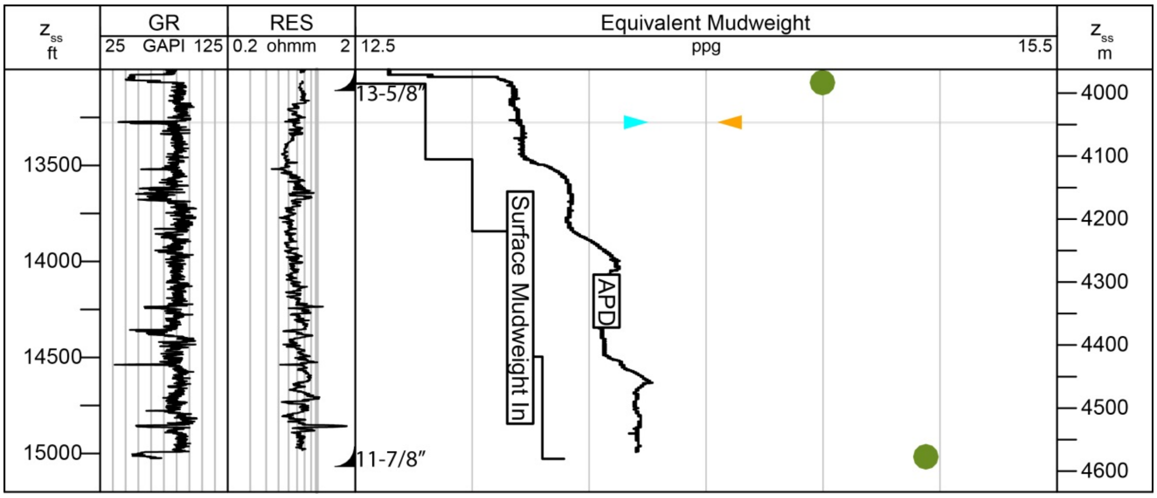

Figure 3.12: Equivalent mudweight vs. depth profile of the mud loss event at 13914 ft z_{ss}. Triangles denote the loss location and fracture gradient range: the lower bound in blue and the upper bound in orange. The green circles record the least principal stresses interpreted from the FPIT tests at the 13-5/8” and 11-7/8” shoes.

3.2.2.4 10-5/8" x 12-1/4" Hole Section Lost Mud

I interpret that the fracture gradient is between 14.33 and 14.9 and ppg EMW at 15160 ft z_{ss} (Fig. 3.13, Table 3.3). Losses occurred while running the liner, circulating, and cementing the 9-7/8” liner in place. Prior to lowering the casing, the hole was circulated and conditioned with 14.33 ppg ESD (14.1 ppg SMW) without losses (Halliburton, 2010b). I interpret 14.33 ppg as the lower bound of the fracture gradient. The fracture gradient upper bound is poorly constrained because the casing summary report was not released, and therefore the dynamic pressure data is unavailable. The loss location is also poorly constrained. Formation pressure integrity tests at the 11-7/8” inch and 9-7/8” shoes (Fig. 3.13, brown squares) suggest a fracture gradient of at least 15 ppg at the top and bottom of the hole section. I assume that the loss occurred into the shallowest exposed sand at 15160 ft z_{SS}.

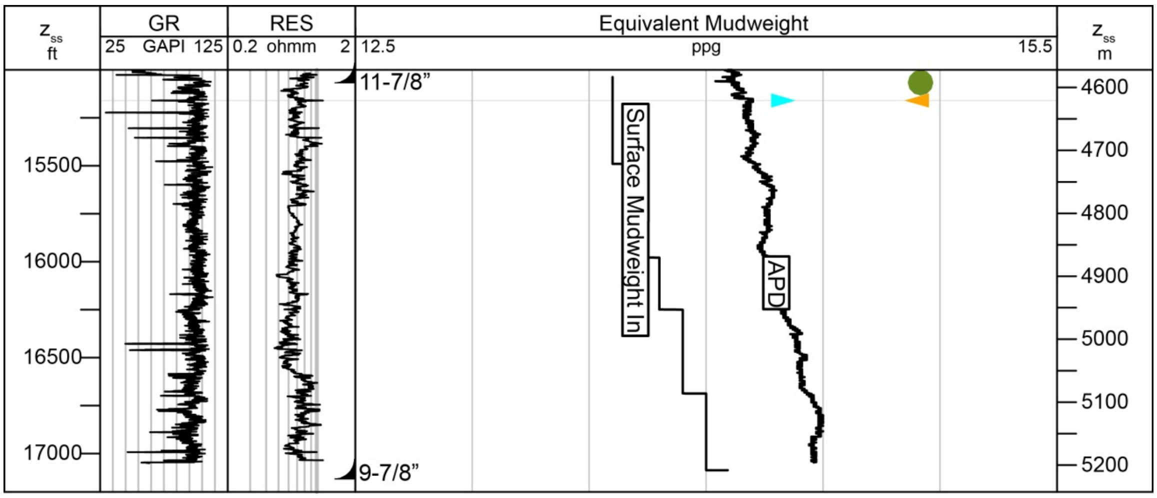

Figure 3.13: Equivalent mudweight vs. depth profile of the mud loss event at 15160 ft z_{SS}. Triangles denote the loss location and fracture gradient range: the lower bound in blue and the upper bound in orange. The green circle records the least principal stress interpreted from the FPIT test at the 11-7/8” shoe.

3.2.2.5 8-1/2" x 9-7/8" and 8-1/2" Hole Sections Lost Mud

BP lost returns occurred on three separate occasions while drilling the final hole sections of the Macondo well Fig. 3.14 (a, b, c). I interpret that the fracture gradient is between 14.71 and 15.04 ppg EMW at 17639 ft z_{SS} (Fig. 3.14 (a), Table 3.3). Losses began while drilling through the M56A sand at 17639 ft z_{SS}, and I interpret the 15.04 ppg ECD during drilling (BP, 2010a) to be the upper bound of the fracture gradient. I interpret the fracture gradient lower bound to be 14.71 ppg, which is the ESD at which the well flowed back (BP, 2010a). The 16 ppg FIT at the 9-7/8” shoe and the fact that losses occurred during drilling suggest that losses occurred at the drill bit and not the shoe.

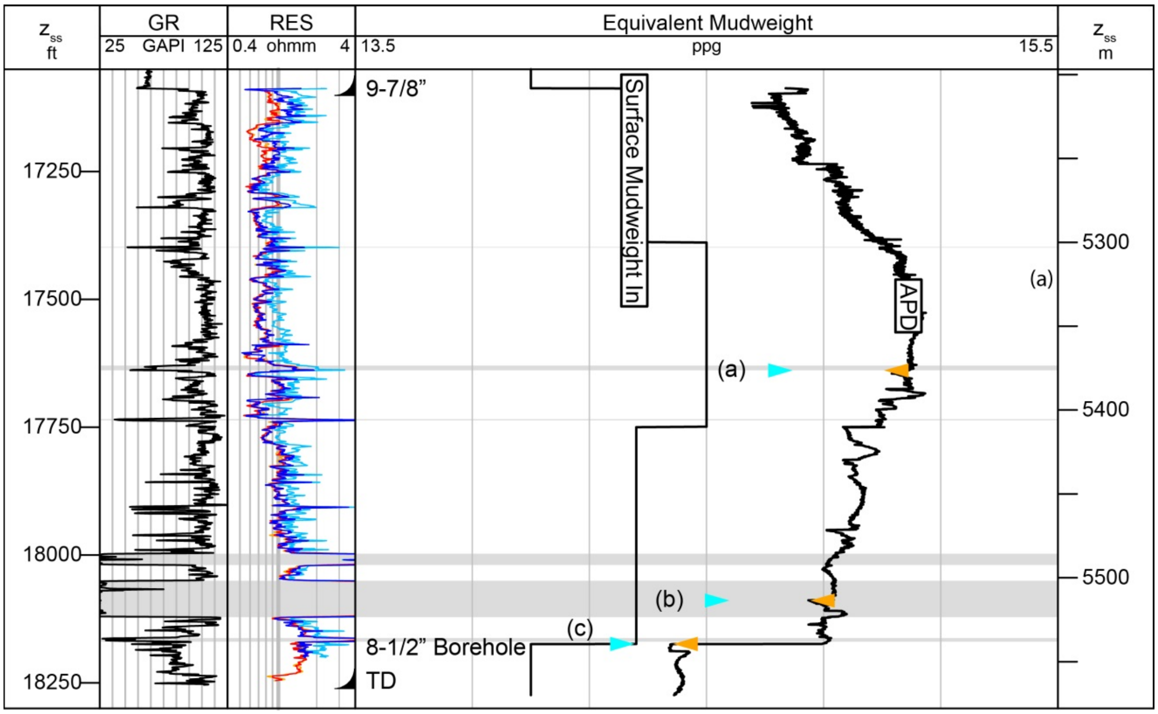

Figure 3.14: Equivalent mudweight vs. depth profile for the bottom hole mud loss events. Triangles denote the loss locations and fracture gradient ranges: the lower bounds in blue and the upper bounds in orange. The three separate lost circulation occurred across the 8-1/2" x 9-7/8" and 8-1/2" hole sections and are note with a, b, and c. Colors differentiate four nearly overlapping resistivity curves: blue – wireline deep, light blue – wireline shallow, red – LWD deep, orange – LWD shallow.

I interpret that the fracture gradient is between 14.53 and 14.83 ppg EMW at 18089 ft z_{ss} (Fig. 3.14 (b), Table 3.3). Mud losses began while circulating at 18,174 ft z_{ss} with an ECD of 14.83 ppg, and I interpret this to be the upper bound of the fracture gradient in the M56 sandstone. The lower bound is interpreted from the 14.53 ppg ESD prior to taking losses (BP, 2010b). The 14.7+ ppg fracture gradient observed shallower in the hole section suggests that this loss event occurred near the drill bit. In addition, the resistivity logs do not indicate fracturing of the mudstone: There are minimal differences between the LWD and wireline resistivity runs, and little separation between shallow and deep resistivity measurements.

This loss event appears to have reduced the fracture gradient in the M56 sand. During remediation efforts, the well was stabilized at 13.9 ppg EMW (Halliburton, 2010b), and a subsequent loss event occurred while drilling the final 100 ft of the well. I interpret that the fracture gradient was reduced to between 14.26 and 14.44 ppg EMW in the M56 sandstone (Fig. 3.14 (c), Table 3.3). These bounds are interpreted from the ESD and ECD during drilling (BP, 2010c). Because the interval was subjected to repeated fracture, the reduced fracture gradient perhaps gives an indication of the least principal stress.

3.2.3 Least Principal Stress Model

3.2.3.1 Effective Stress Ratio

In order to estimate the least principal stress continuously with depth at the Macondo well, I use an empirically calibrated effective stress ratio, *K*, after (Hubbert and Willis, 1972; Matthews and Kelly, 1967; Pilkington, 1978) where:

$$\mathrm{K} = \frac{\sigma_h - u}{\sigma_v - u} \qquad \text{Eq. 3.2}$$

First, I calculate *K* where least principal stress, σ_h, vertical stress, σ_v, and pore pressure, u, are known. In other sections, pore pressure (Appendix B, Chapter 2.4.1) and overburden stress (Appendix A) are modeled continuously in the wellbore. The least principal stress is constrained at five casing shoes based on instantaneous shut-in pressures during the FPIT (3.2.1). At these five casing-shoe locations, the effective stress ratio varies between 0.51 and 1.13 (Fig 3.15, Table 3.3).

The effective stress ratios for the 13-5/8” and 11-7/8” casing shoe FPITs are close to or above 1; this falsely suggests that the minimum horizontal stress is close to or greater than the overburden stress. One possible explanation is that the ISIP interpretations did not completely eliminate near-wellbore effects. Neither test recorded stable fracture propagation away from the wellbore, so it is reasonable that stress concentration is driving the ISIP interpretations above the far-field least principal stress. Alternatively, the overburden model may underestimate the vertical stress. In fact, the model from Appendix A is slightly lower than BP’s post-drill estimate (Fig. A.6). The difference between the vertical stress, least principal stress, and pore pressure is roughly several hundred psi (Table 3.4), so a few-percentage-point inaccuracy with respect to total stress could significantly change K. Because I cannot completely eliminate near-wellbore effects from the model calibration, the model results may skew slightly greater than the true far-field least principal stress.

Table 3.4: Effective stress ratio calculation for each ISIP. The average effective stress ratio from these five ISIP interpretations is 0.78, and it is used to calibrate the least principal stress model.

FPIT Casing Diameter	Vertical Stress	Least Principal Stress (ISIP)	Pore Pressure	Effective Stress Ratio
in	**psi**	**psi**	**psi**	**-**
22"	4668	4245	3800	0.51
18"	5620	5455	5027	0.72
16"	8157	7633	6921	0.58
13-5/8"	9728	9896	8461	1.13
11-7/8"	11728	11696	10506	0.97

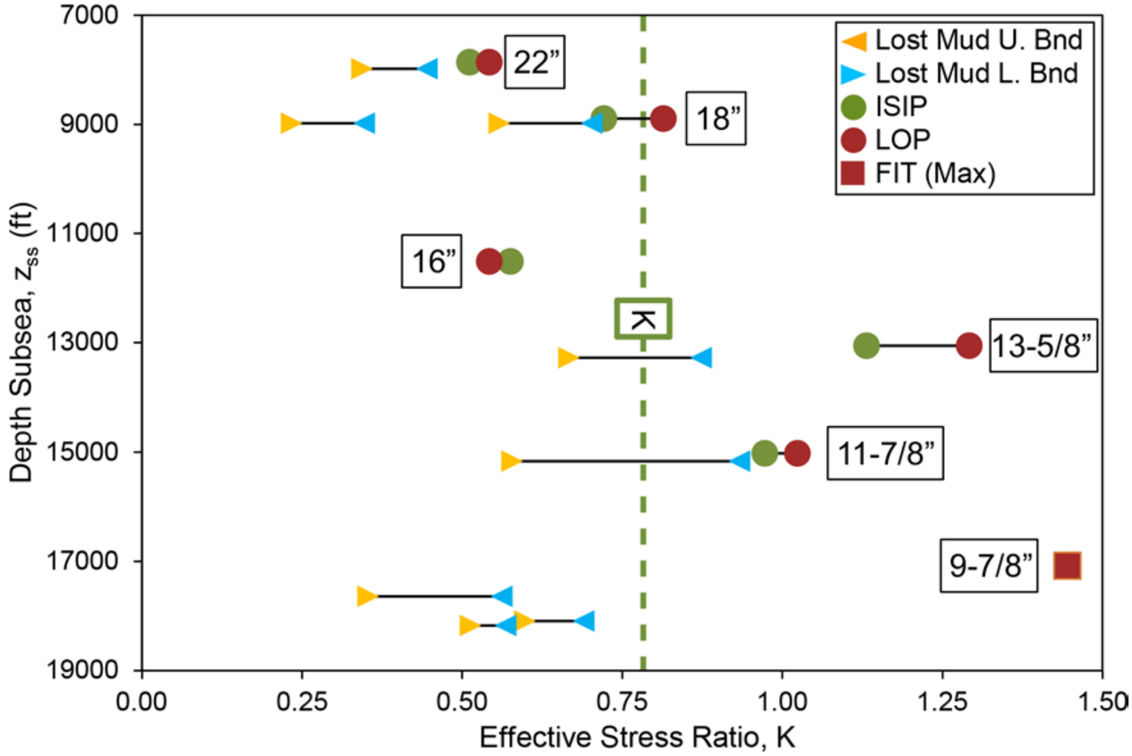

Figure 3.15: K vs. depth for the Macondo FPITs and lost mud events. For each FPIT, the effective stress ratio calculated from the ISIP (green circle) and LOP (brown circle) are connected with black line and labeled with the corresponding casing diameter. The vertical green dashed line records the average effective stress ratio for the five ISIP interpretations (green circles). For each mud loss event, two effective stress ratios are calculated: the lower bound (orange triangle) is connected to the upper bound (blue triangle) with a black line.

Next, I calibrate a single K to describe stress behavior in the well. I calculate the mean (Fig. 3.15, green line) of the five ISIP-derived effective stress ratios (Fig. 3.15, green circles). The resulting effective stress ratio is 0.78. With K calibrated to the Macondo well, Eq. 3.2 is rearranged to solve for σ_h.

$$\sigma_h = K(\sigma_v - u) + u \qquad \text{Eq. 3.3}$$

The overburden model, pore pressure prediction, and $K = 0.78$ are entered in Eq. 3.3 to estimate a continuous least principal stress curve. Implicit in this technique is the assumption that the stress ratio is constant with depth.

3.3 Results

3.3.1 Model Results

Both the mud-loss pressures (Figs. 3.16, 3.17, triangles) and the least principal stress model (Figs. 3.16, 3.17, brown line) trend parallel to the overburden stress before decreasing across the reservoir interval. Because the least principal stress model is derived in part from the pore pressure prediction (Figs. 3.16, 3.17, blue line), the model depth range is limited to where sonic logs were acquired.

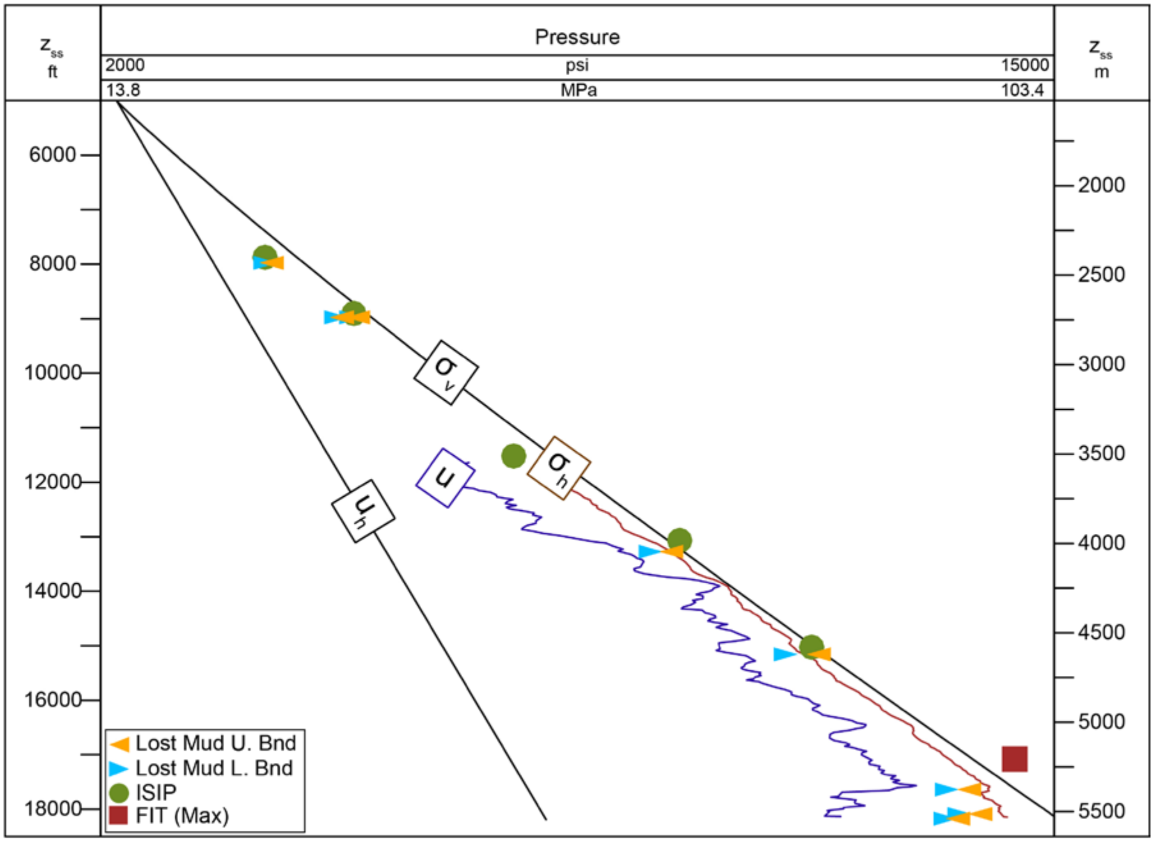

Figure 3.16: Pressure and stress vs. depth at the Macondo well. The hydrostatic pressure, u_h, assumes a constant fluid density of 1.024 g/cm^3 (seawater) from the sea surface. The overburden stress, σ_v (black line), and pore pressure, u (blue line) are modeled in Appendix A and section 2.4, respectively. The least principal stress, σ_h (brown line), assumes a K value of 0.78. Stress interpretations are shown with symbols (triangles, squares, circles). Triangles denote the location and fracture gradient range for each mud loss event: the lower bound in blue and the upper bound in orange. Green circles denote the downhole ISIP pressures. The brown square illustrates the maximum downhole pressure from the anomalous above-overburden 9-7/8" shoe FIT.

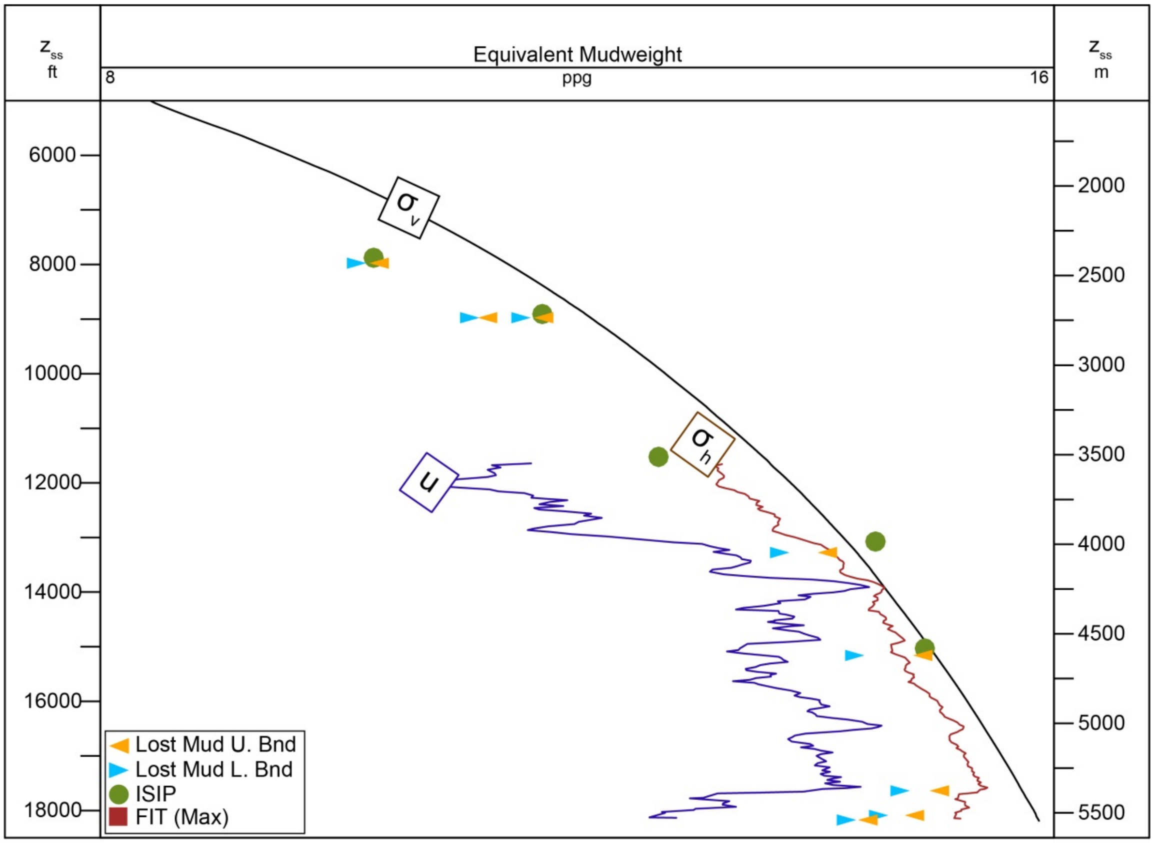

Figure 3.17: Pressure and stress equivalent mudweight vs. depth at the Macondo well. The plot is equivalent to Fig. 3.16; pressures and stresses have been converted to EMW.

At approximately 14000 ft z_{ss}, there is an anomalous increase in the pore pressure and least principal stress. The sonic velocities here decrease, suggesting decreased compaction and effective stress and increased total least principal stress. Near this depth, the first above-overburden FPIT result occurs; this may indicate increased stress, although the mechanism is not well understood. The model predicts least principal stresses that fall within the upper and lower bounds of the lost circulation pressures (Fig. 3.16, 3.17, orange and blue triangles) at 13914 and 15160 ft z_{ss}. However, σ_h exceeds the lost circulation pressures within the reservoir interval. A K value between 0.5 and 0.65 would better capture the reservoir-interval lost circulation pressures. The model also overestimates the effective stress ratios interpreted for the shallow loss events (Fig. 3.15). Although the stress model does not extend above 11000 ft z_{ss}, the K values calculated for the shallow mud loss events vary between 0.23 and 0.7, below K = 0.78 used in the model.

Perhaps the lithology is affecting the stress response. Casing tends to be set in mudstone, so most of the FPITs record the mudstone fracture and stress properties. As a result, K is calibrated to mudstone, so the least principal stress model is representative of the mudstone stress state. The reservoir interval, however, is sand prone, and in 3.2.2.5 I provide evidence that losses occurred into the sandstone. It is therefore reasonable that the least principal stress estimate overpredicts the sandstone least principal stress. The 22” FPIT may have had exposed sands in the casing shoe (BP, 2009a), which explains why K is so far below the other ISIP effective stress ratios.

3.3.2 Comparison to Existing Analysis

As part of their post-drill analysis, BP updated their pre-drill pore pressure and fracture gradient models for the Macondo well to incorporate the data collected during drilling (BP, 2010g). Fig. 3.18 compares BP’s post-drill models (green) to those models outlined in chapters 2 and 3. Although BP’s pore pressure and fracture gradient prediction methodology is proprietary, the fracture gradient prediction appears to use a constant effective stress ratio for sand and shale. BP’s model uses a K of ~0.76 for shale, which is virtually identical to the effective stress calibrated from ISIP interpretations. The K for sand used in the BP model is ~0.49. The BP model confines reductions in pore pressure and fracture gradient to the M56 sandstones, whereas my models suggest that the pressure and stress regression presents in both the sandstones and mudstones (to a lesser degree) across the interval.

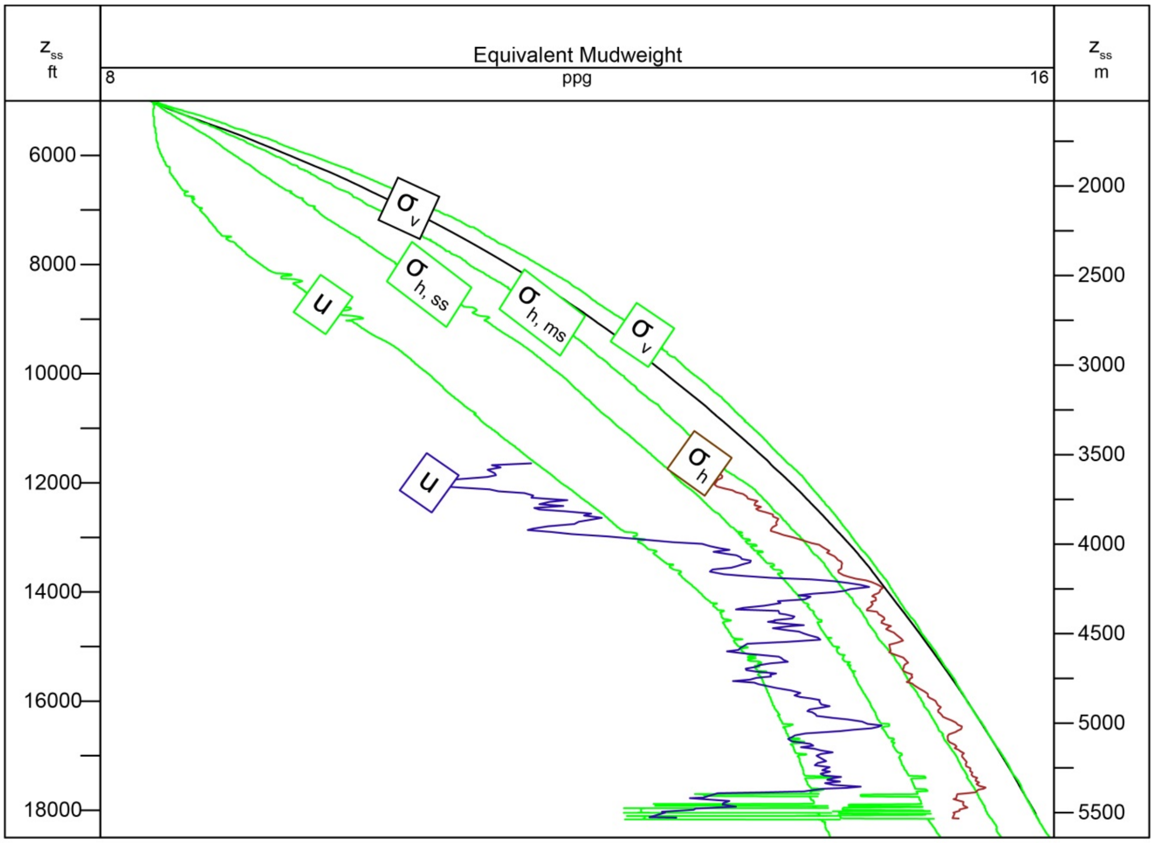

Figure 3.18: Pressure and stress equivalent mudweight vs. depth at the Macondo well. The overburden (black line, Appendix A), least principal stress (brown line, chapter 3), and pore pressure (blue line, section 2.4) models from this study are compared to those calculated by BP (green) in their post-drill analysis (BP, 2010g). BP's fracture gradient models appear to use effective stress ratios of ~0.49 and ~0.76 for sandstone, $\sigma_{h,\,ss}$, and mudstone, $\sigma_{h,\,ms}$, respectively.

3.3.3 Conclusions

I have shown that the pore pressure regression at the Macondo well contributed to the reduction in the fracture gradient across the reservoir interval. In Chapter 2, I demonstrate that pressure measurements record a sharp decrease in the pore pressure as the reservoir interval is approached. Through FPIT and mud loss event interpretation, I demonstrate that the fracture gradient also decreases sharply as the reservoir is approached. The velocity-based least principal stress model establishes the link between the pore pressure and least principal stress regressions. I interpret the sharp increase in mudstone velocity across the reservoir interval to indicate increased effective stress but below-trend total least principal stress. In addition to the below-trend total stress, lithology may have contributed to the decreased fracture gradient. Finally, it is possible that repeated lost circulation in the reservoir interval decreased the fracturing gradient.

Appendix A: Overburden Stress Model

A.1 Introduction

An accurate total vertical stress model provides the underpinnings for pressure and stress analysis. This appendix presents the methods and assumptions of the vertical stress model for the Macondo well. I aggregate and filter density data from the Macondo well and analog wells to create a continuous density profile with depth below seafloor. At the Macondo well, density logs were acquired from 17088 to 18190 ft z_{ss}. Density data were not acquired from 4992 to 17087 ft z_{ss}, so I infer the density in these intervals in the following manner. I aggregate the density logs from MC 252-1 (Texaco), MC 296-1, and MC 897-1 (IODP U1324) (A.2.1). I calculate density from the logging-while-drilling compressional velocity log at the Macondo well using a calibrated empirical transform (A.2.2). I then filter the data (A.2.3) and interpolate across gaps in the data (A.2.4) to create a continuous density curve with depth.

Next, I integrate the density profile with depth to calculate overburden stress at the Macondo well. I equate the overburden stress to the vertical stress by assuming that one of the principal stresses is oriented vertically. Two common models that result in an overburden stress that is principal and greatest is the uniaxial strain model (e.g. (Hottman and Johnson, 1965; Hubbert and Rubey, 1959)) and the Anderson (1951) fault model for extension. Either of these models reasonably characterizes stress in the deepwater Gulf of Mexico. I also apply the Macondo overburden model to other wells in the region (e.g. Fig. 2.3, MC 562-1) by changing the water column height component of the vertical stress.

A.2 METHODS

A.2.1 Analog Wells

No single well in the adjacent eight lease blocks contains density logs that span the seafloor to the total depth of the Macondo well, so the model synthesizes multiple wells into a single density profile. I aggregate the density logs from MC 252-1 (Texaco), MC 296-1, and MC 897-1 (IODP U1324 from Long et al. (2011)) using the seafloor as a common datum (Fig. A.1).

Density logs in MC 252-1 (Texaco) span 3509 to 7509 ft z_{sf} (below seafloor). At MC 296-1, density logs span 7509 to 8791 ft z_{sf}. Due to their proximity, both wells provide reasonable estimates for the density profile at the Macondo well. Both wells are within three miles of the Macondo well and therefore likely experienced similar depositional processes. Salt canopies dramatically change the density profile of wells in Deepwater Gulf of Mexico; Macondo, MC 252-1 (Texaco), and MC 296-1 did not encounter salt.

I incorporate density measurements at MC 879-1 to estimate the near seafloor density profile from 0 to 1986 ft z_{sf}. MC 879-1 serves as a reasonable analog for shallow density at Macondo for several reasons. IODP Expedition 308 Site U1324, located 50 miles from the Macondo well in Mississippi Canyon block 897. MC 897-1 has a water depth of 3467 ft, which is ~1500 ft shallower than any of the other analog wells. Given its similar proximity to the Mississippi River Delta, I assume MC 897-1 experienced similar sedimentation across the sampled depths (Pleistocene-Holocene sediments). At 897-1, densities are recorded as moisture and density (MAD) measurements (Blum, 1997), whereas nuclear logs measure density in the other analog wells. MC 897-1 is also relevant as an analog because, like the Macondo well, it records overpressures at shallow depths. Long et al. (2011) observes near surface overpressures as shallow as ~330 ft below seafloor at MC 897-1. The first indicator of overpressure at the Macondo well could be as shallow as 1200 ft z_{sf}, but overpressure likely begins even shallower. Overpressure reduces effective stress, which increases porosity and thus reduces density and vertical stress.

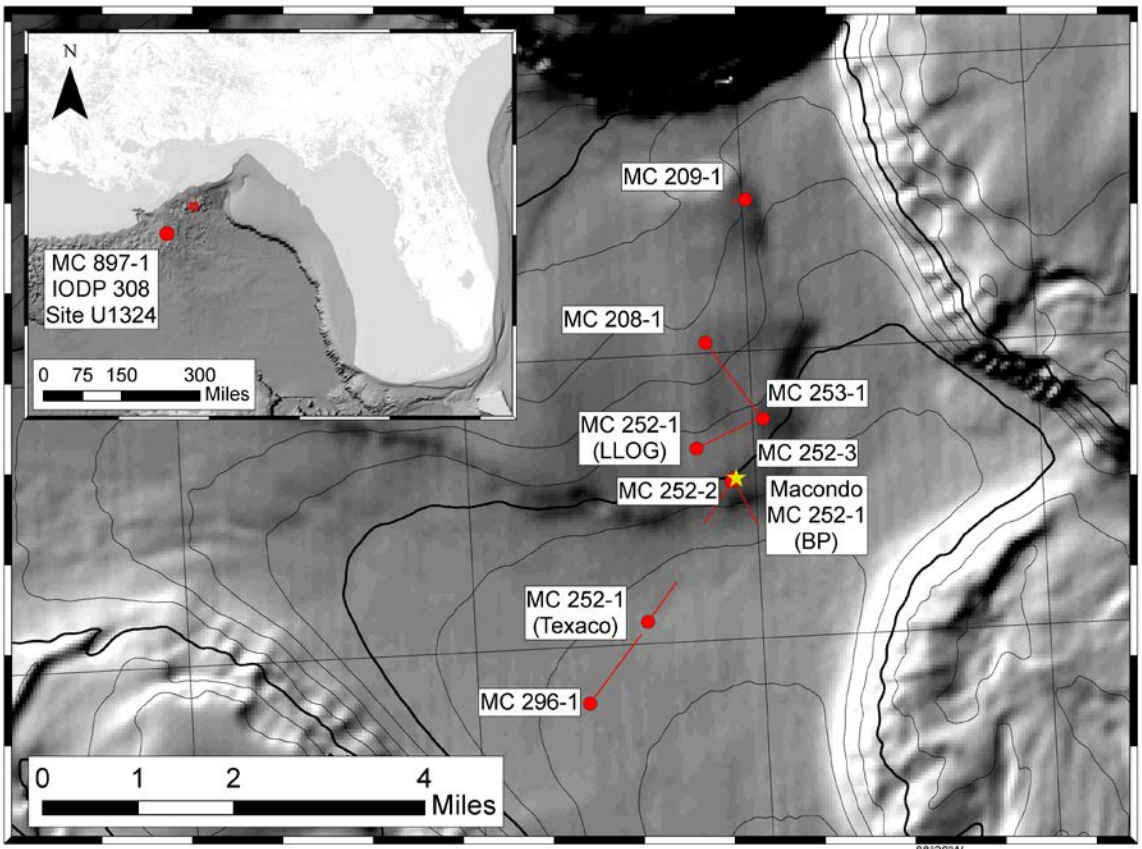

Figure A.1: Bathymetry map of the region surrounding the Macondo well, Mississippi Canyon, Gulf of Mexico. Symbols record bottom-hole locations and red lines approximate well trajectories. A star denotes the Macondo well.

A.2.2 Sonic to Density Transform

I also use compressional velocity recorded at the Macondo well to estimate density. Although density logs were acquired only along the target hydrocarbon-bearing interval at the Macondo well, compressional velocity log data spans a longer section of the well from 6600 ft to 13000 ft z_{sf}. Compressional velocity is in part a function of density, and can be related through an empirical relationship using lithological constraints. Gardner et al. (1974) establishes a well-known, empirically-based, power-law, velocity-to-density transform:

$$\rho = A\, v^{B} \qquad \text{(Eq. A.1)}$$

where for, ρ, is density (g/cm^3), v is velocity (ft/s), and A and B are empirically derived unit dependent constants.

The sonic and density wireline logs in the Macondo well overlap across ~1000 ft near the pay interval (Fig. A.2), so I locally calibrate the equation, controlling for lithology. Mudstone is the dominant the lithology from 8750-12000 ft z_{sf}, so I filtered the overlapping data to exclude gamma ray values below 70 GAPI and bulk densities below 2.35 g/cm^3 (Fig. A.2, black circles). I use ordinary least squares regression to constrain the A and B parameters for the mudstones in the Macondo well. The calibration yields A = 0.6639 and B = 0.1418 (ft/s and g/cm^3). I then use this calibrated relationship to calculate density from velocity from 8750 ft to 12000 ft z_{sf} (Fig. A.3, pink dots).

I calibrated Eq. A.1 for the Macondo well because the parameters from the paper, A = 0.25 and B = 0.23, describe the velocity vs. density relationship for a wide range of depths, ages, and regions for combined sandstone and mudstone lithologies. The parameters from Gardner et al. (1974) (Fig. A.2, blue line) under-predict density across the velocities measured.

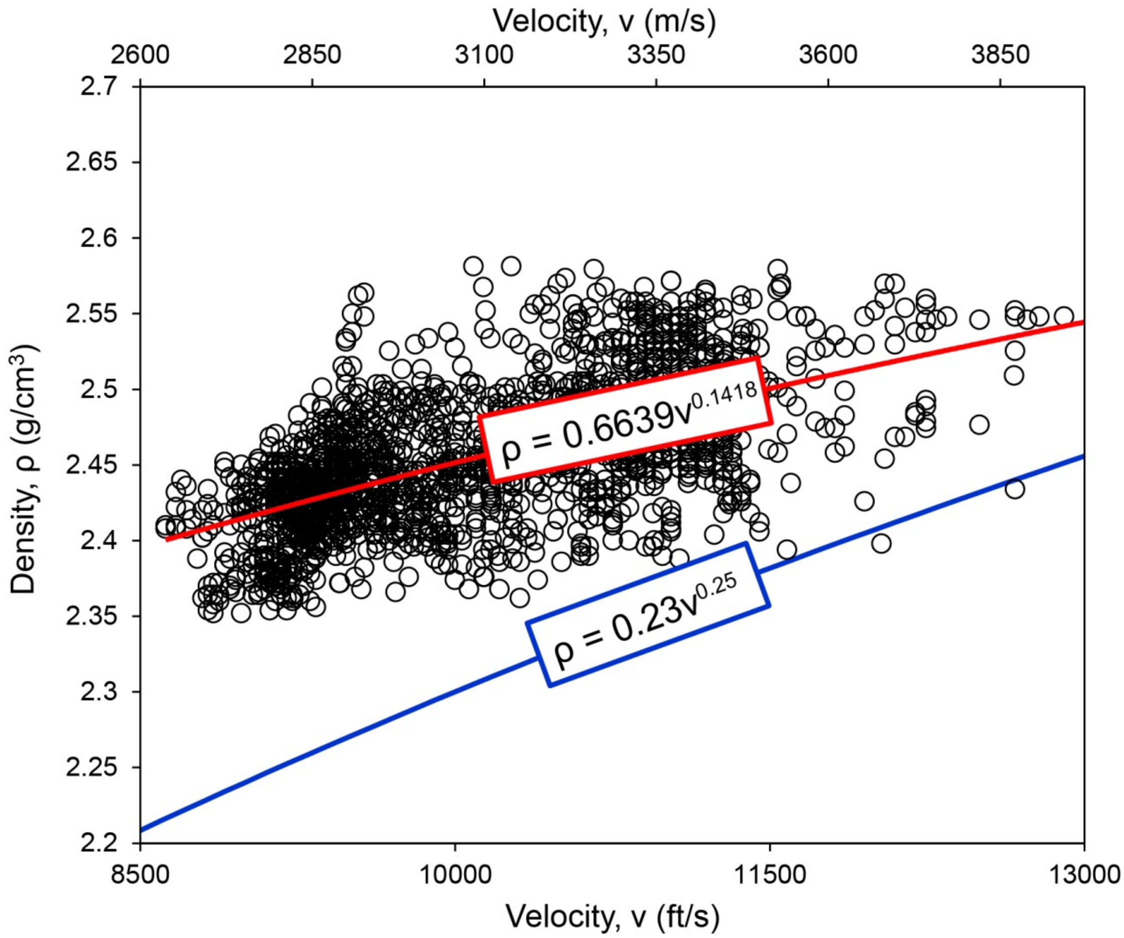

Figure A.2: Velocity vs. density at the Macondo well.Black circles record velocity vs. density in mudstones between ~17,100 and 18,100 ft z_{ss} from the overlapping wireline log. The red line records the empirical power-law relationship calibrated for the mudstones at the Macondo well. The blue line illustrates the calibration from Gardner et al. (1974). Parameters are unit dependent (ft/s and g/cm^3).

A.2.3 Density Synthesis and Filters

Unfiltered density data from MC 897-1, MC 252-1 (Texaco), MC 296-1, and Macondo along with sonic density from Macondo are displayed on Fig. A.3. I filter the data in the following manner. For the MC 897-1 data per (Long, 2007), I calculate a matrix density for each MAD measurement using Eq. A.3, which is possible because porosity and bulk density are measured independently. I then eliminate data points with unrealistic matrix densities (<2.6 g/cm^3) and (>2.8 g/cm^3) because they likely represent erroneous MAD measurements. Each eliminated measurement is replaced with the next shallowest valid measurement. Above 5000 ft z_{sf} I removed all data with a bulk density below 2.0 g/cm^3, and below 5000 ft z_{sf} I removed all data with a bulk density below 2.15 g/cm^3. I filter the density data to remove erroneous measurements (e.g. poor pad contact) and highly porous sands in the analog wells that do not represent the mudstone-dominated lithology penetrated by the Macondo well. Sandy, highly porous, hydrocarbon-bearing intervals tend to have lower densities than the surrounding mudstone.

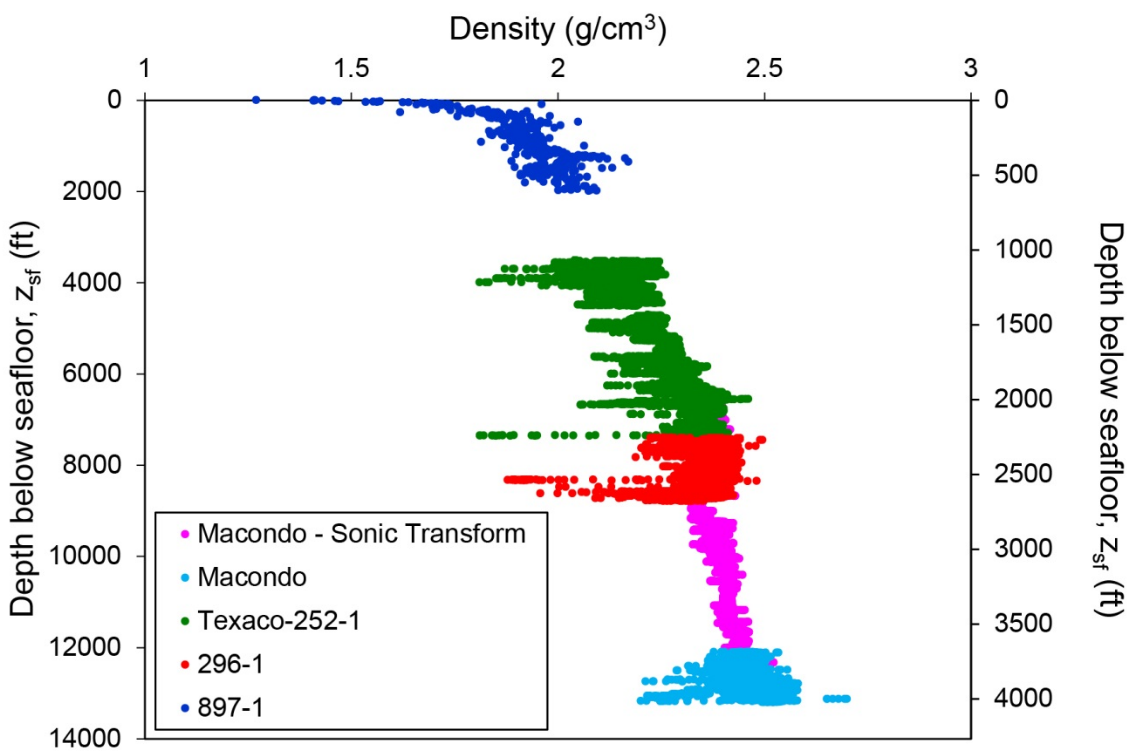

Figure A.3: Bulk density vs. depth below seafloor for the Macondo well and three analog wells. MC 897-1 measurements (blue) are recorded using MAD measurements. MC 296-1 (red), MC 252-1 (Texaco) (green) and Macondo (light blue) are the unfiltered wireline density logs. Macondo – Sonic Transform (pink) is calculated using the sonic-to-density transform described above.

A.2.4 Interpolation Across Gaps in the Density Profile

The aggregated density data has gaps in the vertical profile (Fig. A.3). Gaps occur between and within the data sets due to multiple logging runs, casing shoes, and data removed in A.2.3. Table A.1 summarizes the data set used at each depth interval and the locations of gaps greater than 50 ft. For gaps smaller than 50 ft, the density is assumed constant and equal to the measured density above the missing interval.

I interpolate density across each of the five gaps greater than 50 ft using an empirical depth vs. porosity relationship after Athy (1930):

$$\varphi = \varphi_0 e^{-\lambda z_{sf}(ft)} \qquad \text{(Eq. A.2)}$$

where z_{sf} is depth below seafloor (ft), φ is porosity, φ_0 is porosity at the surface, and λ is an empirically derived consolidation constant (ft^{-1}). I assign a surface porosity of 0.48, the maximum porosity assuming spherical grains.

First, density measurements are converted to porosity with Eq. A.3.

$$\varphi = \frac{\rho_b - \rho_m}{\rho_f - \rho_m} \qquad \text{(Eq. A.3)}$$

where $\rho_{b,m,f}$ are bulk, matrix and fluid densities respectively. I assume that water is the predominant pore fluid and assign it a constant density of 1.024 g/cm^3 (sea water). I use a matrix density of 2.72 g/cm^3 based on measurements at MC 897-1.

Next, λ from Eq. A.2 is calibrated for each gap using porosities from 500 ft above and below the respective gap with an exponential ordinary least squares line of best fit (Fig. A.4, red line). Finally, I use Eq. A.2 (calibrated for each gap) to calculate porosity (thus density per Eq. A.3) across each gap as a function of depth.

Table A.1: Source of the density data for each depth interval.

Well	**Data Type**	**Top (ft) z_{sf}**	**Bottom (ft) z_{sf}**	**Length (ft)**
MC 897-1	MAD	0	1,986	1,985
Gap	Athy Interpolation	1,986	3,509	1,523
MC 252-1 (Texaco)	Wireline Density Log	3,509	4,509	1,000
Gap	Athy Interpolation	4,509	4,709	200
MC 252-1(Texaco)	Wireline Density Log	4,709	5,909	1,200
Gap	Athy Interpolation	5,909	5,959	50
MC 252-1 (Texaco)	Wireline Density Log	5,959	7,509	1,550
MC 296-1	Wireline Density Log	7,509	8,791	1,282
MC 252-1 (BP)	LWD Sonic Log Transform	8,791	9,970	1,179
Gap	Athy Interpolation	9,970	10,020	50
MC 252-1 (BP)	LWD Sonic Log Transform	10,020	12,015	1,995
Gap	Athy Interpolation	12,015	12,096	81
MC 252-1 (BP)	Wireline Density Log	12,096	13,199	1,103

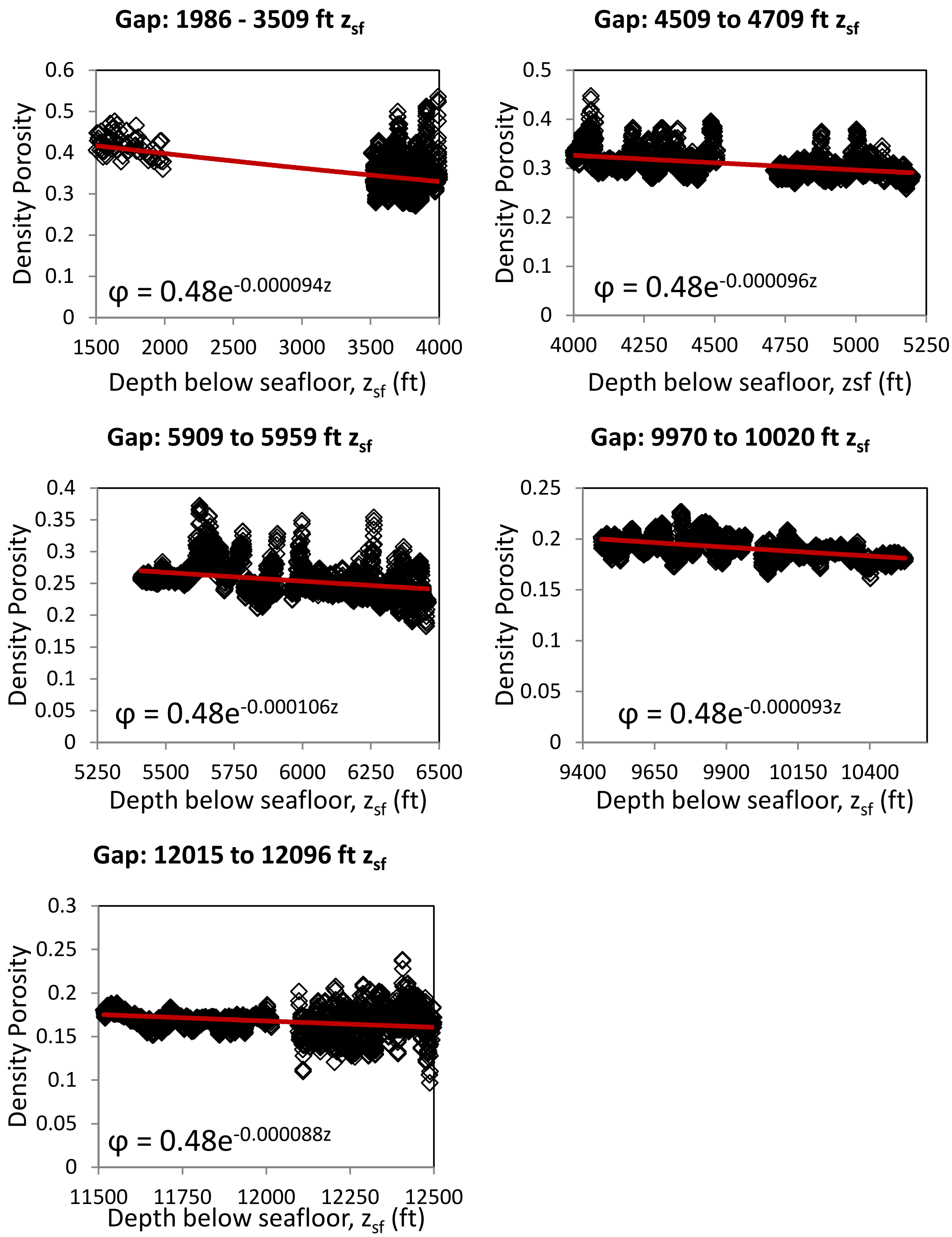

Figure A.4: Depth vs. porosity across each gap in the aggregated density profile (Fig. A.3). Aggregated density data with depth is shown with black diamonds. OLS regression of data 500 ft above and below the gap is used to calculate λ using φ_0 =

0.48. The red lines illustrate Eq. A.2 calibrated for each gap. The interpolated densities are included in Fig. A.5.

A.3 Results

A.3.1 Density Profile

Once the data are aggregated, overlaps are eliminated, and gaps are filled, the data set forms a continuous density curve with depth (Fig. A.5). Density increases rapidly near the seafloor, and then increases at a progressively slower rate with depth. Over just 300 ft, density increases by 0.5 g/cm^3; from 6 to 300 ft z_{sf}, ρ_b increases from 1.4 g/cm^3 to 1.9 g/cm^3. The next 0.5 g/cm^3 increase to 2.4 g/cm^3 occurs more gradually from 300 to 6500 ft z_{sf}

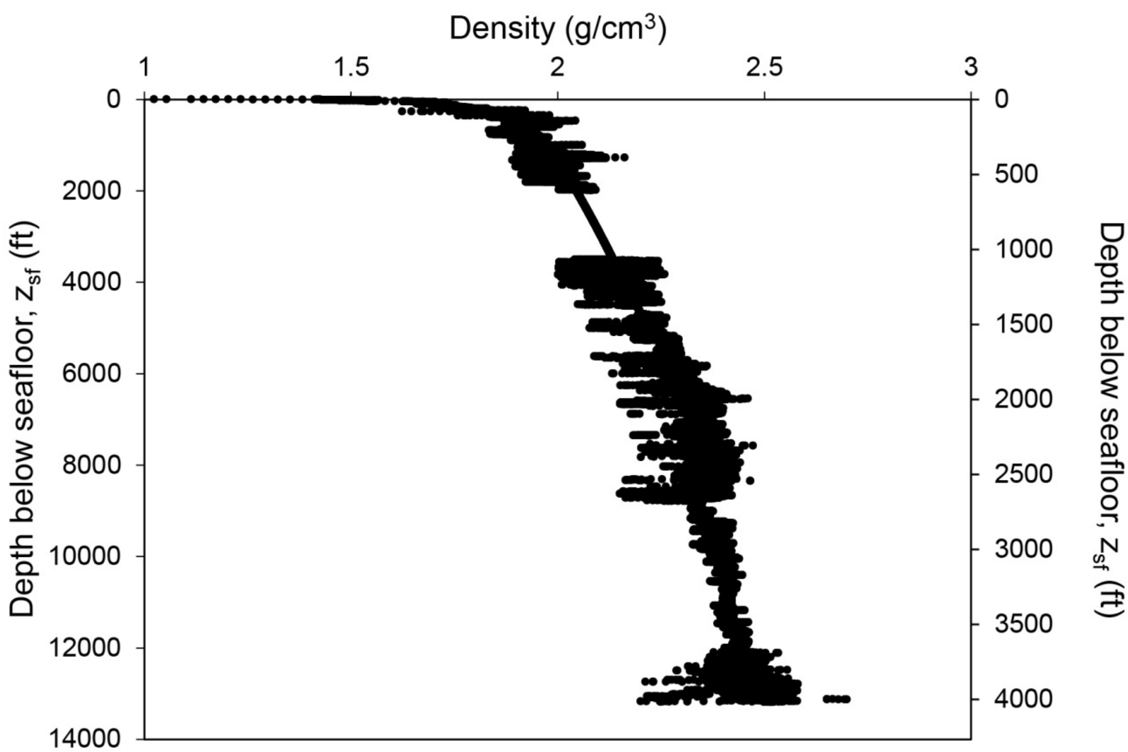

Figure A.5: Aggregated, despiked, continuous density vs. depth below seafloor.

A.3.2 Stress Profile

I calculate vertical stress from the density curve. By orienting the maximum principal stress parallel to gravity, the vertical stress becomes function of the overlying sediment and pore fluid densities. The overburden stress in a vertical borehole is described by:

$$\boldsymbol{\sigma_v = \rho_{sw} * z_{water\ depth} * g + \int_{z_{total\ depth}}^{z_{water\ depth}} \rho_b(z_{sf}) * g\ dz} \qquad \text{(Eq. A.4)}$$

where $\rho_b(z_{sf})$ is the bulk density at a given depth below the seafloor, ρ_b is the density of seawater (1.024 g/cm^3), and g is gravity.

Fig. A.6 illustrates the completed overburden model. Total stress increases from 2,200 psi at the seafloor to 15,000 psi at the M56 reservoir. At this scale, vertical stress with depth appears to increase linearly. To highlight the concavity of the curve due to increasing density, I projected a constant gradient of 0.97 psi/ft (2.24 g/cm^3) from the seafloor to the M56 reservoir.

BP produced overburden models for the Macondo well for exploration and well planning purposes (BP, 2010g); however, their methodology is proprietary and was not released during the trial proceedings. I digitized their figure for comparison with my model (Fig. A.6, green line), and the two are nearly identical.

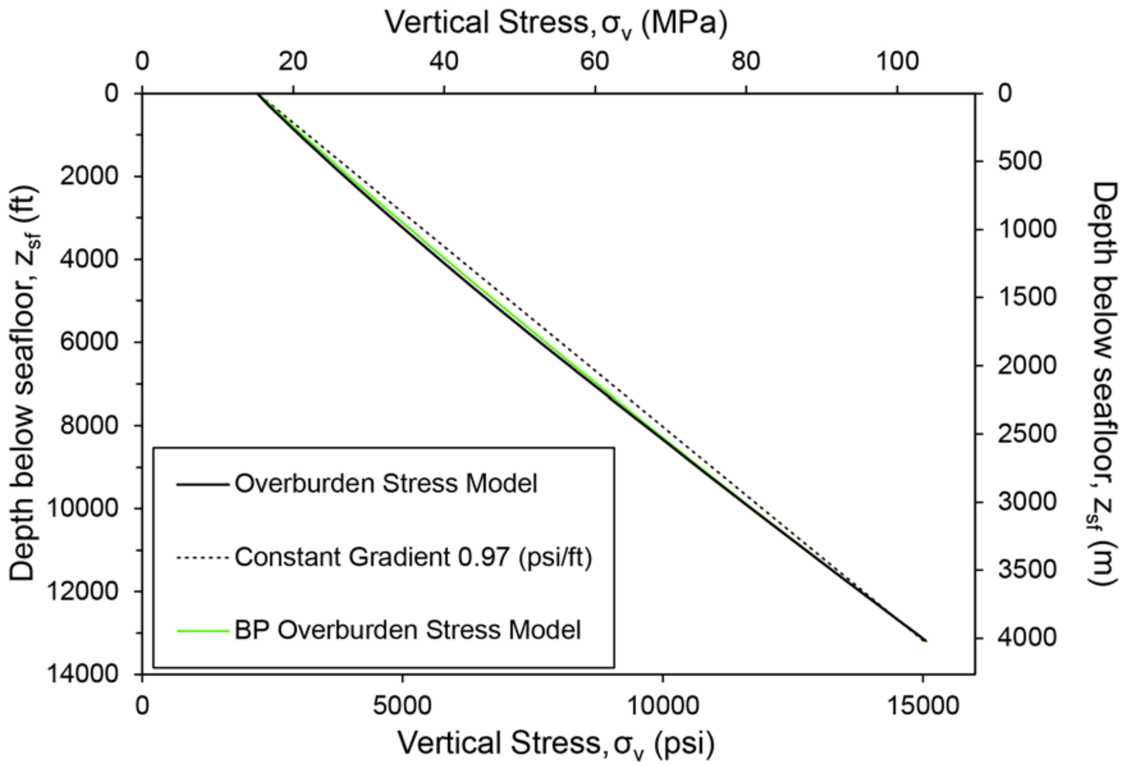

Figure A.6: Vertical stress vs. depth below seafloor profile for the Macondo well.

The black line illustrates the overburden model results. The dotted line illustrates a stress model based on constant bulk density of 2.24 g/cm^3 (0.97 psi/ft). Vertical stress at the seafloor (z_{sf} = 0) is equal to the weight of the water column. The green line shows the nearly identical model from a BP internal technical report (BP, 2010g)

The effect of increasing density with depth on the overburden stress is more clearly illustrated with an average gradient (Fig. A.7). If the effect of water depth is eliminated, the average gradient from the seafloor is calculated as:

$$\frac{d\sigma_{v\,mean}}{dz_{sf}} = \frac{\sigma_v(z_{sf}) - \sigma_{v\,water\,column}}{z_{sf}} \quad \text{(Eq. A.5)}$$

For the Macondo well, the average stress gradient measured from the seafloor rapidly increases from 0.5 to 0.8 psi/ft at 1000 ft z_{sf}, and then gradually approaches 0.97 psi/ft at 13,000 ft z_{sf}. Again, to highlight the difference between the empirical model and one in which density is assumed constant, I project the average gradient at the reservoir, 0.97 psi/ft, to the surface (Fig. A.7, dotted line).

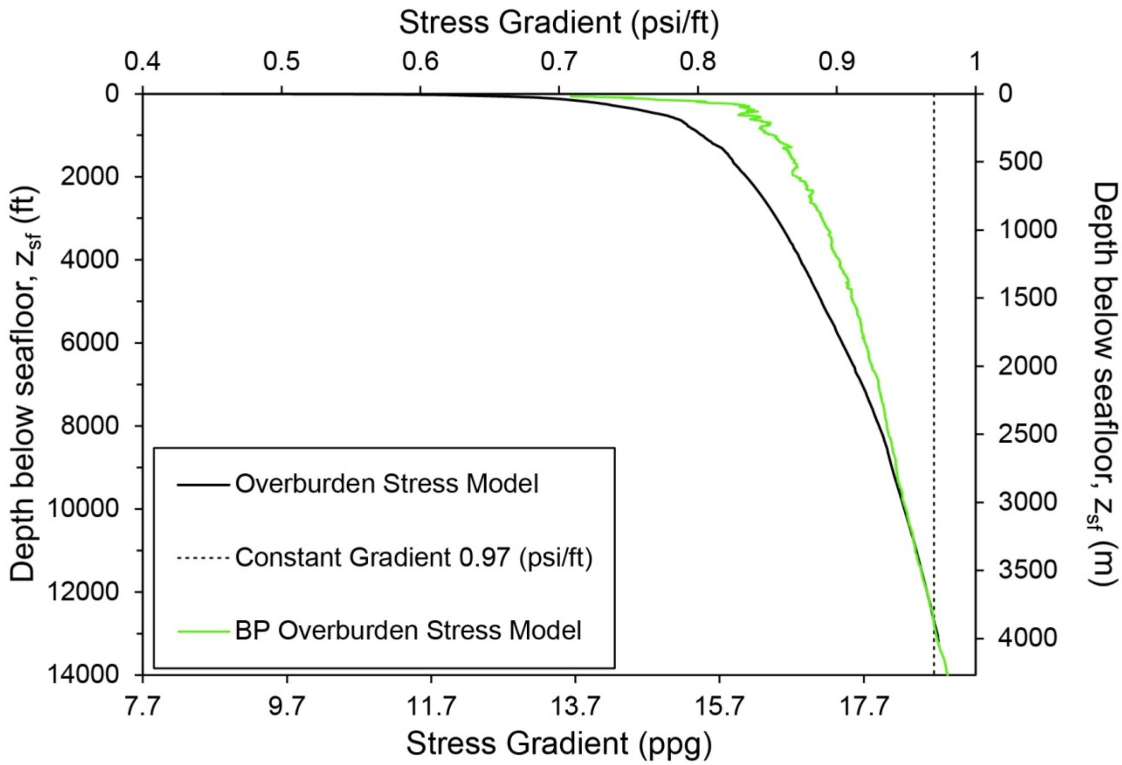

Figure A.7: Average vertical stress gradient vs depth below seafloor.

The overburden model (black line) and a stress model based on constant bulk density (dotted line) are shown as average gradients from the seafloor. The green line shows the nearly identical model from a BP internal technical report (BP, 2010g). The lower axis expresses the average gradient in equivalent mudweight density.

I also apply a modified version of this model to other regional wells to generate overburden stress profiles. By modifying the stress due to the height of the water column to match the depth of the seafloor, I apply this model to other wells in this region, including MC 562-1 (Fig. 2.3).

Table A.2: Overburden stress with depth subsea

z_{sf}	Overburden Stress
ft	psi
0	2216
100	2285
200	2361
300	2439
400	2520
500	2603
600	2687
700	2769
800	2851
900	2935
1000	3019
1100	3103
1200	3189
1300	3278
1400	3364
1500	3449
1600	3536
1700	3621
1800	3709
1900	3797
2000	3886
2100	3975
2200	4064
2300	4153
2400	4243
2500	4333
2600	4423
2700	4513
2800	4604
2900	4695
3000	4786
3100	4877
3200	4969
3300	5061
3400	5153
3500	5245
3600	5338
3700	5431
3800	5524
3900	5618
4000	5711
4100	5804
4200	5899
4300	5994
4400	6088
4500	6182
4600	6277
4700	6373
4800	6469
4900	6565
5000	6661
5100	6756
5200	6853
5300	6950
5400	7049
5500	7148
5600	7246
5700	7342
5800	7440
5900	7540
6000	7639
6100	7738
6200	7838
6300	7938
6400	8038
6500	8139
6600	8241
6700	8337
6800	8439
6900	8542
7000	8643
7100	8744
7200	8846
7300	8946
7400	9048
7500	9150
7600	9252
7700	9353
7800	9454
7900	9557
8000	9659
8100	9762
8200	9865
8300	9967
8400	10068
8500	10170
8600	10271
8700	10371
8800	10471
8900	10572
9000	10673
9100	10775
9200	10876
9300	10979
9400	11083
9500	11185
9600	11289
9700	11392
9800	11495
9900	11598
10000	11702
10100	11806
10200	11910
10300	12014
10400	12118
10500	12223
10600	12327
10700	12432
10800	12536
10900	12641
11000	12746
11100	12850
11200	12954
11300	13059
11400	13164
11500	13268
11600	13373
11700	13479
11800	13584
11900	13690
12000	13795
12100	13901
12200	14007
12300	14113
12400	14219
12500	14324
12600	14428
12700	14535
12800	14641
12900	14749
13000	14857
13100	14959
13200	15065

Appendix B: Pore Pressure Indicators

B.1 Introduction

Pore pressure indicators in permeable formations provide a framework for the pore pressure profile in a well. The quantity, quality, and depth of the indicators vary significantly on a well by well basis. LWD and wireline tools provide precise measurements, but tend to only cover short, targeted intervals of interest. Other pressure indicators include well kicks (Bradley, 1975) and background/connection gasses (Alberty and Fink, 2014). This Appendix aggregates the pressure indicators used to create Macondo pore pressure profile (2.2.1 and 2.4.2). In addition, I document the interpretations and assumptions used to determine pore pressure from each indicator, and detail the corrections applied to measurements from analog wells.

B.2 Methods

B.2.1 Macondo Pressure Measurements

The Macondo well has both LWD and wireline-measured pore pressures. LWD measurements were acquired with Halliburton's GeoTap Sensor. Wireline samples were recorded with Schlumberger's Modular Formation Dynamics Tester (MDT). Table B.1 summarizes the pore pressure measurements.

Table B.1: Summary of the LWD and wireline pressure measurements at the Macondo well. Tight/dry tests, and lost-seal tests have been excluded. The below MDT depths reflect wireline measurement. My analysis corrected all wireline measurements to driller's depth by adding 16.5 ft, based on the alignment of LWD and wireline gamma ray logs.

Depth Subsea, z_{ss}	Pore Pressure	Type
ft	psi	
18054.4	11843.2	MDT
18056.6	11844.8	MDT
18060.5	11847.9	MDT
18054.5	11850.4	MDT
18070.6	11855.3	MDT
18075.5	11863.4	MDT
18072.6	11855.8	MDT
18087.5	11857.0	MDT
18097.5	11859.4	MDT
18110.5	11862.5	MDT
18060.4	11850.5	MDT
18012.5	11838.2	MDT
17999.5	11835.0	MDT
18007.3	11839.2	MDT
18016.5	11841.0	MDT
17737.6	12038.4	MDT
17637.1	13044	GeoTap
17637.1	13037	GeoTap
17638.1	13063	GeoTap
18003.1	11845	GeoTap
18005.1	11845	GeoTap

At the Macondo well, 12 measurements are excluded. Both tools use fluid drawdown from the formation to measure pore pressure: MDT on the order of gallons to dozens of gallons, and Geotap at a rate of 1 cm^3/s. Both the drawdown rate and test duration inhibit these tools from measuring pressures in impermeable formations. Nine tests were "dry" or "tight", which meant a quick pressure draw-down phase was followed by slow pressure buildup phase due to the low permeability of the formation (Brown, 2003). Three tests were deemed "lost seal", which meant the pressure buildup phase converged with the static borehole pressure because the tool failed to form a proper seal against the borehole wall (Brown, 2003).

The measurements at the Macondo well provide pressure 17,630 to 18,110 ft z_{SS}. The 22 total measurements span 4 separate sand bodies. Fig. B.1 illustrates the sand interval thickness and location of the pressure measurements. The Macondo well spans

4992 to 18274 ft z_{ss}, and measured pore pressures only span a 500 ft interval at the base of the well, so addition indicators are used to constrain pressure.

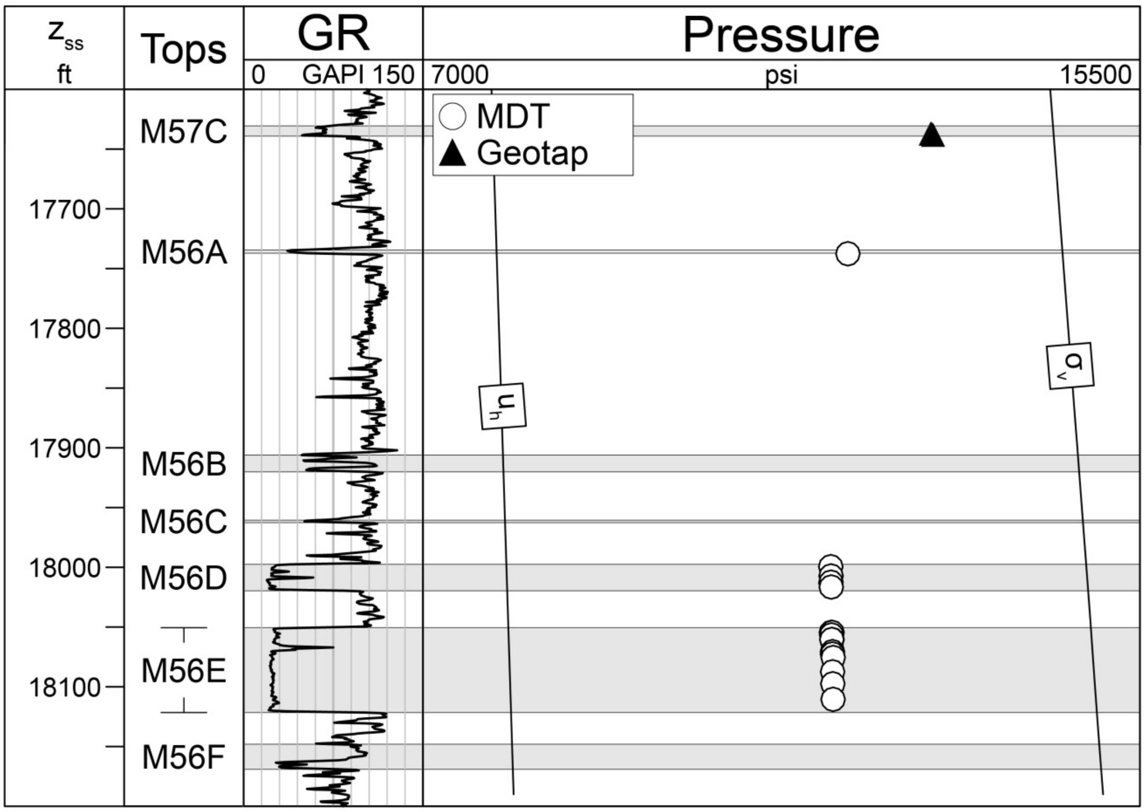

Figure B.1: Pressure vs. depth across the M57 and M56 interval at the Macondo well. Gamma ray (GR) is used to determine top and bottom of sand intervals (gray rectangles). Sand interval names follow BP nomenclature.

B.2.2 Analog Well Measurements

I depth- and pressure-correct measurements from an adjacent well, MC 252-1 (Texaco), to better constrain pore pressures at Macondo. Abandoned without production in 2000, MC 252-1 (Texaco) is located 1.27 miles southwest of the Macondo well in water depths of 5225 ft (Fig. A.1). MC 252-1 (Texaco), targeting the shallower Rigel gas prospect, recorded 70 viable in-situ MDT pressures spanning 8900 to 12500 ft z_{ss} (Table B.2). Given the proximity and similar geologic history of Macondo and MC 252-1

(Texaco), I interpret that the MDT pressures from MC 252-1 (Texaco) are representative of the in-situ pressure regime encountered at the Macondo well.

I assume that MDT-measured sands are the same depth below seafloor at both wells. A 217 ft depth correction is applied to the original measurements based off of the wellhead bathymetric difference. I also assume that the sands are continuous and hydraulically connected, such that pressure follows the hydrostatic gradient of seawater (Fig. B.2); thus a 96 psi pressure correction is applied to each point. Table B. lists the original MDT depths and pressures of MC 252-1 (Texaco) and the values projected to the Macondo well. The low dip angle and short distance between MC 252-1 (Texaco) and the Macondo well results in small depth and pressure corrections. Fig. B.3 shows the difference between the original and corrected MDT measurements.

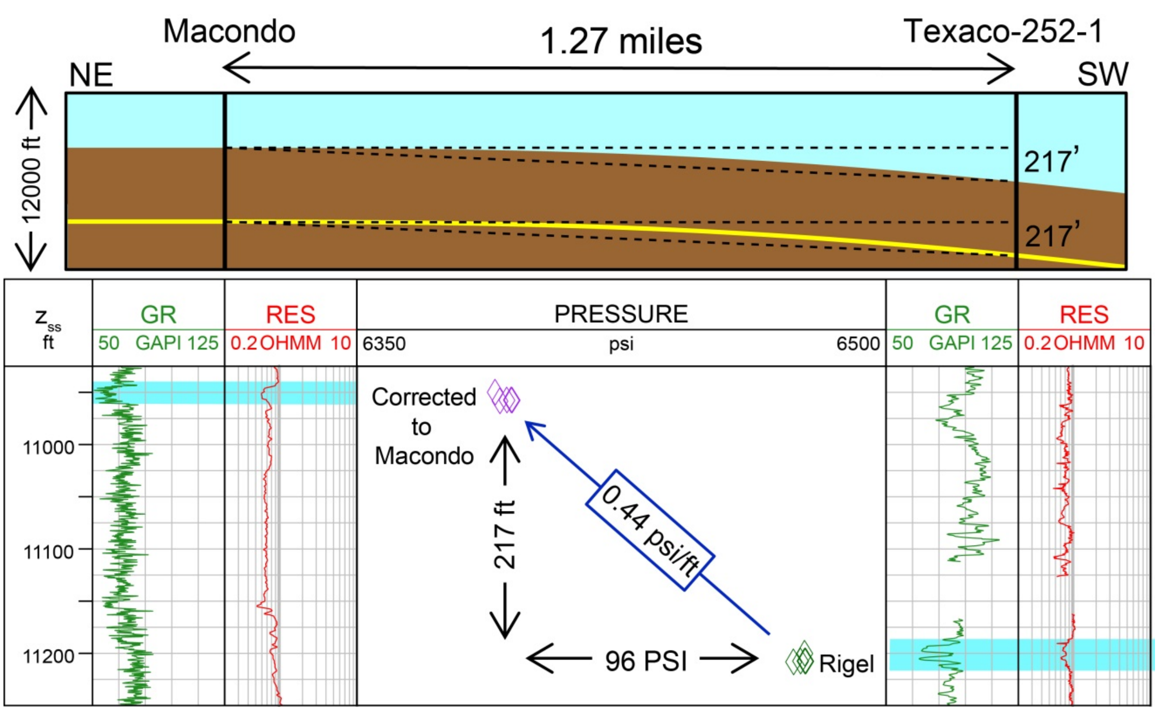

Figure B.2: Pressure and depth correction applied to MC 252-1 (Texaco) pore

pressure measurements. Above: Cartoon illustrates our assumptions that the sands at MC 252-1 (Texaco) and Macondo are (1) the same depth below seafloor, (2) hydraulically connected, and (3) water bearing. Below: Gamma ray, resistivity, and pressure at the Macondo (left) and MC 252-1 (Texaco) (right) wells. The green diamonds denote the original pressure measurements at MC 252-1 (Texaco). Purple diamonds record the depth and pressure correction using the hydrostatic gradient (blue arrow).

Table B.2: MDT measurements for MC 252-1 (Texaco)

Original		Projection	
z_{ss}	Pore Pressure	z_{ss}	Pore Pressure
ft	psi	ft	psi
8918.51	4797.12	8701.5	4700.8
8918.96	4796.67	8702.0	4700.3
8978.72	4807.88	8761.7	4711.5
8986.68	4810.43	8769.7	4714.1
9097.43	4931.06	8880.4	4834.7
9099.14	4931	8882.1	4834.7
9113.54	4931.72	8896.5	4835.4
9113.97	4932.61	8897.0	4836.3
9116.11	4932.81	8899.1	4836.5
9117.73	4932.86	8900.7	4836.5
9117.86	4933.14	8900.9	4836.8
9120.31	4933.05	8903.3	4836.7
9201.04	5011.23	8984.0	4914.9
9201.66	5011.84	8984.7	4915.5
10588.07	6124.79	10371.1	6028.4
10806.17	6407.04	10589.2	6310.7
10812.8	6409.84	10595.8	6313.5
10814.46	6409.13	10597.5	6312.8
10816.09	6410.34	10599.1	6314.0
10819.4	6395.25	10602.4	6298.9
10820.25	6410.7	10603.3	6314.4
10822.66	6411.84	10605.7	6315.5
10825.21	6411.08	10608.2	6314.7
10826	6420.85	10609.0	6324.5
10827.79	6411.55	10610.8	6315.2
10829.22	6411.96	10612.2	6315.6
10832.47	6412.33	10615.5	6316.0
10836.67	6412.92	10619.7	6316.6
10841.62	6413.07	10624.6	6316.7
10843.24	6412.66	10626.2	6316.3
10844.9	6413.41	10627.9	6317.1
10849.01	6412.79	10632.0	6316.4
10850.61	6414.11	10633.6	6317.8
10852.27	6412.93	10635.3	6316.6
10855.67	6414.7	10638.7	6318.4
10858.79	6414.24	10641.8	6317.9
10859.73	6414.63	10642.7	6318.3
10863.8	6415.21	10646.8	6318.9
10867.11	6415.17	10650.1	6318.8
10870.46	6415.61	10653.5	6319.3
10876.57	6416.14	10659.6	6319.8
10881.2	6416.74	10664.2	6320.4
10886.8	6417.4	10669.8	6321.1
10908.25	6420.52	10691.3	6324.2
11199.94	6469.28	10982.9	6372.9
11207.4	6469.36	10990.4	6373.0
11207.4	6469.66	10990.4	6373.3
11207.4	6467.7	10990.4	6371.4
11208.25	6465.06	10991.3	6368.7
11464.01	6561.32	11247.0	6465.0
11464.88	6534.35	11247.9	6438.0
11465.7	6537.59	11248.7	6441.2
11466.58	6584.9	11249.6	6488.6
11469.03	6570.61	11252.0	6474.3
11469.06	6587.42	11252.1	6491.1
11469.08	6769.82	11252.1	6673.5
11469.88	6587.85	11252.9	6491.5
11469.91	6587.24	11252.9	6490.9
11470.72	6587.49	11253.7	6491.1
11577.69	6817.38	11360.7	6721.0
11885	7015.09	11668.0	6918.7
12082.67	7359.61	11865.7	7263.3
12093.87	7314.26	11876.9	7217.9
12094.79	7319.1	11877.8	7222.8
12526.4	7593.33	12309.4	7497.0
12555.81	7670.69	12338.8	7574.3
12557.72	7670.75	12340.7	7574.4
12562.32	7671.03	12345.3	7574.7
12564.17	7671.28	12347.2	7574.9
12565.06	7671.29	12348.1	7574.9

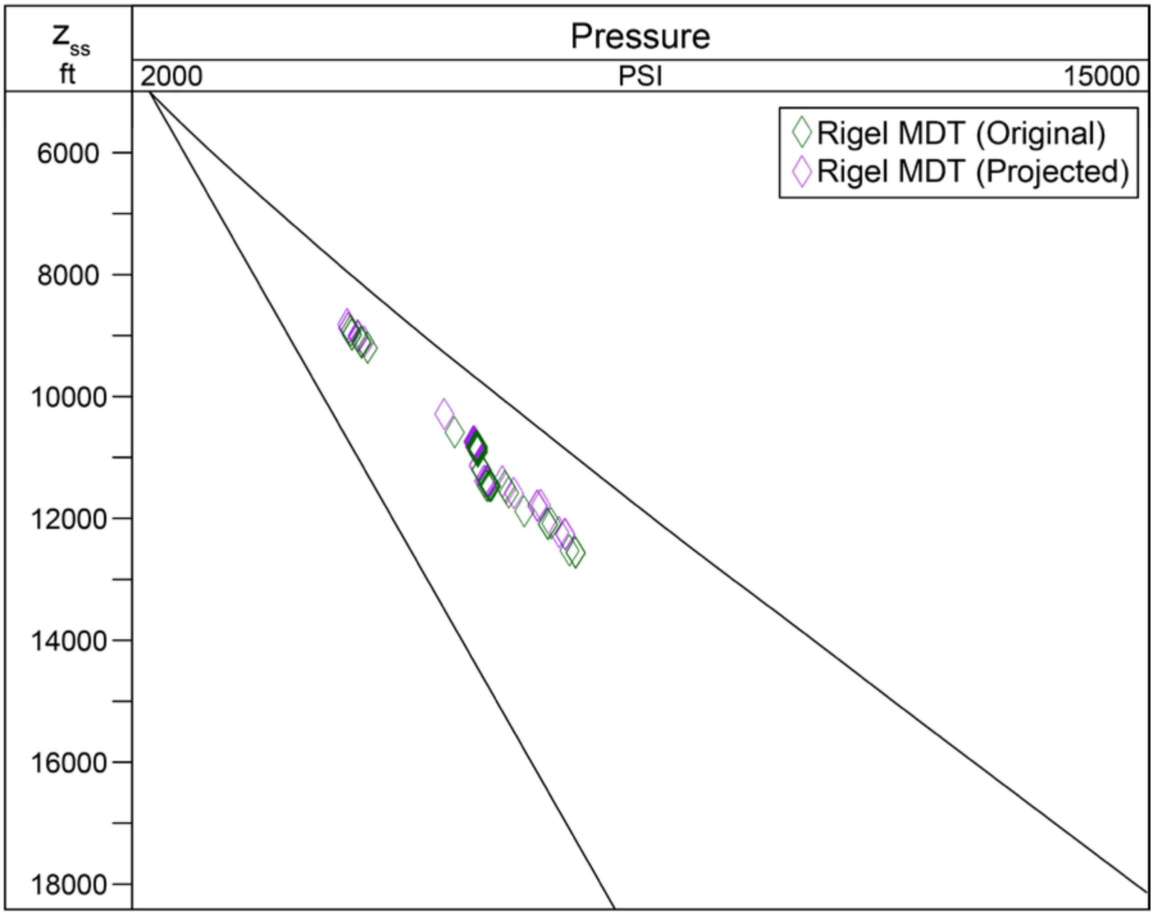

Figure B.3: Pressure vs. depth profile of the Macondo well with corrected and uncorrected MC 252-1 (Texaco) MDT measurements. The pressure vs depth profile spans the seafloor to the bottom of the Macondo well. Green diamonds record the uncorrected values and purple diamonds show my applied depth and pressure correction.

B.2.3 Formation Fluid Influx or 'Kick' Analysis

I also constrain pore pressure at the Macondo with another widely used pressure indicator informally known as a 'kick' (Bradley, 1975). During a kick, pore fluids enter the wellbore because pressure in the wellbore is less than the pressure in the formation. The Macondo well experienced multiple fluid influxes of varying severity, each of which provides information about pore pressure. In the following subsections, I paraphrase the circumstances surrounding each event using end of well reports (Halliburton, 2010a, b), daily drilling logs, daily geological & PPFG reports, and well section review summaries. I then analyze each event to determine its location along the exposed borehole and an estimate of the pore pressure, incorporating BP's analysis of the kick.

Kicks are detected in a variety of ways (see Transocean (2009) pp. 70 for complete list). I focus on increases in the volume of the mud pit or trip tank and continued flow after mud pumps are turned off (during a 'flow check'). In a closed hydraulic loop, the volume of mud injected into the drill pipe roughly equals the mud volume (minus cuttings) coming out of the annulus, so volume increases in the system can often be attributed to pore fluid influx. If the exposed formation is impermeable, then a kick may go undetected because the volume and rate of pore fluids entering the wellbore may not cause a perceptible change in the volume of mud in the system. I also focus on a third means of kick detection: the gas levels in the returning mud measured by a chromatograph. As the drill bit penetrates a gas-bearing porous formation, the gas liberated from the pulverized formation becomes entrained or dissolved in the circulating mud and is detected at the surface as "background gas". Increasing gas levels may indicate that pore pressures are approaching the borehole pressures (Transocean, 2009).

Constraining the location of a kick is important for determining the pressure, because the depth is required to calculate the pressure from the mudweight. A kick taken while drilling new formation likely originates at the base of the wellbore, provided that the overlying pressure remains unchanged. If a kick occurs as a result of a reduction in downhole pressure (e.g. a mudweight reduction, swabbing, cuttings load settling), the kick location is not easily constrained.

I estimate pore pressure from kicks in three ways. In all three cases, ESD and ECD measured downhole are preferable to surface mudweight measurements (see 2.4.2 for complete description). (1) If the well is shut-in during the kick, then the pore pressure and confined wellbore pressure reach equilibrium. If the formation fluids do not displace fluids in the drill pipe, downhole pore pressure is calculated by adding the shut in drill pipe pressure (SIDPP) measurement and the static pressure exerted by the mud (Transocean, 2009):

$$\mathrm{u\ (psi)} = \frac{\mathrm{MW\ (ppg)}}{19.25} * \mathrm{z(ft)} + \mathrm{SIDPP(psi)} \qquad \text{(Eq. B.1)}$$

(2) If the well is not shut in during a kick or shut-in pressure is unavailable, then I constrain pore pressure with other drilling information. The ECD when the kick is taken represents the lower bound of the pore pressure. The ECD required to kill the flowing well or the ESD once the well is static is used as the upper pore pressure bound.

(3) A kick may also result from borehole pressure reduction. Mud circulation cutoff, mud density reduction, mud dilution by pore fluids all has the net effect of reducing borehole pressure. During drill pipe connections, mud pumps are turned off, allowing the hydraulic system to become static (Alberty 2014). If the dynamic to static pressure decrease causes the pressure at any point in the wellbore to drop below the pore pressure, fluids may influx into the borehole. This scenario is often detected as “connection gases”, mud gas levels above the background gas level following a drill-pipe connection. In this third case, borehole pressures before and during the event serve as the upper and lower pore pressure bounds respectively.

Table B.3: Kick summary: The pore pressure was calculated using the mean of the upper and lower pore pressure bound in psi (except for 7505 ft z_{ss} kick, which uses the upper bound only). Pore pressure (ppg) is referenced to the Deepwater Horizon drill floor. The upper and lower bounds are referenced to the drill floor of the rig at the time of the kick.

z_{ss}	Pore Pressure	Pore Pressure	Pore Pressure Upper Bound	Pore Pressure Lower Bound
ft	psi	ppg	ppg	ppg
7505	3629	9.22	9.20	8.90
8874	4737	10.19	10.24	10.11
12159	7305	11.50	11.53	11.46
13172	8549	12.42	12.42	12.42
14495	10029	13.25	13.30	13.20
17399	12854	14.16	14.22	14.10

B.2.3.1 Kick at 7505 ft z_{ss}

I interpret that the pore pressure is between 9.2 and 8.9 ppg EMW at 7505 ft z_{ss} (Fig. B.4, Table B.3). No flow was recorded while drilling with seawater (8.54 ppg, ECD 8.6 to 9.3 ppg) the 26" hole section from 28" casing shoe at 6142 ft z_{ss} to end of the hole section at 7912 ft z_{SS}. I interpret that pore pressure is below the ECD. However, the well flowed during casing operations (Bodek et al., 2009) after the riserless pad was then filled from 4982 to 7912 ft z_{ss} with 12 ppg mud (Fig. B.4, upper brown line): static EMW varied from 9.07 ppg at 6142 ft z_{ss} (casing shoe) to 9.72 ppg at 7912 ft z_{ss} (bottom hole). The static pressure from the emplaced 12 ppg mud and overlying seawater column exceeded the ECD, so the well should have remained static after circulation stopped; it did not.

It is possible that flow occurred during drilling and was not detected. I use a second interpretation: the static borehole pressure decreased below the pore pressure. The static pressure reduction could have occurred if cuttings and barite settled out of the mud column. Alternatively, the 12 ppg mud could have fractured the borehole and entered the formation. This would have lowered the mud level in the borehole (Fig. B.4, lower brown line). Mud at the top of the pad would have been replaced with lower-density seawater, thus reducing the static borehole pressure.

I use the gamma ray log to locate sand intervals that are potential sources of the kick. The first significant sand interval at 6750 ft z_{ss} was drilled with an ECD of 8.9 ppg, which I interpret to be the lower pore-pressure bound of this event. Sand intervals near 7500 ft z_{ss} experienced an ECD of 9.2 ppg, and I interpret this to be the upper pore-pressure bound. Were pore pressures in the ~9.7 ppg EMW range (the static pressure after mud emplacement at the base of the borehole section), one would expect dramatic water flow during drilling, given the low density of the seawater used (Boudek 2009). I interpret that the location of the brine influx is the eight-foot thick sand at 7505 ft z_{ss} with a resistivity signature well below the shale baseline.

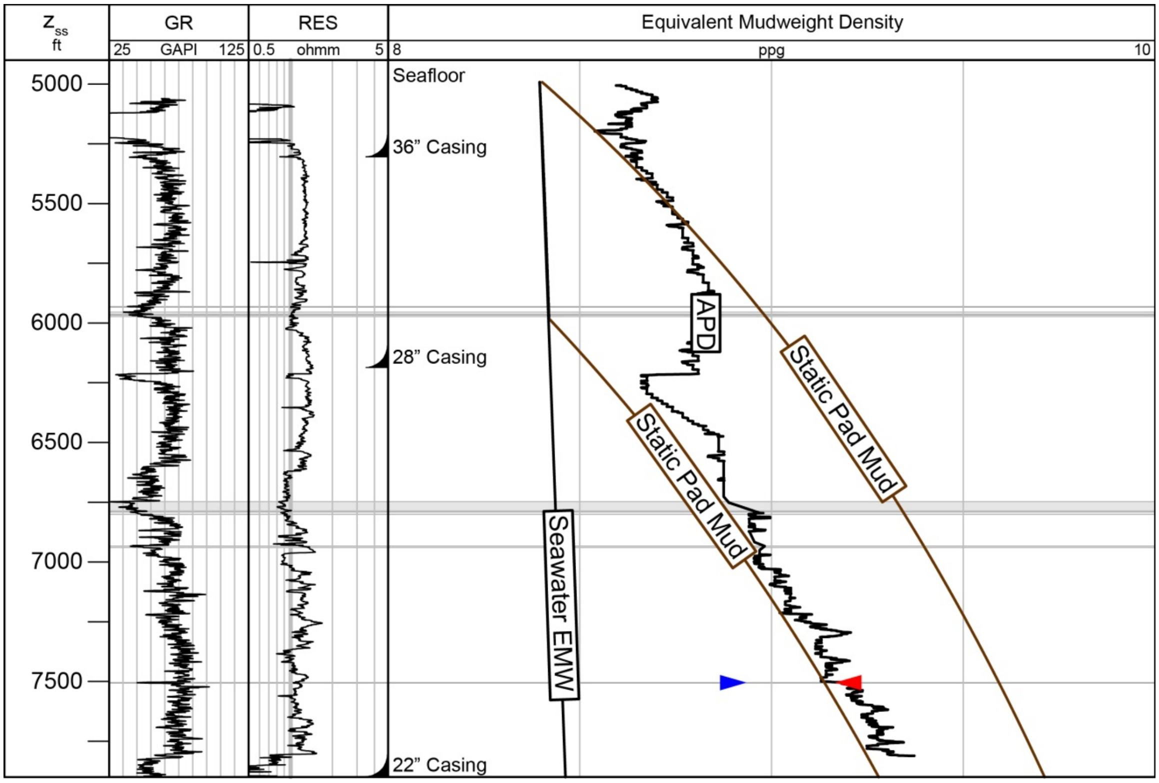

Figure B.4: Equivalent mudweight vs. depth profile of the 7505 ft z_{ss} kick. Red and blue triangles denote the location, and upper and lower pore-pressure bounds interpreted for this kick. The upper brown line records the EMW of the 12 ppg pad mud assuming that the borehole is filled to the well head. The lower brown line illustrates the borehole pressure if the pad mud level were to fall by 1000 ft. The 26” borehole section was drilled with seawater without the riser connecting the annulus to the drill floor. Because this plot shows average density projected to the Marianas drill floor, the constant seawater density (8.52 ppg) is not constant as an EMW. The sand intervals (gray rectangles) are picked using the gamma ray (GR) and resistivity (RES) logs.

B.2.3.2 Kick at 8874 ft z_{ss}

I interpret that the pore pressure is between 10.05 and 10.24 ppg EMW at 8874 ft z_{ss} (Fig. B.5, Table B.3). The second kick occurred in the 16.5” x 20” hole section while drilling from 8824 to 8881 ft z_{ss} (Fig. B.4). The well was static during connections at 8784 and 8824 ft z_{ss}, but a flow check at 8881 showed the well was flowing. The well was shut in and allowed to equilibrate with the pore pressure. The shut-in drill pipe pressure was 120 psi and annulus pressure was 90 psi. This implies that the drill pipe fluid was less dense than the annular fluid, even with dilution from the influx of formation fluid. Surface mudweight prior to the kick was 9.8 ppg, and an ESD of 9.98 was recorded at a recent flow check (BP, 2009a). The SIDPP of 120 psi (Fig. B.4, red dashed line) is added to the ESD of 9.98 ppg (Fig. B.4, solid red line) (Eq. B.2), to calculate a pore pressure of 4767 psi or 10.24 ppg EMW. The ESD measurement was recorded at the last flow check and may have changed, so I also include the ECD as a lower pore pressure bound.

Even though the borehole was exposed between 7863 and 8881 ft z_{ss}, the kick most likely originated between 8824 and 8881 ft z_{ss} because the mudweight was unchanged. A three-foot thick sand at 8874 ft z_{ss} with a resistivity signature above shale baseline may be the source of the gas influx.

I interpret the next kick to have been a continuation of the previous event. After the well-kill operations at 8881 ft z_{ss}, drilling continued to 8974 ft z_{ss}. Here, a flow check indicated that the well was static, so I interpret that the pore pressure is less than the ESD of 10.26 ppg. Drilling continued to 8984 ft z_{ss} with reduced mudweight (10.05 ppg SMW, ECD of 10.3 ppg). A flow check revealed a kick during drilling. Circulation continued without further gains, and an ESD of 10.24 ppg was recorded post circulation. I interpret this to be the upper bound. ESD during the kick was not noted, and the well was not shut in. I interpret the 10.05 ppg SMW to be the lower pore pressure bound. The lower bound is below the observed pressure in the previous kick. This, combined with the absence of sandy intervals in the newly drilled section, suggests reactivation of the previous kick.

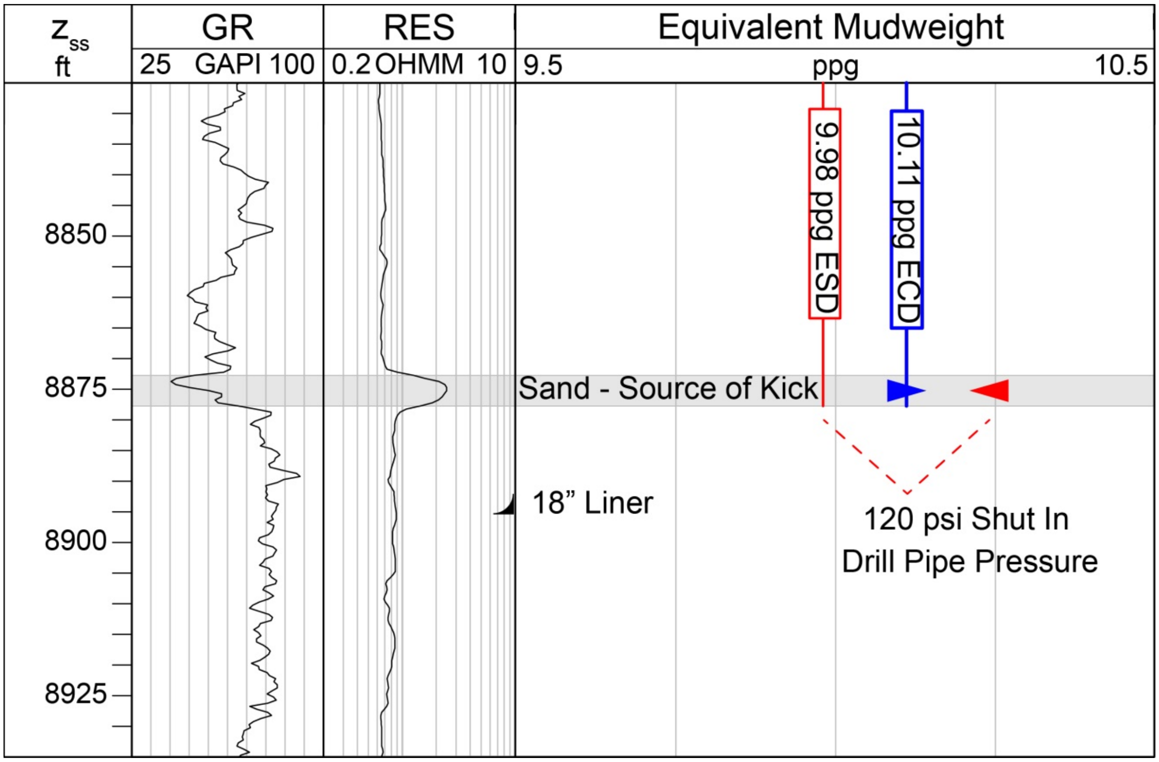

Figure B.5: Equivalent mudweight vs. depth profile of the 8874 ft z_{ss} kick. Yellow rectangle highlights the sand that was the likely location of the kick. The sand interval is interpreted from the gamma ray (GR) and resistivity (RES) logs. The kick occurred during drilling as the bit penetrated this sand. The red line shows the last recorded ESD projected to the kick depth and the blue line is the projected ECD. The red dashed line shows the addition of the SIDPP to static density. Red and blue triangles denote the location and upper and lower pore pressure bounds from this kick. EMW calculations use the Marianas dill floor.

B.2.3.3 Background Gas at 12159 ft z_{ss}

I interpret that the pore pressure is between 11.46 and 11.53 ppg EMW at 12159 ft z_{ss} (Fig. B.6, Table B.3). Following the rig change and reentry operations by the *Deepwater Horizon*, drilling commenced from 9001 to 12166 ft z_{ss} with background gas levels of 60 to 150 units (Fig. B.5, gray rectangles) (Halliburton, 2010b). ECD while drilling from 11811 to 12166 ft z_{ss} was 11.46 ppg. The deepest connection-gas-free drill-pipe connection was recorded at 11897 ft z_{ss}. Upon picking up off the bottom to circulate at 12166 ft z_{ss}, gas levels jumped to 2970 units (Fig. B.5, red dot), cutting the density of the returns from 11.1 to 10.6 ppg. I interpret that high permeability sands fluxed gas into the system during this connection. The pressure decrease resulting from halted circulation (and any additional swabbing effects) was sufficient for significant volumes of gas to enter the borehole. By increasing the mudweight to 11.4 ppg and circulating bottoms up, BP reduced gas readings to background levels(Halliburton, 2010b).

After raising the mudweight and circulating out the gas at 12166 ft z_{ss}, BP recorded an ESD of 11.53 ppg, a static flow check, and gas levels back below 200 units: this serves as the upper pore pressure bound. I interpret the lower bound to be 11.46 ppg from the ECD during drilling. I could not constrain the pressure drop due to swabbing. Despite the length of the exposed borehole, I constrain the influx source below 11895 ft z_{ss} where connection gas spikes are last absent. A five-foot thick sand at 12159 ft z_{ss} with a strong positive resistivity signature may be the source of the gas influx.

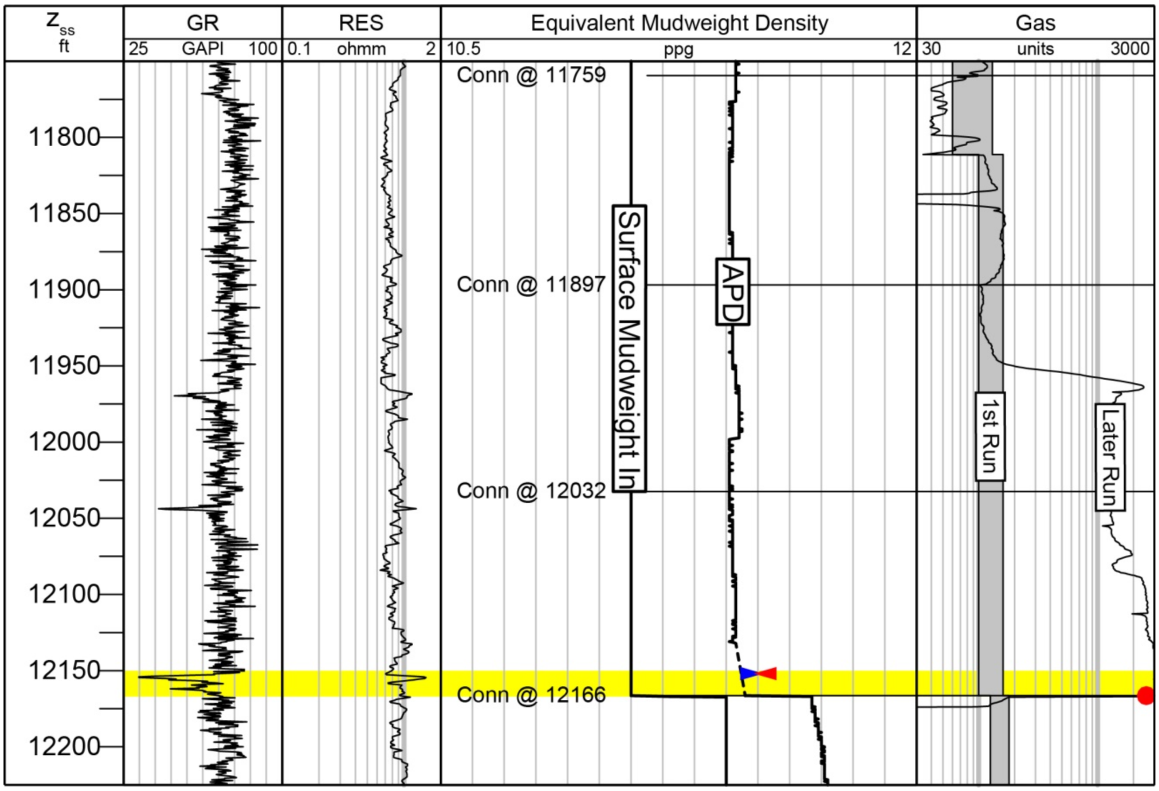

Figure B.6: Equivalent mudweight vs. depth profile of the 12159 ft z_{ss} gas event. The yellow rectangle highlights the connection gas at 12166 ft z_{ss} gas due to pore pressure converging on the static borehole pressure. The sand top and bottom are estimated from the gamma ray (GR) and resistivity (RES) logs. Red and blue triangles denote the location and upper (11.53 ppg ESD after SMW was increase) and lower (11.46 ppg ECD during drilling) pore pressure bounds for this event. Background gas from the drilling logs is shown in gray. The black line shows gas levels when the interval was drilled a second time after cementing the 16” liner in place. EMW calculations use the Deepwater Horizon drill floor.

B.2.3.4 Kick at 13164 ft z_{ss}

I interpret that the pore pressure is 12.42 ppg EMW at 13164 ft z_{ss} (Fig. B.7, Table B.3). While drilling from 12767 to 13294 ft z_{ss}, the trip tank gained 35 bbl, ECD dropped from 12.4 to 12.32 ppg, and a subsequent flow check confirmed a pore fluid influx into the wellbore. The well was shut in multiple times during well control operations, and the SIDPP varied between 380 and 150 psi (Halliburton, 2010b). My interpretation uses 360 psi, the SIDPP after the stuck drill pipe was severed downhole. The downhole annulus pressure measured 12.32 ppg ECD immediately prior to the incident, but the ESD is not available so I use the surface mudweight of 11.9 ppg. The 360 psi SIDPP and 11.9 ppg SWM yield a pore pressure of 12.42 ppg (Eq. B.2). This calculation may underestimate pore pressure, because it uses a surface measurement. The estimate is only slightly higher than the 12.4 ppg ECD during drilling. The first connection gas spike appears at 13123 ft z_{ss}, so the kick most likely originated from a nearby sand interval. I interpret that the four-foot thick sand at 13173 ft z_{ss} with a strong positive resistivity signature is the source of the gas influx.

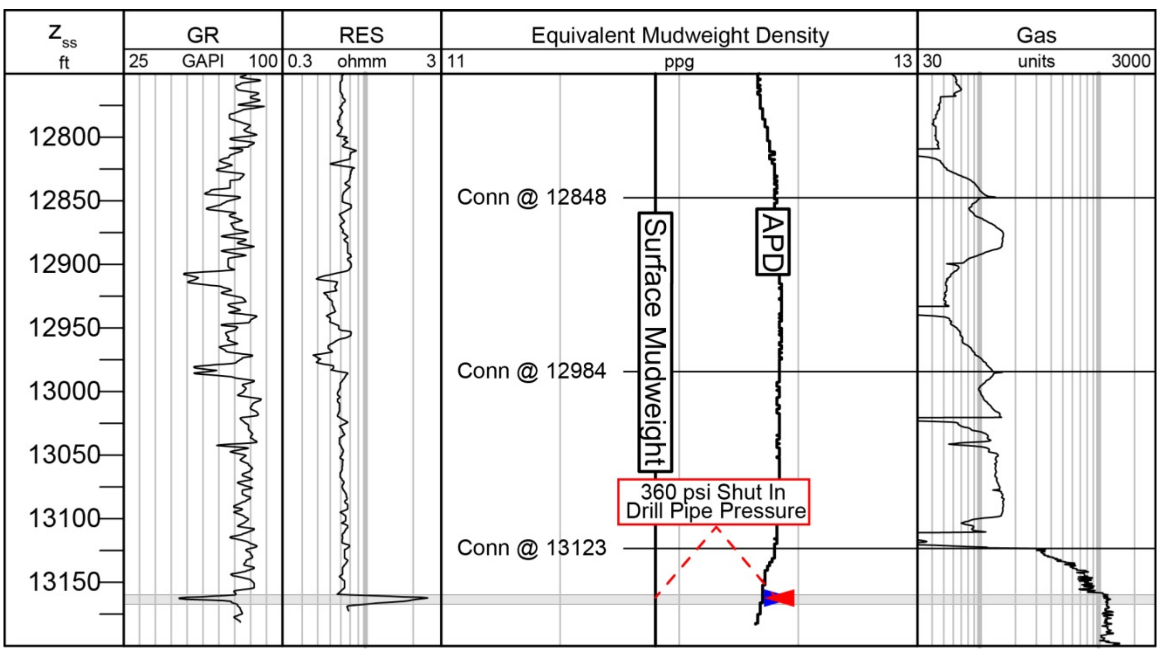

Figure B.7: Equivalent mudweight vs. depth profile of the 13164 ft z_{ss} kick. The overlapping red and blue triangles denote the interpreted pore pressure and location of this kick.

B.2.3.5 Connection Gas at 14495 ft z_{ss}

I interpret that the pore pressure is between 13.2 and 13.3 ppg EMW at 14495 ft z_{ss} (Fig. B.8, Table B.3) from the background gas response to ECD changes. The 12-1/4" x 14-1/2" hole section spans 13059 to 15017 ft z_{ss}. A gas-bearing sandstone at 14285 ft z_{ss} appears to have caused a spike in the gas reading of the incoming mud. However, the first indicator that pore pressure is approaching the borehole pressure occurs during the connection at 14357 ft z_{ss}. The surface mudweight was 13.2 ppg and max gas was 90 units (above background levels of 64 units) so gas was circulated out of hole after the connection (Halliburton, 2010b). Prior to the connection at 14495 ft z_{ss}, background gas appears to be increasing (Fig. B.8, upper yellow rectangle), even though no resolvable sands appear on the log. Here, I interpret that pore pressure is converging on static borehole pressure. After the connection at 14496 ft z_{ss}, the surface mudweight was increased to 13.3 ppg and gas levels decreased (Fig. B.8, lower yellow rectangle). I use the surface mudweights of 13.2 and 13.3 ppg as the lower and upper pore pressure bounds respectively (Fig. B.8, blue and red triangles).

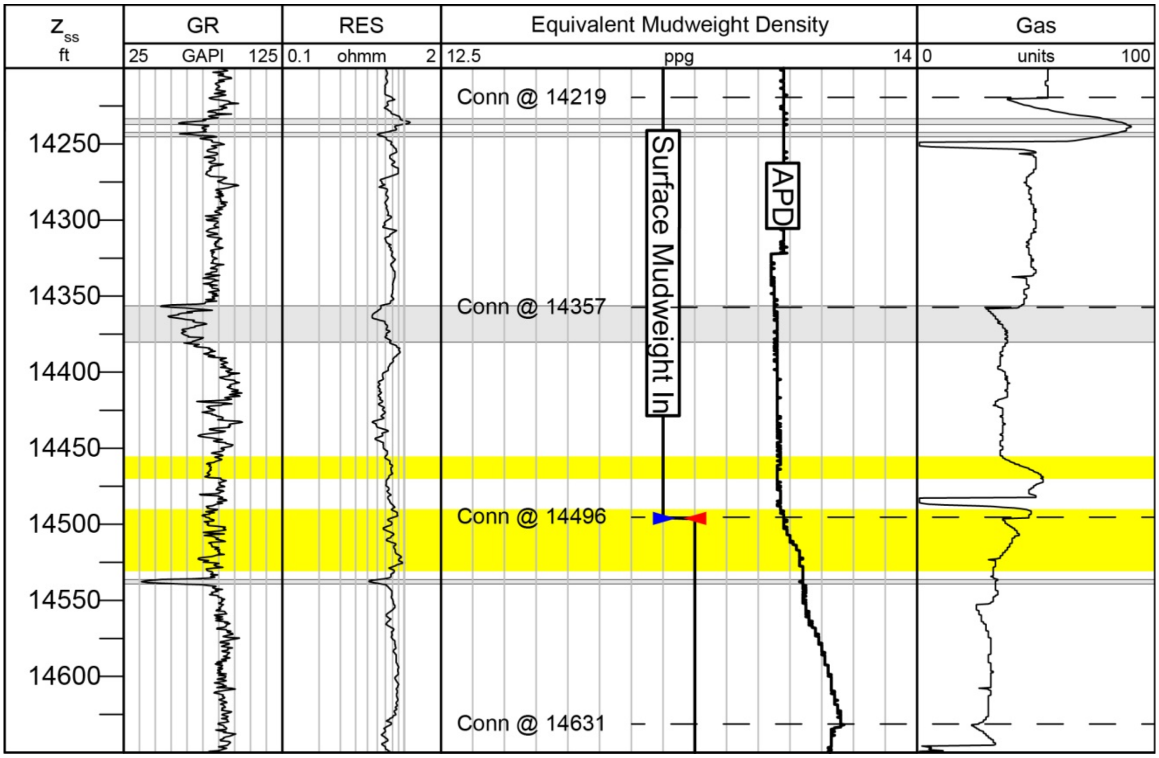

Figure B.8: Equivalent mudweight vs. depth profile of the 14495 ft z_{ss} gas event. The yellow rectangles highlight the increasing background gas due to pore pressure converging on the borehole pressure (upper rectangle) and the decreasing background gas after the mudweight was increased. The sand top and bottom are picked using the gamma ray (GR) and resistivity (RES) logs. Red and blue triangles denote the location and upper and lower pore pressure bounds from this event.

B.2.3.6 Connection Gas at 17399 ft z_{ss}

I interpret that the pore pressure is between 14.1 and 14.22 ppg EMW at 17399 ft z_{ss} (Fig. B.9, Table B.3). The 8-1/2” x 9-7/8” hole section was drilled from the 9-7/8” casing shoe at 17082 to 17235 ft z_{ss} with a 14.3 ppg SMW and a 14.52 ppg ESD with no connection gasses (Halliburton, 2010b). While increasing the surface mudweight to 14.5 ppg (14.71 ppg ESD), drilling continued to 17548 ft z_{ss}. Between 17548 and 17675 ft z_{ss}, BP lost partial returns (3.2.2.5). After spotting an LCM pill and regaining full returns, drilling proceeded to 17749 ft z_{ss}. Here, while circulating and lowering the surface mudweight to 14.3 ppg, the well flowed back 16 bbl and with max gas of 309 units. I agree with BP's interpretation (Halliburton, 2010b) that this flow is a result of ballooning (mud reentering the borehole from fractures as borehole pressure is reduced below the least principal stress) and therefore not an indicator of pore pressure. While drilling ahead (ECD 14.9 ppg, ESD 14.5 ppg), the driller noted connection gases at 17964 (156 units) and again at 18129 (786 units) with low mud cut of 14.1 ppg (Fig. B.9, red dots).

Pore pressures are well constrained below 17749 ft z_{ss}. Multiple MDT measurements record the onset of the regression; therefore, I interpret that the source of the gas is above 17749 ft z_{ss}. The first uptick in background gas occurs at 17350 ft z_{ss} (Fig. B.9, yellow rectangle), despite increasing static and dynamic borehole pressures, so I interpret that the sand at 17,399 ft z_{ss} is the source of the gas. The connection gasses in the lower half of the well section could imply that pore pressures are between the 14.5 ppg ESD and the 14.9 ppg ECD. However, after the hole reached TD at 18274 ft z_{ss}, the well was static with a downhole ESD 14.22-14.26 ppg, and background gas was below 40 units with and ECD between 14.4 and 14.5 ppg. Therefore I interpret the upper pore pressure bounds to be 14.22 ppg (the static borehole pressure at TD) and 14.1 ppg (the surface density of the gas cut returns at 18129 ft z_{ss}; Fig. B.9, red dashed line). Our interpretation is consistent with the pore pressure of 14.18 ppg in the sand at 17637 ft z_{ss} recorded by the Geotap.

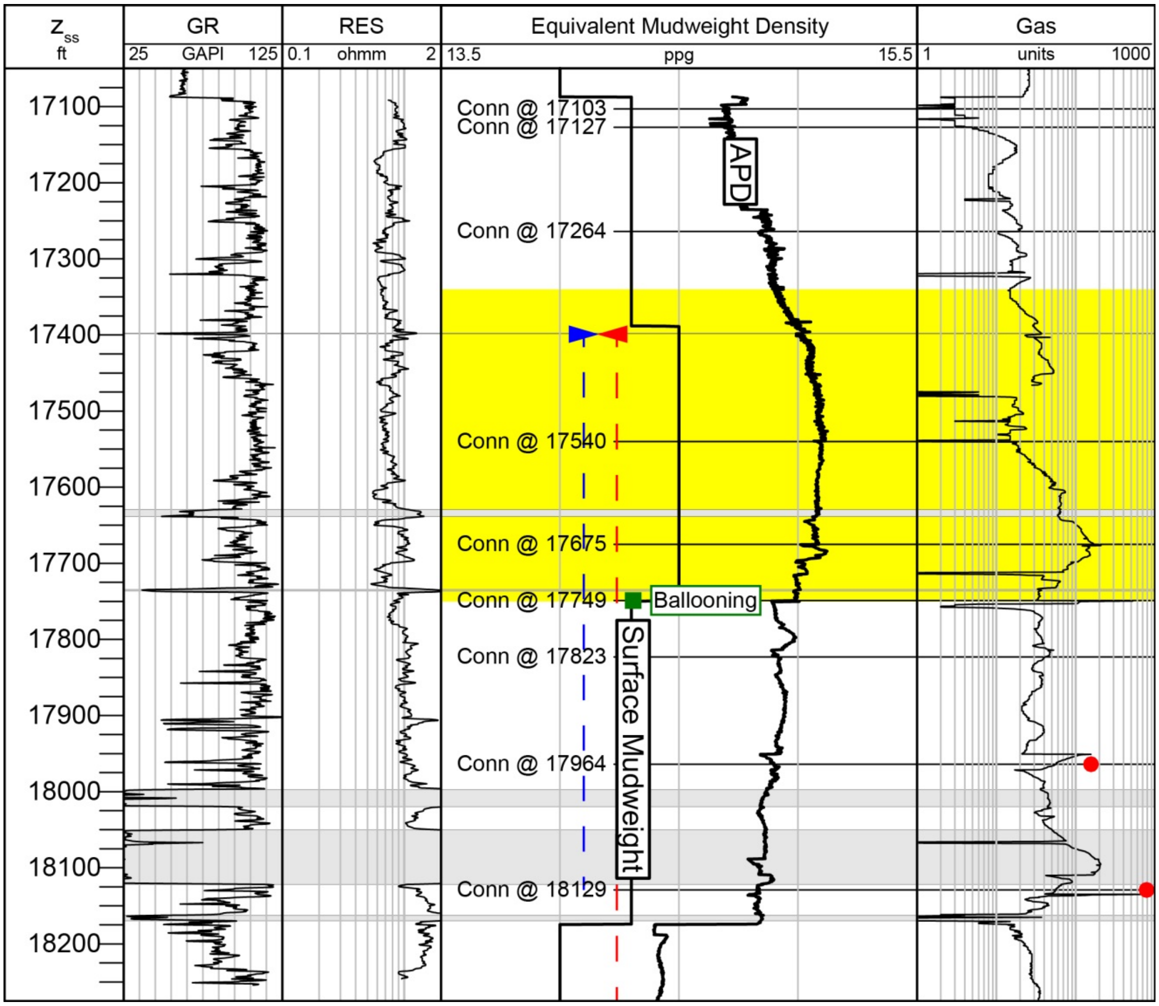

Figure B.9: Equivalent mudweight vs. depth profile of the 17399 ft z_{ss} gas event. The yellow rectangle highlights the background gas response to changes in the ECD. As the ECD (inferred from the APD) decreases, the background gas appears to increase. Red and blue triangles denote the location and upper and lower pore pressure bounds from this event. The red dashed line shows the last recorded ESD projected to the kick depth and the blue dashed line is cut SMW at the 18129 ft connection gas (red dot).

B.3 RESULTS

I analyze pressure at the Macondo well based on in-situ pressure measurements and the occurrence of kicks during drilling (Fig. B.10). Six kicks, 21 direct pressure measurements spanning 17637 to 18110 ft z_{ss} in the Macondo well, and 70 depth corrected MDT measurements from MC 252-1 (Texaco) are used to constrain pore pressure at Macondo. Pore pressure approximately parallels the overburden stress from near the seafloor to 17640 ft z_{ss}. Below, pore pressure decreases by 1200 psi across the M56 reservoir interval.

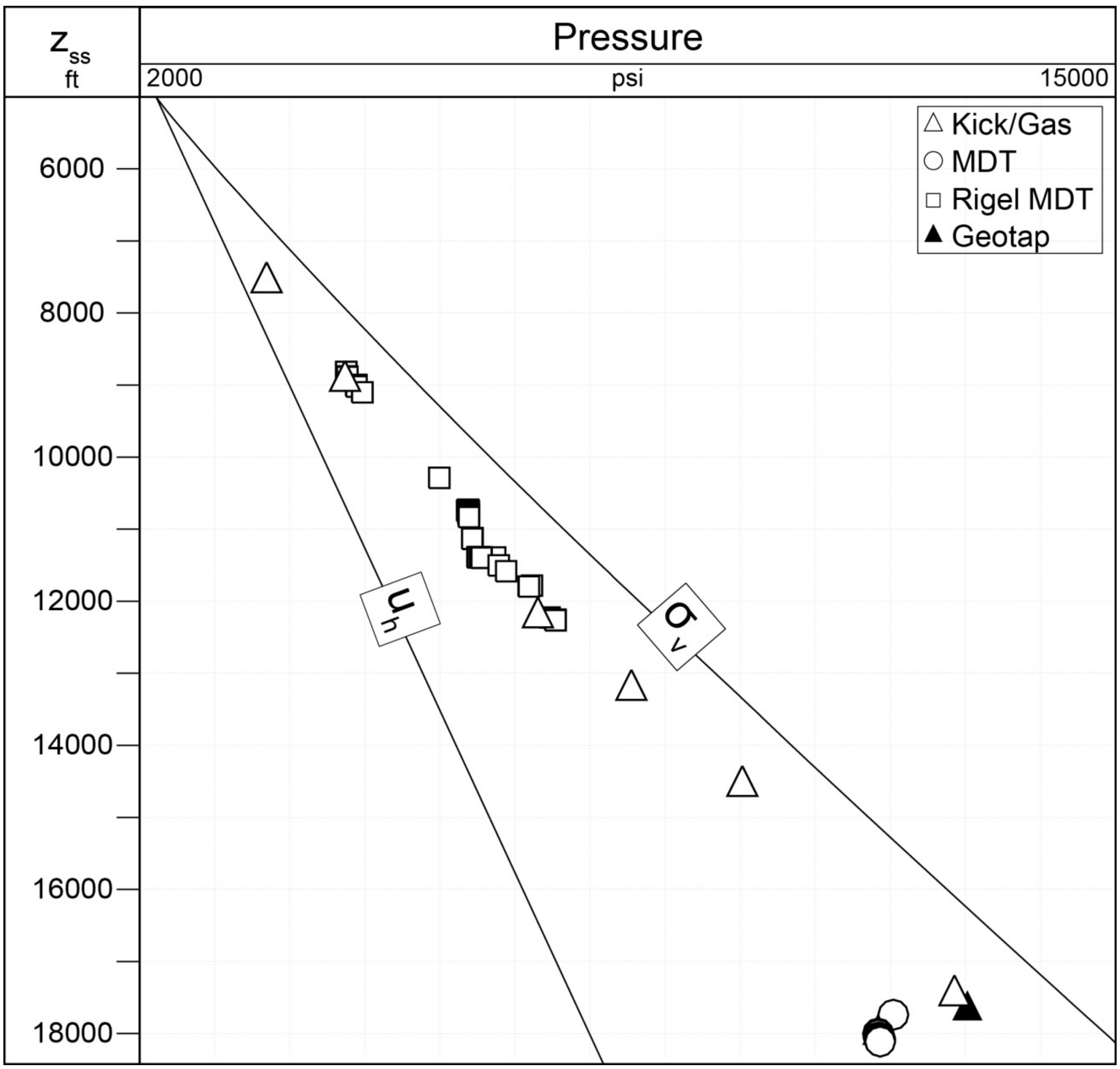

Figure B.10: Pressure vs. depth profile with all pressure indicators. Corrected Texco-252-1 measurements are shown as squares. The upper and lower pore

pressure bounds interpreted from kicks are averaged and displayed as triangles.

Glossary

Table G.1: Nomenclature.Tight tests, dry tests, and lost-seal tests have been excluded.

Symbol	Name	Dimensions	Units
z_{ss}	true vertical depth below the sea surface (mean sea level)	L^1	(feet or meters)
z_{sf}	true vertical depth below the seafloor	L^1	(feet or meters)
$z_{df\ DWH}$	true vertical depth below the drill floor of the Deepwater Horizon (75 ft above mean sea level)	L^1	(feet or meters)
$z_{df\ Marianas}$	true vertical depth below the drill floor of the Marianas (89 ft above mean sea level)	L^1	(feet or meters)
σ_v'	vertical effective stress	$M^1L^{-1}T^{-2}$	(psi or MPa)
σ_v	total vertical stress	$M^1L^{-1}T^{-2}$	(psi or MPa)
u	pore pressure	$M^1L^{-1}T^{-2}$	(psi or MPa)
u*	excess pressure	$M^1L^{-1}T^{-2}$	(psi or MPa)
u_h	hydrostatic pore pressure	$M^1L^{-1}T^{-2}$	(psi or MPa)
ρ_{pw}	pore-water density	M^1L^{-3}	(g/cm^3)
φ	porosity	-	-
φ_0	reference porosity	-	-
φ_m	clay-bound water porosity	-	-
ρ	bulk density	M^1L^{-3}	(g/cm^3)
ρ_{pf}	pore-fluid density	M^1L^{-3}	(g/cm^3)
ρ_{pw}	pore-water density	M^1L^{-3}	(g/cm^3)
ρ_{sw}	sea-water density	M^1L^{-3}	(g/cm^3)
ρ_m	matrix density	M^1L^{-3}	(g/cm^3)
v	log-derived acoustic velocity	$L^{-1}T^1$	(μs/ft or μs/m)
v_{ma}	matrix velocity	$L^{-1}T^1$	(μs/ft or μs/m)
λ	empirical consolidation constant (Athy)	-	-
β	empirical consolidation constant (Lahann)	-	-
λ^*	normalized overpressure	-	-
g	acceleration of gravity	L^1T^{-2}	(ft/s^2 or m/s^2)
FPIT	formation pressure integrity test	$M^1L^{-1}T^{-2}$	(psi or MPa)
FIT	formation integrity test	$M^1L^{-1}T^{-2}$	(psi or MPa)
LOT	leak-off test	$M^1L^{-1}T^{-2}$	(psi or MPa)

XLOT	extended leak-off test	$M^1L^{-1}T^{-2}$	(psi or MPa)
MDT	modular dynamic formation tester	$M^1L^{-1}T^{-2}$	(psi or MPa)
ESD	equivalent static density	$M^1L^{-1}T^{-2}$	(psi or MPa)
ECD	equivalent circulating density	$M^1L^{-1}T^{-2}$	(psi or MPa)
SIDPP	shut-in drill pipe pressure	$M^1L^{-1}T^{-2}$	(psi or MPa)
EMW	equivalent mud weight	M^1L^{-3}	(lb/gal or ppg)
A/B	empirically derived constants for Gardner eqn.		
P_{static}	downhole static pressure	$M^1L^{-1}T^{-2}$	(psi or MPa)
$P_{surface}$	surface pressure	$M^1L^{-1}T^{-2}$	(psi or MPa)
T	temperature		

References

Addis, M., Hanssen, T., Yassir, N., Willoughby, D., and Enever, J., 1998, A comparison of leak-off test and extended leak-off test data for stress estimation, *in* Proceedings SPE/ISRM Rock Mechanics in Petroleum Engineering 1998, Society of Petroleum Engineers.

Alberty, M., and McLean, M., 2001, Fracture gradients in depleted reservoirs-drilling wells in late reservoir life, *in* Proceedings SPE/IADC drilling conference 2001, Society of Petroleum Engineers.

Alberty, M. W., 2010, Email: From: Alberty, Mark W, Sent Thur Sep 23 14:24:41 2010, Subject: RE: MC252 #1 Attachment: Macondo LOT Worksheet.

Alberty, M. W., and Fink, K., 2014, The Use of Connection and Total Gases Quantitatively in the Assessment of Shale Pore Pressure: SPE Drilling & Completion, v. 29, no. 02, p. 208-214.

Alberty, M. W., and McLean, M. R., 2014, The use of modeling to enhance the analysis of formation-pressure integrity tests: SPE Drilling & Completion, v. 29, no. 04, p. 431-437.

Anderson, E. M., 1951, The dynamics of faulting and dyke formation with applications to Britain, Hafner Pub. Co.

Athy, L. F., 1930, Density, porosity, and compaction of sedimentary rocks: AAPG Bulletin, v. 14, no. 1, p. 1-24.

Barbier, C., 2015, United States of America v. BP Exploration & Production, Inc., et al., Volume No. 10-4536; MDL 2179, United States District Court Eastern District of Louisiana.

Bartlit, F., Grimsley, S., and Sambhav, S., 2011, Macondo: The gulf oil disaster : Chief Counsel's Report National Commission on the BP Deepwater Horizon Oil Spill and Offshore Drilling.

Beck, F., 2011, Revised Expert Report of Dr. Frederick "Gene" Beck on Well Design, Control, Drilling and Monitoring.

Bjørlykke, K., 1999, Principal aspects of compaction and fluid flow in mudstones: Geological Society, London, Special Publications, v. 158, no. 1, p. 73-78.

Blum, P., 1997, Physical properties handbook: a guide to the shipboard measurement of physical properties of deep-sea cores: Note 26. doi: 10.2973/odp. tn. 26.1997.

Bodek, R., Paine, K., and Albertin, M., 2009, Email - From: Bodek, Robert Sent: Wed Oct 21 20:48:02 2009 Subject RE: Macondo well flow event.

Boebert, E., and Blossom, J. M., 2016, Deepwater Horizon, Harvard University Press.

Bourgoyne, A. T., 2011, Expert Report in re: Oil Spill by the Oil Rig "Deepwater Horizon" in the Gulf of Mexico, on April 20, 2010: United States District Court Eastern District of Louisiana.

BP, 2009a, 18 1/8" x 22" hole-section review (18" CSG section) Drilling Operations: 10/21/09-10/28/09.

-, 2009b, Daily Geological Report 10/26/2009.

-, 2009c, Daily PPFG Report 10/25/2009.

-, 2009d, Macondo RSDP Pre-drill Review.

-, 2010a, Daily Geological Report 04/03/2010.

-, 2010b, Daily Geological Report 04/05/2010.

-, 2010c, Daily Geological Report 04/10/2010.

-, 2010d, Deepwater Horizon Accident Investigation Report.

-, 2010e, Deepwater Horizon Accident Investigation Report, Appendix K (CSI Investigation Team).

-, 2010f, Deepwater Horizon Accident Investigation Report, Appendix W.

-, 2010g, Post-Well Subsurface Description of Macondo well (MC0252_1BP1) v3: BP.

Bradley, J. S., 1975, Abnormal formation pressure: AAPG Bulletin, v. 59, no. 6, p. 957-973.

Brown, A., 2003, Improved interpretation of wireline pressure data: AAPG bulletin, v. 87, no. 2, p. 295-311.

Colten-Bradley, V. A., 1987, Role of pressure in smectite dehydration--effects on geopressure and smectite-to-illite transformation: AAPG Bulletin, v. 71, no. 11, p. 1414-1427.

Combellas-Bigott, R. I., and Galloway, W. E., 2006, Depositional and structural evolution of the middle Miocene depositional episode, east-central Gulf of Mexico: AAPG bulletin, v. 90, no. 3, p. 335-362.

Daines, S. R., 1982, Prediction of fracture pressures for wildcat wells: Journal of Petroleum Technology, v. 34, no. 04, p. 863-872.

Detournay, E., and Carbonell, R., 1997, Fracture-mechanics analysis of the breakdown process in minifracture or leakoff test: SPE production & facilities, v. 12, no. 03, p. 195-199.

Dugan, B., and Sheahan, T., 2012, Offshore sediment overpressures of passive margins: Mechanisms, measurement, and models: Reviews of Geophysics, v. 50, no. 3.

Dutta, N. C., 1986, Shale compaction, burial diagenesis, and geopressures: a dynamic model, solution and some results: Thermal modeling in sedimentary basins: Editions Technip, p. 149-172.

Engineering, N. A. o., and Council, N. R., 2012, Macondo Well Deepwater Horizon Blowout: Lessons for Improving Offshore Drilling Safety, Washington, DC, The National Academies Press, 196 p.:

Flemings, P., and Lupa, J., 2004, Pressure prediction in the Bullwinkle Basin through petrophysics and flow modeling (Green Canyon 65, Gulf of Mexico): Marine and Petroleum Geology, v. 21, no. 10, p. 1311-1322.

Flemings, P. B., Long, H., Dugan, B., Germaine, J., John, C. M., Behrmann, J. H., and Sawyer, D., 2008, Erratum to "Pore pressure penetrometers document high overpressure near the seafloor where multiple submarine landslides have occurred on the continental slope, offshore Louisiana, Gulf of Mexico" [Earth and Planetary Science Letters 269/3-4 (2008) 309-32]: Earth and Planetary Science Letters, v. 274, no. 1–2, p. 269-283.

Flemings, P. B., Stump, B. B., Finkbeiner, T., and Zoback, M., 2002, Flow focusing in overpressured sandstones: Theory, observations, and applications: American Journal of Science, v. 302, no. 10, p. 827-855.

Forrest, J., Marcucci, E., and Scott, P., 2005, Geothermal gradients and subsurface temperatures in the northern Gulf of Mexico, *in* Proceedings The Gulf Coast Association of Geological Societies New Orleans, 2005, Volume 55, GCAGS Transactions, p. 233-248.

Gao, B., and Flemings, P. B., 2017, Pore pressure within dipping reservoirs in overpressured basins: Marine and Petroleum Geology, v. 80, p. 94-111.

Gardner, G., Gardner, L., and Gregory, A., 1974, Formation velocity and density-the diagnostic basics for stratigraphic traps: Geophysics, v. 39, no. 6, p. 770-780.

Hafle, M., and Mueller, E. T., 2010, Drilling & Completions MOC: Production Casing for Macondo (version 2).

Halliburton, 2010a, BP Exploration & Production, Inc., OCS-G 32306 001 ST00BP00, Mississippi Canyon Block 252, RIG: Transocean Deepwater Horizon.
-, 2010b, BP Exploration & Production, OCS-G 32306 001 ST00BP00 & BP01, Mississippi Canyon Block 252, RIG: Transocean Deepwater Horizon.
Hart, B., Flemings, P., and Deshpande, A., 1995, Porosity and pressure: Role of compaction disequilibrium in the development of geopressures in a Gulf Coast Pleistocene basin: Geology, v. 23, no. 1, p. 45-48.
Hickman, S. H., Hsieh, P. A., Mooney, W. D., Enomoto, C. B., Nelson, P. H., Mayer, L. A., Weber, T. C., Moran, K., Flemings, P. B., and McNutt, M. K., 2012, Scientific basis for safely shutting in the Macondo Well after the April 20, 2010 Deepwater Horizon blowout: Proceedings of the National Academy of Sciences, v. 109, no. 50, p. 20268-20273.
Hoffman, J., and Hower, J., 1979, Clay mineral assemblages as low grade metamorphic geothermometers: application to the thrust faulted disturbed belt of Montana, USA: The Society of Economic Paleontologists and Mineralogists, v. 26, p. 55-79.
Hottman, C., and Johnson, R., 1965, Estimation of formation pressures from log-derived shale properties.
Hsieh, P. A., 2011, Application of MODFLOW for oil reservoir simulation during the Deepwater Horizon crisis: Ground Water, v. 49, no. 3, p. 319-323.
Huang, W.-L., Longo, J. M., and Pevear, D. R., 1993, An experimentally derived kinetic model for smectite-to-illite conversion and its use as a geothermometer: Clays and Clay Minerals, v. 41, p. 162-162.
Hubbert, M. K., and Rubey, W. W., 1959, Role of fluid pressure in mechanics of overthrust faulting I. Mechanics of fluid-filled porous solids and its application to overthrust faulting: Geological Society of America Bulletin, v. 70, no. 2, p. 115-166.
Hubbert, M. K., and Willis, D. G., 1972, Mechanics of hydraulic fracturing.
Huffman, A. R., 2011, Expert Report in re: Oil Spill by the Oil Rig "Deepwater Horizon" in the Gulf of Mexico, on April 20, 2010: United States District Court Eastern District of Louisiana.
Issler, D., 1992, A new approach to shale compaction and stratigraphic restoration, Beaufort-Mackenzie Basin and Mackenzie Corridor, Northern Canada (1): AAPG bulletin, v. 76, no. 8, p. 1170-1189.
Lahann, R., 2002, Impact of smectite diagenesis on compaction modeling and compaction equilibrium: Pressure regimes in sedimentary basins and their prediction: AAPG Memoir, v. 76, p. 61-72.
Lahann, R., Lahann, W., McCarty, D., and Hsieh, J., 2001, Influence of clay diagenesis on shale velocities and fluid-pressure, *in* Proceedings Offshore Technology Conference 2001, Offshore Technology Conference.
Lebleu, J., 2010a, 8.5x9.875" Open Hole Loss Event Summary.
-, 2010b, Macondo 20" Open Hole Mud Loss Event Summary.
-, 2010c, Macondo 22" Open Hole Loss Event Summary.
Long, H., 2007, Interpreting pore pressure in marine mudstones with pore pressure penetrometers, in situ data, and laboratory measurements, Thesis.
Long, H., Flemings, P., Germaine, J., and Saffer, D., 2011, Consolidation and overpressure near the seafloor in the Ursa Basin, Deepwater Gulf of Mexico: Earth and Planetary Science Letters, v. 305, no. 1, p. 11-20.

Matthews, W., and Kelly, J., 1967, How to predict formation pressure and fracture gradient: Oil and Gas Journal, v. 65, no. 8, p. 92-106.

McNutt, M. K., Chu, S., Lubchenco, J., Hunter, T., Dreyfus, G., Murawski, S. A., and Kennedy, D. M., 2012, Applications of science and engineering to quantify and control the Deepwater Horizon oil spill: Proceedings of the National Academy of Sciences, v. 109, no. 50, p. 20222-20228.

Mehrabian, A., Savari, S., Whitfill, D., and Abousleiman, Y., 2017, Geomechanics of Wellbore Strengthening Revisited: A Combined Theoretical and Experimental Approach With Field Case Studies, *in* Proceedings SPE/IADC Drilling Conference and Exhibition 2017, Society of Petroleum Engineers.

Merrell, M. P., Flemings, P. B., and Bowers, G. L., 2014, Subsalt pressure prediction in the Miocene Mad Dog field, Gulf of Mexico: AAPG bulletin, v. 98, no. 2, p. 315-340.

Mondol, N. H., Bjørlykke, K., Jahren, J., and Høeg, K., 2007, Experimental mechanical compaction of clay mineral aggregates—Changes in physical properties of mudstones during burial: Marine and Petroleum Geology, v. 24, no. 5, p. 289-311.

Pilkington, P., 1978, Fracture gradient estimates in Tertiary basins: Petroleum Engineer International, v. 8, no. 5, p. 138-148.

Pollastro, R. M., 1993, Considerations and applications of the illite/smectite geothermometer in hydrocarbon-bearing rocks of Miocene to Mississippian age: Clays and Clay minerals, v. 41, p. 119-133.

Posamentier, H. W., 2003, Depositional elements associated with a basin floor channel-levee system: case study from the Gulf of Mexico: Marine and Petroleum Geology, v. 20, no. 6, p. 677-690.

Postler, D., 1997, Pressure integrity test interpretation, *in* Proceedings SPE/IADC drilling conference 1997, Society of Petroleum Engineers.

Reilly, M. J., and Flemings, P. B., 2010, Deep pore pressures and seafloor venting in the Auger Basin, Gulf of Mexico: Basin Research, v. 22, no. 4, p. 380-397.

Rubey, W. W., and Hubbert, M. K., 1959, Role of fluid pressure in mechanics of overthrust faulting II. Overthrust belt in geosynclinal area of western Wyoming in light of fluid-pressure hypothesis: Geological Society of America Bulletin, v. 70, no. 2, p. 167-206.

Seldon, B., and Flemings, P. B., 2005, Reservoir pressure and seafloor venting: Predicting trap integrity in a Gulf of Mexico deepwater turbidite minibasin: AAPG bulletin, v. 89, no. 2, p. 193-209.

Transocean, 2009, Well Control Handbook.

Turley, J. A., 2014, An Engineering Look at the Cause of the 2010 Macondo Blowout, *in* Proceedings IADC/SPE Drilling Conference and Exhibition 2014, Society of Petroleum Engineers.

Unknown, 2011a, Demonstrative: "Macondo History of Lost Returns".

-, 2011b, Demonstrative: "Macondo Was 'The Well From Hell'".

Walker, C., Belvedere, P., Petersen, J., Warrior, S., Cunningham, A., Clemenceau, G., Huenink, C., and Meltz, R., 2012, Straining at the leash: Understanding the full potential of the deep-water, sub-salt Mad Dog field, from appraisal through early production, *in* Proceedings 32nd Annual Gulf Coast Section SEPM Foundation Bob F. Perkns Research Conference,

New Understanding of the Petroleum Systems of Continental Margins of the World 2012, Volume 32, p. 25-64.
Wilhelm, R., Franceware, L., and Guzman, C., 1998, Seismic pressure-prediction method solves problem common in deepwater Gulf of Mexico: Oil and Gas Journal, v. 96, no. 37, p. 67-75.
Yardley, G., and Swarbrick, R., 2000, Lateral transfer: A source of additional overpressure?: Marine and Petroleum Geology, v. 17, no. 4, p. 523-537.
Zhang, J., 2011, Pore pressure prediction from well logs: Methods, modifications, and new approaches: Earth-Science Reviews, v. 108, no. 1, p. 50-63.
Zhang, J., and Yin, S.-X., 2017, Fracture gradient prediction: an overview and an improved method: Petroleum Science, p. 1-11.
Zoback, M. D., 2007, Reservoir geomechanics: Earth stress and rock mechanics applied to exploration, production and wellbore stability, Cambridge Press.